EXTREME ULTRAVIOLET IMAGING
AND RESIST CHARACTERIZATION
USING SPATIAL FILTERING TECHNIQUES

by

Michael David Shumway

Memorandum No. UCB/ERL M04/49

20 December 2004

EXTREME ULTRAVIOLET IMAGING
AND RESIST CHARACTERIZATION
USING SPATIAL FILTERING TECHNIQUES

by

Michael David Shumway

Memorandum No. UCB/ERL M04/49

20 December 2004

ELECTRONICS RESEARCH LABORATORY

College of Engineering
University of California, Berkeley
94720

Extreme Ultraviolet Imaging and Resist Characterization
using Spatial Filtering Techniques

by

Michael David Shumway

B.Sc. (California Institute of Technology) 1998

A dissertation submitted in partial satisfaction of the
requirements for the degree of

Doctor of Philosophy

in

Engineering - Electrical Engineering and Computer Sciences

in the

GRADUATE DIVISION

of the

UNIVERSITY OF CALIFORNIA, BERKELEY

Committee in charge:

Professor Jeffrey Bokor, Chair
Professor Andrew Neureuther
Professor Eugene E. Haller

Fall 2004

The dissertation of Michael David Shumway is approved:

Chair   12/17/04
                                                       Date

                                              12/20/09
                                                       Date

                                              12/20/04
                                                       Date

University of California, Berkeley

Fall 2004

Abstract

Extreme ultraviolet imaging and resist characterization
using spatial filtering techniques
by

Michael David Shumway

Doctor of Philosophy in Engineering – Department of EECS

University of California at Berkeley

Professor Jeffrey Bokor, Chair

This thesis provides information on extreme ultraviolet (EUV) photoresists and

provides new methods to probe resist properties. Resolution and line-edge roughness are

both investigated for linewidths at and below 50 nm. By using a spatial frequency

doubling method, an EUV optic designed for 100-nm resolution was converted into a tool

that prints dense features in the 30- to 50-nm range with low line edge roughness. Loose

pitch features are shown down to 25 nm.

The primary imaging system used in these experiments incorporated coherent 13.4-

nm wavelength light and a 10×-Schwarzschild demagnification optic. High-resolution

and high contrast test patterns were exposed into both chemically amplified and non-

chemically amplified resists. Combining the 10× demagnification provided by the optic

with the spatial-frequency doubling technique, a 20× reduction of the object grating pitch

was obtained. For example, 0.8-μm dense lines on the object grating printed 40-nm dense

lines onto the resist-coated wafer. The line and space patterns were limited to one

1

orientation and a dense 1:1 spacing. The ability to spatial frequency double four pitches in a single exposure was also analyzed and demonstrated. When comparing multiple linewidths, this method removed wafer-processing variations from the printing experiments.
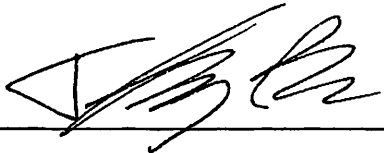
This thesis also describes work done to create specifications for a new 10× optic designed for use with these experiments. Mirror roughness simulations, mirror alignment calculations, and EUV interferometry were all done for this optic. The best full-field images were printed using this new optic.

Furthermore, this thesis presents additional spatial filtering techniques that introduce more ways to look at photoresist performance. Most notably is the method to modulate aerial image contrast. Instead of using a two-exposure process (pattern and background flood), this work integrates the contrast variation into the mask design. By changing the duty cycle of a grating, the field strengths of the diffracted orders are altered. Using spatial filtering, only the 0 and +1 orders are then used to create the field mismatch. This imbalance in the orders creates a decrease in image contrast at the wafer plane. The additional benefit of using this filtering technique is that the duty cycles on the mask do not print on the wafer. Constant linewidths are produced because all orders except for the 0 and +1 are filtered out. The resist ends up seeing only variations in contrast and not the encoded duty cycle information.

Coherence plays an essential role in these experiments. Both the spatial frequency doubling and the aerial image contrast methods utilize the coherent addition of the diffracted orders. Along with this necessary function, coherence also brings ringing

2

effects from hard edges and amplification of defects to the imaging system. Coherence errors are investigated in both experiments and simulations.

To evaluate resist materials for EUV lithography, it is necessary to expose different test patterns with very high spatial resolution (less than 50 nm lines and spaces). To this end, all of the configurations presented here are designed to help evaluate the ultimate performance and extendibility of resist materials for future lithography techniques.

Prof. Jeffrey Bokor

For My Parents and Jen

Table of contents

List of figures

Chapter 1

Chapter 2

Chapter 3

Chapter 4

Chapter 5

Chapter 6

Acknowledgements

Prof. Jeff Bokor, Prof. Andy Neureuther, Prof. Eugene Haller, Prof. Bill Oldham, Prof. David Attwood

Ken Goldberg, Patrick Naulleau, Eric Snow, Sang Hun Lee, Chang Hyun Cho

Paul Denham, Drew Kemp, Seno Rekawa, Phil Batson, Farhad Salmassi, Erik Anderson, Alexander Liddle, Donna O'Connell, Craig Henderson, Heidi Cao, Manish Chandhok, Robert Brainard, John. Bjorkholm, Scott Hector, Mark Terry, Michael Lercel, Sang-In Han, Guojing Zhang,

Yashesh Shroff, Ranjana Sahai, Carolyn White, Kostas Adam, Mike Williamson, Kris Rosfjord, Chang Chang, Weilun Chao, Yan Wang, Lei Yuan, Yijian Chen, Jason Cain, Greg McIntyre, Scott Hafeman, Garth Robins, Frank Gennari, Yunfei Deng, Mike Lam, Daniel Ceperley, Patrick Xuan, Shiying Xiong

Ruth Gjerde, Kia Cooper, Vivian Kim, Charlotte Jones, Beverly Harris, Terry Powell

Chris, Donna, Bret, Jeff, John & Korana, Albert, Michele, Martin, Mansoor, Rahul, Erin, Rene, Tim, Colin, Jeff, Andres, James, Hayley

Sam, Steve & Peggy, Karen, Phyllis, Greg & Keri, Trey, Brian, Dana, Erin, Tim, Mike & Michaelle, Jess & Kristina, John & Maria, Adam, Joanne, Ryan, Seth, Jim

Brett, Aaron, Mark, Mike, Fred

ShumMom, ShumDad, Jen, Scott, Karen, Alex, Carl, Rose, Lori, Dave, Rosa, Bob, Maurissa, Bob, Erik, Brandy, Charlie, Anna, Leonard, Margery, Lucille, Kathy, Joanie, Scott

----

1 Introduction

1.1 Background

The lithography community is continually striving to print smaller and smaller features into photoresists. Challenges have come and gone on the iconic *International Technology Roadmap for Semiconductors* (ITRS) [1]. Numerous "next-generation" lithography (NGL) methods have been proposed. Some have been tossed aside while others have become champions and have led the industry through several feature generations. This community has continually pushed toward smaller critical dimensions (CD) and pioneered technologies that would not only work but would turn profits for the computer chip manufacturers.

Extreme ultraviolet (EUV) lithography won the battle over several competing technologies to become the most feasible NGL technique. Even with that being the case, EUV lithography has still been pushed farther down the roadmap due to extra efforts needed with 193 nm technology. The even shorter wavelength, 157-nm lithography, has faded away partially due to the upstart called immersion lithography (IL) [25]. The immersion technique also seems to be pushing EUV lithography farther down the technology path. Will EUV lithography make it to commercialization? Even if EUV lithography has all of its showstoppers removed, might some other technology overtake it? Perhaps maskless, imprint, or some form of self-assembly will take lithography tools and technologies in newer and more profitable directions.

EUV lithography has made many exciting advances for more than a decade now, but there are still hurdles that must be overcome. In this chapter, an overview of EUV lithography is presented to spotlight the successes of EUV and to identify areas that must still be researched.

1.2 Extreme Ultraviolet Lithography

Extreme ultraviolet lithography is a next-generation lithography technique for manufacturing integrated circuits at high volumes [2]. It is targeted to print critical dimensions of 45 nm and smaller with a large depth of focus (DOF) [3]. EUV lithography continues on the path of projection optical systems but with a radical reduction in wavelength (10-15 nm) and a conversion to lower numerical apertures (NA).

This reduction in wavelength is important due to the boost in resolution performance. Ultimate lithographic resolution, R, is calculated by the equation

$$R = k_1 \cdot (\frac{\lambda}{NA}),$$
(Eq. 1-1)

where NA is the numerical aperture of the tool, λ is the wavelength of light used, and k_1 is an empirical constant based on the rest of the lithography system. For EUV systems, the range of k_1 is between 0.5 and 1.0 [4]. This shorter wavelength allows for an impressive reduction in printable feature size while keeping modest values of k_1 and NA.

Since 1996, EUV interferometry has been conducted at Lawrence Berkeley National Laboratory. This started with 2-mirror optical systems (10x, 0.08NA) which will be discussed in Chapter 3. From 1999 to 2002, two 4-mirror systems (4x, 0.1NA) were

developed and used for EUV research. Most recently another 2-mirror optic (Micro Exposure Tool) has been built (5×, 0.3NA) and will also be discussed in Chapter 3.

Current state-of-the-art features use 193 nm lithography. Adding immersion technology to these tools seems to have usurped 157 nm lithography as the next step. But there will come a point at which conventional systems will no longer produce the finer dimensions needed for new chip designs and an alternative method must be used. This point will be reached somewhere under 65-nm feature sizes. As mentioned in the Background Section (1.1), there were originally many NGL possibilities to solve this problem. That list included proximity x-ray lithography (PXL), proximity electron lithography (PEL), ion projection lithography (IPL), and electron projection lithography (EPL). The next generation lithography technique used will be implemented only when it is necessary since current optical lithography methods are already well understood and well established.

Today, the Next Generation Lithography roadmap only emphasizes the extreme ultraviolet and EPL techniques [5]. Currently, the NGL community has placed more confidence in the EUV lithography process. The projection e-beam technique (known as SCALPEL) creates very fine features using a scattering membrane mask. The mask design for this technique is a challenge since it requires struts for stability and stress control to help decrease distortions [3].

There are no materials known that allow for lenses to be used at EUV wavelengths so the mask and projection systems use only mirrors. Also, most materials absorb EUV wavelengths, including nitrogen and oxygen, and so this system must always be used in a

3

vacuum. The mirrors, masks, and resists are currently in R&D stages and are a few of the primary issues of concern for EUV lithography. All three of these will be addressed in the next sections. It is important to add that an acceptable EUV source is also a major hurdle for the commercialization of EUV lithography. Source power is now on the order of 10 Watts but it needs to grow to 100-120 Watts for commercialization. My experiments utilized the Advanced Light Source, an electron synchrotron at the Lawrence Berkeley National Laboratory, which provided a consistent low-power source (1-2 Watts) for this research.

1.2.1 Thin Film Multilayers

The creation of reflective mirror surfaces at EUV wavelengths was in many respects the enabling technology for EUV lithography. Due to advances in thin film growth and processing, these mirrors have opened the doors for exciting research at EUV and soft X-ray wavelengths. Several techniques have been used to create these reflective multilayers including evaporation, sputtering, laser-plasma deposition, and epitaxial growth. This section will explain how reflective multilayers work and the methods used to fabricate them.

Thin film multilayer mirrors are a collection of alternating indexed polycrystalline layers [5]. These mirrors can be thought of as Bragg reflectors made by using both high Z and low Z materials. The high Z material causes scattering and absorption at EUV wavelengths. This material is chosen to have as little absorption as possible to keep the overall reflectivity high but provide large scattering due to a significant refractive index difference between the high and low Z layers. The function of the low Z material is primarily to space the scattering planes so that reflections are constructive over roundtrips

through the layer pairs. At normal incidence, the thickness of one layer pair is equal to half the wavelength. There are two EUV wavelength ranges that currently have mirror designs that provide enough reflectivity for lithography purposes. For the λ=11.3-11.6 nm range, alternating molybdenum and beryllium layers are used. In the λ=13.3-13.6 nm range, molybdenum and silicon are alternated. The Mo/Be mirrors typically have 70 layers and the Mo/Si mirrors are constructed using 40 layers. Molybdenum has the second greatest phase shift next to beryllium at EUV wavelengths.

The multilayer mirrors reflect around 70% of the incoming photons within a relatively small bandwidth (4-5%) [7]. Figure 1-1 shows typical reflectivity plots. Recently, a Ru-capped multilayer has shown a reflectivity of 69.6% for 13.4-nm photons [24]. This multilayer also has better oxidation resistance than the original Si/SiO_2 capping layer.
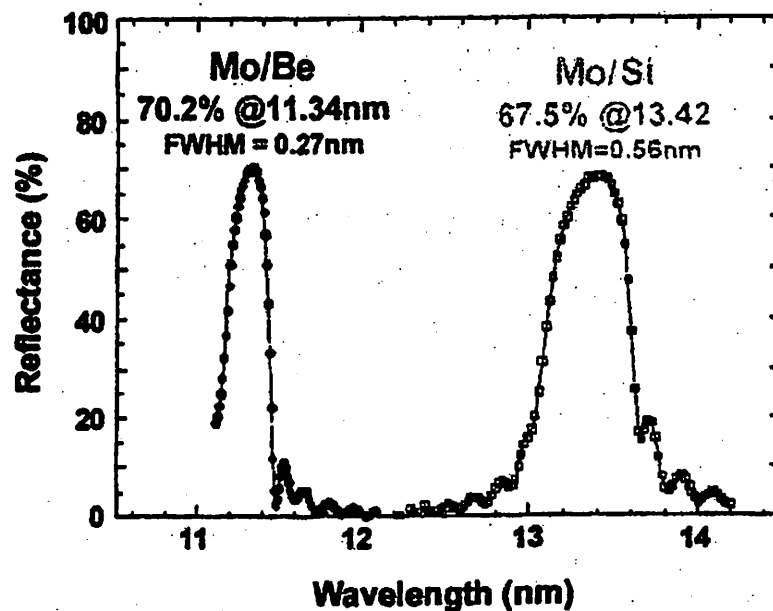
Figure 1-1: Standard reflectivity plots for the two different EUV multilayers. [8]

Not only is absorption occurring in the layer pairs but interdiffusion also plays an important role in reflectivity. The more the reflective planes are blurred by interdiffusion, the lower the reflectivity. Temperature plays a key role here. This can be seen in Figure 1-2. As temperature is increased, stress is relieved but reflectance drops considerably due to this interdiffusion.
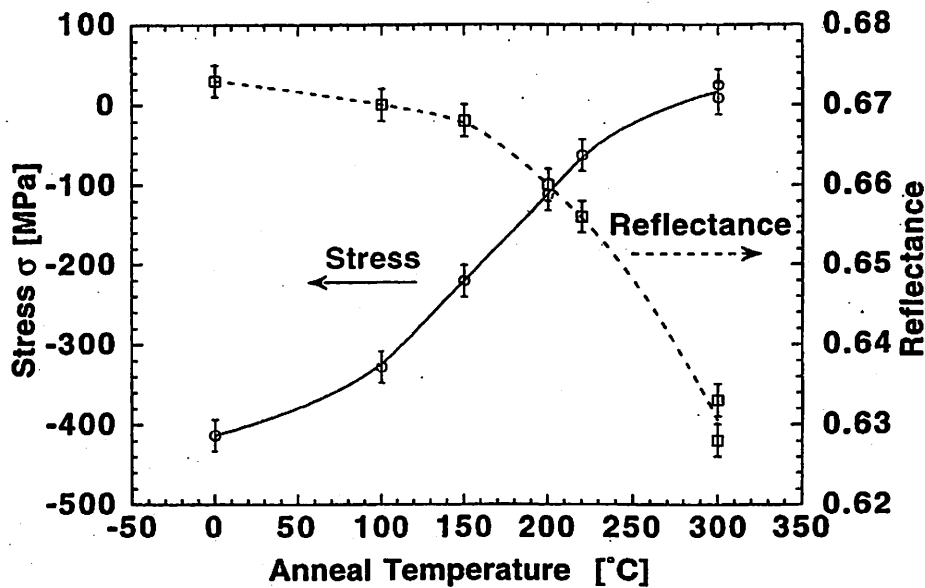
Figure 1-2: Stress and reflectance as a function of anneal temperature. As temperature is increased the stress is reduced in the multilayer stack but reflectance is lost due to interdiffusion. [8]

There is currently a temperature limit of 150°C for any multilayer processing step in order to insure the reflectance stays at acceptable levels. This creates a challenge for process engineers, who need to do further deposition and etch steps on top of these multilayers to create EUV masks. Full EUV lithography systems will contain around 10 mirrors and if each is reflecting at 70%, only 2 to 3% of the original flux will hit the wafer, which can result in lengthy (costly) exposure times.

6

1.2.2 Masks and Defects

This section describes the mask technologies associated with extreme ultraviolet lithography. It piggybacks on the multilayer research discussed above since a great reflector surface is the first requirement to fabricating an EUV mask.

An EUV mask consists of a multilayer reflection coating below a patterned absorber layer. There are three areas for possible mask defects. They can arise in the absorber pattern, as particle contamination on the finished mask, or in the reflecting multilayer.

The absorber defects can be fixed using selective etching or selective deposition depending on the type of defect. Particle contamination on the finished mask is still an issue for research. There are currently no pellicles available to fully transmit the valuable EUV photons. Mask handlers must develop technologies that do not require pellicles. In addition, there is a problem in fixing the multilayer defects since they are difficult to detect and then to repair.

Mask absorber materials are also being researched [12]. Almost all of the emphasis is with the 13.4nm Mo/Si multilayer stack. Some current contenders are Cr, TiN, NiSi, TaSi(N), Ta, TaN, and TaGe. When evaluating these absorbers there are many requirements. These include EUV absorbance, inspection ability, and repair. For example, a common parameter is the contrast seen when exposing the mask with deep ultraviolet (DUV) photons. More contrast between the absorber and multilayer increases the inspection ability.

There are currently two absorber process flows that have been developed: subtractive and damascene. The subtractive technique is easier to fabricate but damascene allows for better mask cleaning and inspection. One of the disadvantages of the damascene process

is that the additional silicon used partially absorbs EUV photons (~20% for 70nm of Si). In general, absorber thickness can be less than 100nm for either technique.

Manufacturing issues for EUV masks include substrate roughness, number of defects, and reproducibility of layer thicknesses. A small defect on the substrate can become increasingly problematic as tens of layers are deposited above it. Not only can they be hard to detect, but techniques to fix them are still not mature. A low defect deposition process is needed for the multilayers followed by a suitable inspection technique.

Such a solution for low defect deposition has been found by a collaboration between Lawrence Livermore National Laboratory and Veeco Instruments. The previous method used to make reflective multilayers for EUV lithography was magnetron sputtering. This method produced approximately 10,000 defects per cm^2, which would not be practical for commercial EUV lithography. The new method that has been developed is called the Ultra Clean Ion Beam Sputter Deposition System [9]. It can produce masks with up to 81 alternating layers of silicon and molybdenum, each with a thickness of 3 to 4 nm. First, ions hit Si, Mo, or Be targets, which cause a vapor to be formed. The vapor is then deposited on the surface with Ångstrom accuracy. This technique produces a defect density under 0.1 defects per cm^2. This is an impressive and necessary improvement that has helped EUV lithography in becoming feasible for industrial applications. It is important to note that these mirrors are usually not flat which means deposition techniques must vary layer thickness across a curved surface. Figure 1-3 illustrates the newer deposition system. By varying the table and mirror rotation speeds

the thicknesses of the layers can be changed for each layer and for different areas on the mirror surface.
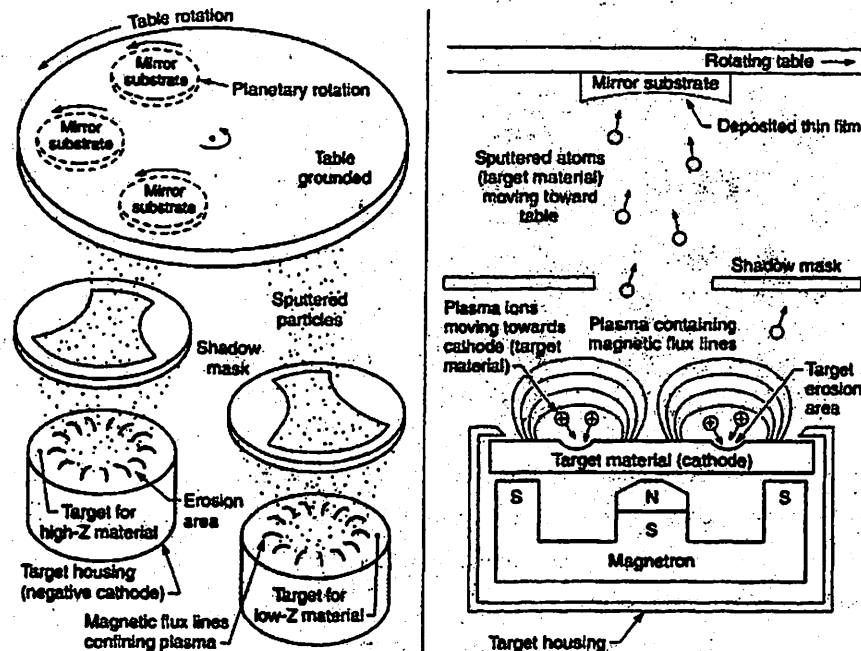
Figure 1-3: Magnetron sputtering setup. The shadow masks allow for controlled deposition (uniformity) and the table/mirror rotations allow for varying layer thicknesses. [6]

As mentioned above, inspection techniques are also very important. Many current optical inspection methods can be used, e.g., laser-based particle detection, optical microscopy, and scanning electron microscopy. Unfortunately, these methods can only be used for investigating surface or near-surface defects and cannot find defects buried in the multilayer reflector. This means that inspection tools need to be developed that use extreme ultraviolet light in order to characterize the mirrors completely, including deep into the multilayers.

Researchers have being looking into various inspection systems. The techniques are based on scanning a focused EUV beam across the wafer and measuring the intensity of the reflected beam. In one case, the beam was focused down to a diameter of a few microns [10]. As the beam was scanned, both light and dark field photodetectors were able to record changes in the scattered beam caused by the defects. The shape and size of the defects, as well as the incident beam size, all cause changes in the intensity. Since this inspection technique uses EUV photons it accurately characterizes the properties of these defects. When inspection is performed at non-EUV wavelengths the characterization is only approximate.

The results were promising in terms of measuring defects, but for industrial practicality problems still arose. Most importantly, the inspection scanning rate of the masks needed to be increased. Two methods were suggested do this. First, an increase in the photon flux from the EUV source would increase the signal to noise ratio and therefore allow for faster scans. Second, by making the incident beam size smaller, less time is necessary for each scan region. This has led to the development of another tool. It is called an aerial image microscope (AIM) [11]. One is currently being built at the Advanced Light Source incorporating one of the 10× Schwarzschild optics used in this research. This AIM tool will use at-wavelength inspection techniques to investigate EUV mirror substrates and mask defects.

Masks are definitely the key to most of the next generation lithographies. A possible revolution to current lithography practices is maskless lithography. There is a procedure being researched using EUV light and an adjustable array of nanomirrors that would eliminate the need for a mask [13]. Mirrors could be tilted by applying a voltage between

10

the mirror and the base. Any "off" mirrors would simply direct the EUV light away from the wafer. This would remove three major EUV mask hurdles which are their high cost, inherent defects, and lack of a suitable pellicle [14].

1.2.3 Photoresists

Challenges have also arisen in the realm of EUV photoresist materials and development processes. The highly absorbing nature of EUV waves by most materials and the desire to print small feature sizes require the use of thin layer imaging resists. There are many areas of interest which include line-edge roughness (LER), EUV sensitivity, etch resistance, resolution, depth of focus, outgassing, photoresist collapse, and compatibility with existing manufacturing processes [15,16].

Understanding the causes and then learning to minimize LER is an important step for photoresist success. The industry is reaching a point where LER is a significant percent of the feature width. For example, dense 30-nm lines have shown 5-nm LER (3 sigma rms). LER values of this magnitude will become unacceptable in future generations. In fact, increased LER in transistors has been shown to degrade performance [15].

The causes of LER are still being investigated, but there are several suggested contributors. When exposing a resist, a 25%-50% change in dose is required to change the soluble resist film to insoluble (for positive tone resists) [17]. The dissolution behavior in this portion of the exposure region is what determines the sharpness of the resist line which in turn contributes to the LER. High intensity modulation (high contrast images) will minimize the inhomogeneous dissolution behavior's spatial extent. See Figure 1-4 for a diagram of this effect.

11
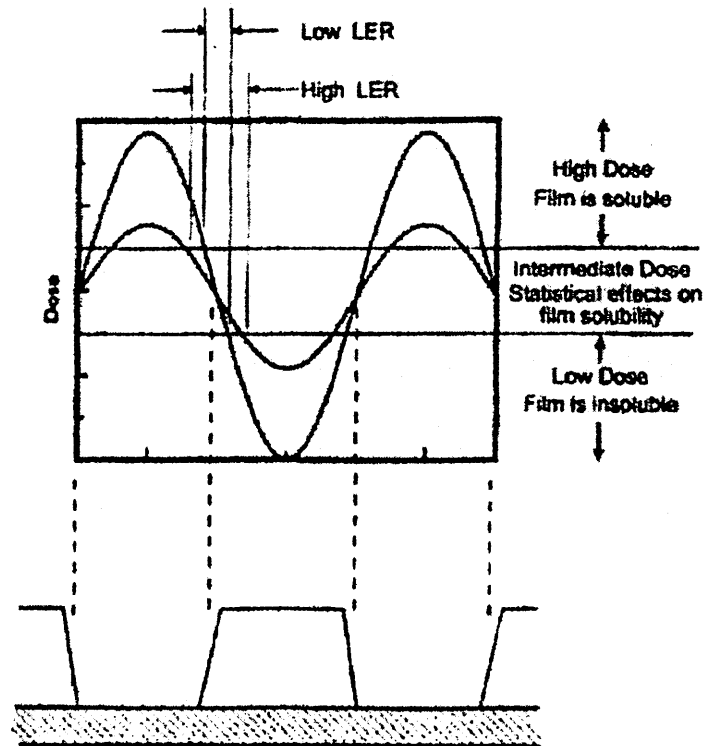
Figure 1-4: Effect of aerial image contrast on line edge roughness [17]

The inhomogeneous solution could be caused by non-uniform diffusion of the photo-acid generator (PAG), nano-scale variations in acid deprotection, or general statistical effects on the solubility of the polymer chains. High dissolution imbalance is also important to get a steep solubility gradient at the line edge during baking in order to get smoother lines. The following is a list of other proposed causes of LER:

Resist resin size/shape/composition
Developer strength
Stress/tensions during development [18]
Optical density of the photoresist [19]
Phase compatibility between protected and deprotected polymers [20]
Shot noise [21]

12

Imaging depth in EUV photoresists will be around 100 nm. If this is too thin to do full wafer processing then there are some thin layer imaging (TLI) processes being investigated [22,23]. Figure 1-5 shows two examples of TLI.
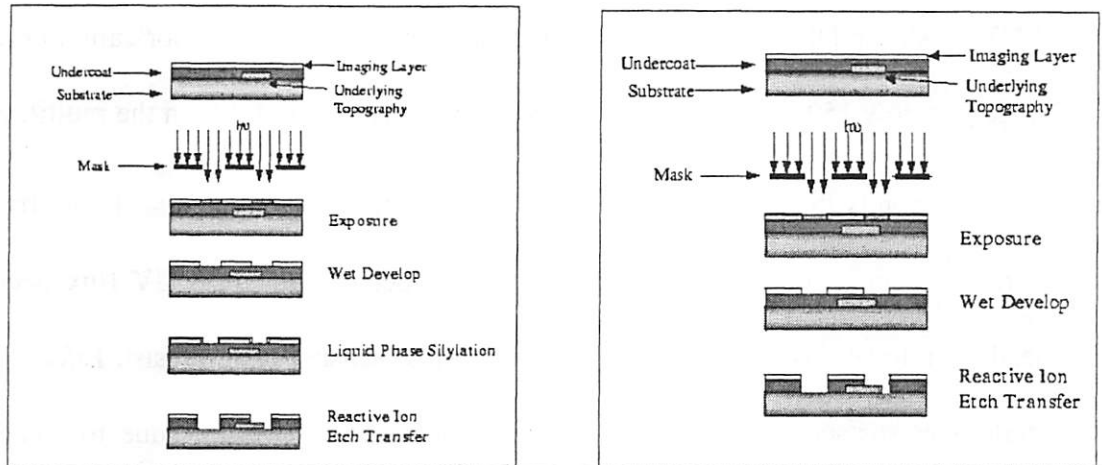
Figure 1-5: Two examples of thin-layer imaging: Silylated top-surface imaging (left) and bi-layer resist (right) [22]

Silyated top-surface imaging (TSI) includes a cross-linked bottom layer which is etched after the top layer is mixed with silicon vapor to become a hardmask. The bi-layer system on the right makes the top layer become a SiO_2 etch mask. A third technique, an ultra-thin resist (UTR) method is similar to the bi-layer process except that the bottom layer starts out as an etch-resistant hardmask. Silyated TSI seems to contribute large amounts of LER and is generally not considered a practical technique. Stable materials for the bi-layer process are still being investigated. Currently, the highest potential lies in the UTR technique.

1.2.4 Summary

There have been many advances in EUV technologies. However, there are still many challenges and risks that need to be evaluated. Both the substrate and multilayer need to be essentially defect free and smooth. Inspection tools need to be developed for EUV masks and they need to work in industry settings. Also, the fabrication process must be kept below 150°C or there will be too much thermal instability in the multilayer.

Currently the multilayer surfaces have reflectivities around 70%. Every fraction of a percentage point counts because that means a decrease in the EUV flux needed. This leads to a lower laser power requirement or a less sensitive photoresist. Lifetime of these multilayer surfaces is also very important. Degradation overtime due to contamination and EUV radiation needs to be minimized.

1.3 Research Motivations

The purpose of this research was to contribute to the EUV program in areas that were critical to the development of EUV as a commercially-viable technology. By utilizing existing equipment at the Lawrence Berkeley National Laboratory and the interferometry beamline at the Advanced Light Source it was decided to make advances in designing imaging systems and tools to aid in photoresist experiments. Using EUV wavelengths to print small features is necessary for the timely development of resists and processing techniques for the entire EUV lithography program. At the time I began my research, there were only a few systems in the world that could print images using EUV photons. At the conclusion of this research it is satisfying to see that the Micro Exposure Tool (MET) has come on-line and is able to print comparably-sized features. In addition,

the MET has variable coherence, larger field size, and a larger NA. All of which will enable it to push toward even smaller and more complex features.

1.4 Thesis Content

Chapter 2 details the workhorse technique of this research – the spatial frequency doubling method. Chapter 3 provides an overview of the EUV optical systems used at the ALS. This includes information on mirror surface roughness, interferometry methods, and simulations.

Chapter 4 explains the methodology and apparatus used in the experiments as well as the many upgrades installed during the course of the research. Chapter 5 details exposure results achieved in the different photoresists and experimental configurations. Chapter 6 provides a description of the aerial image contrast method and its LER findings. Finally, Chapter 7 summarizes this research and addresses future research potential.

1.5 References

[1]   http://public.itrs.net "International Technology Roadmap for Semiconductors"

[2]   S. Rizvi, "National technology roadmap for semiconductors: an analysis and perspective," Proc. SPIE, Vol. 3331, 190-196 (1998).

[3]   D. Lammers, "EUV, SCALPEL systems get Sematech's support," EE Times, http://www.eetimes.com/story/industry_semiconductor_news/OEG19981218S002
3

[4]   J. Bokor, A. Neureuther, and W. Oldham, "Advanced Lithography for ULSI",

        IEEE Circuits and Devices Magazine, Vol. 12, No. 1, 11-15 (Jan 1996).

[5]   http://public.itrs.net/Files/2003ITRS/Litho2003.pdf

[6]   D. Attwood, Soft x-rays and extreme ultraviolet radiation, Cambridge University

        Press, United Kingdom, (1999).

[7]   W. Silfvast, "Intense EUV incoherent plasma sources for EUV lithography and

        other applications," IEEE Journal of Quantum Electronics, Vol. 35, No. 5, 90-94

        (May 1999).

[8]   Don Sweeny and David Attwood, NGL Review presentation, 1998.

[9]   A. Heller, "Compact, more powerful chips from virtually defect-free thin-film

        system," http://www.llnl.gov/str/Vernon.html.

[10]   S. Jeong, M. Idir, L. Johnson, Y. Lin, P. Baston, R. Levesque, P. Kearney, P. Yan,

        E. Gullikson, J. Underwood, and J. Bokor, "Actinic detection of EUVL mask

        blank defects," Proc. SPIE, Vol. 3546, 524-530 (1998).

[11]   A. Barty, J. Taylor, R. Hudyma, E. Spiller, D. Sweeney, G. Shelden, and J.

        Urbach, "Aerial image microscope for the inspection of defects in EUV masks,"

        Proc. SPIE, Vol. 4889, 1073-1084 (2002).

[12]   P. Yan, G. Zhang, P. Kofron, J. Chow, A. Stivers, E. Tejnil, G. Cardinale, and P.

        Kearney, "EUV mask patterning approaches," Proc. SPIE, Vol. 3676, 309-313

        (1999).

[13]   Y. Shroff, Y. Chen, W. Oldham, "Image optimization for maskless lithography,"
        Proc. SPIE, Vol. 5374, 637 (2004).

[14]   Hawryluk, Sheldon, and Troccolo, "EUVL Reticle Factory Model and Reticle
        Cost Analysis", Conference of OSA Trends in Optics and Photonics, Vol. 4, 54
        (1996).

[15]   M. Ryoo, S. Shirayone, H. Oizumi, and N. Matsuzawa, "Control of line edge
        roughness of ultrathin resist films subjected to EUV exposure," Proc. SPIE, Vol.
        4345, 903-911 (2001).

[16]   Discussion with Heidi Cao, Intel Corporation

[17]   W. Hinsberg, F. Houle, J. Hoffnagle, M. Sanchez, G. Wallraff, M. Morrison, and
        S. Frank, "Deep-ultraviolet interferometric lithography as a tool for assessment of
        chemically amplified photoresist performance," J. Vac. Sci. Technol. B, Vol.16,
        No. 6, 3689-3694 (1998).

[18]   Discussion with Andy Neureuther, Professor at UC Berkeley (11/19/2004)

[19]   M. Williamson, X. Meng, and A. Neureuther, "Effects of image contrast and resist
        types upon line edge roughness (LER)," Proc. SPIE, Vol. 4690, 357 (2002)
        (accepted for publication).

[20]   Q. Lin, D. Goldfarb, M. Angelopoulos, S. Sriram, and J. Moore, "Line-edge
        roughness in positive-tone chemically amplified resists: effect of additives and
        processing conditions," Proc SPIE, Vol. 4345, 78 (2001).

[21]   V. Rao, J. Hutchinson, S. Holl, J. Langston, C. Henderson, D. Wheeler, G. Cardinale, D O'Connell, J. Bohland, G. Taylor, and R. Sinta, "Top surface imaging process and materials development for 193 nm and extreme ultraviolet lithography," J. Vac. Sci. Technol. B, Vol. 16, No. 6, 3722 (1998).

[22]   C. Henderson, D. Wheeler, T. Pollagi, D. O'Connell, J. Goldsmith, A. Fisher, G. Cardinale, J. Hutchinson, and V. Rao, "Top Surface Imaging Resists for EUV Lithography," Proc SPIE, Vol. 3331, 32-39 (1998).

[23]   V. Rao, J. Cobb, C. Henderson, U. Okoranyanwu, D. Bozman, P. Mangat, R Brainard, and J. Mackevich, Proc SPIE, Vol. 3676, 615 (1999).

[24]   S. Bajt, EUV VNL Quarterly Status Meeting, September 8, 2004.

[25]   W. Hinsberg, G. Wallraff, C. Larson, B. Davis, V. Deline, S. Raoux, D. Miller, F. Houle, J. Hoffnagle, M. Sanchez, C. Rettner, L. Sundberg, D. Medeiros, R. Dammel, and W. Conley, "Liquid immersion lithography – evaluation of resist issues," Proc. SPIE, Vol. 5376, 21-33 (2004).

2   Spatial Frequency Doubling

2.1   Introduction

The resolution limits for most EUV resists were unknown at the beginning of this research. This was primarily because existing tools could not reach the necessary feature sizes to determine resist potential. To address this shortcoming, I worked to modify an interferometry station into an imaging tool. This helped give feedback for the timely development of resists and processing techniques for the EUV lithography program. The spatial frequency doubling technique I incorporated was based on work done previously that produced 250 nm lines and spaces using 248 nm wavelength light [1,2]. A second method of spatial frequency multiplying, using multiple gratings to diffract orders, has also been demonstrated [7,8]. This technique used coherent 1.8-nm radiation to pattern 50-nm period gratings and incoherent 13-nm radiation to pattern dense lines with a 250-nm period.

High contrast images are achievable by using spatial frequency filtering techniques. Several other aperture-plane filtering techniques will be discussed later which also extended the resist-analysis options (multiple pitch printing in Chapter 5 and aerial image contrast variation in Chapter 6).

By using spatially coherent 13.4-nm wavelength light and a 10×-demagnification optical system, high-resolution/high-contrast test patterns were exposed that extended well beyond the conventional resolution limits of the designed optic. By combining the

10x demagnification provided by the optic with the spatial-frequency doubling technique, 20x reduction of the object grating pitch was obtained. For example, 0.8-micron dense lines on the object grating printed 40-nm dense lines onto the resist-coated wafer. To get these small features, the line and space patterns are restricted to a single orientation and a dense 1:1 spacing.

2.2 Theory

The spatial frequency doubling technique is most easily envisioned for a system configured to image a simple grating object. Conventional imaging will collect all the lowest diffracted orders from the mask that fit within the NA of the imaging system. This is shown in Figure 2-1.
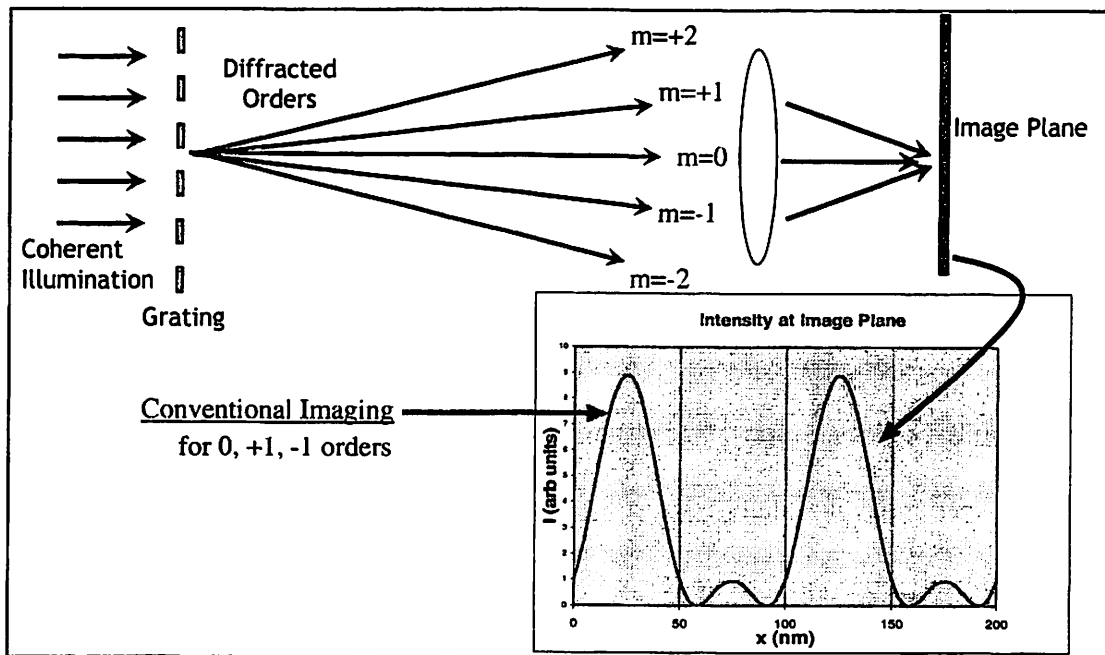
Figure 2-1: Diagram of conventional imaging system collection the lowest three orders (0, +1, and -1).

20

For coherent imaging, the field, E, at the image plane from the lowest three orders (0, +1, -1) is proportional to [3]

$$E(\omega) \propto 1 + \sin(\omega + \Theta) + \sin(\omega - \Theta),$$ (Eq. 2-1)

Where

$$\omega = \frac{2\pi x}{p}$$ (Eq. 2-2)

and

$$\Theta = \sin^{-1}(\frac{\lambda}{p}).$$ (Eq. 2-3)

In these equations, x is the spatial coordinate in the image plane, p is the pitch of the object grating, and λ is the wavelength of incident light. This leads to the result shown in Figure 2-1 for the intensity of the 0, +1, and -1 orders

$$I(\omega) = \left| E^2 \right| \propto [1 + \sin(\omega + \Theta) + \sin(\omega - \Theta)]^2.$$ (Eq. 2-4)

If, however, the zeroth order is blocked as drawn in Figure 2-2, we end up removing the dc term we had in Equation 2-1, leaving

$$E_{F2X}(\omega) \propto \sin(\omega + \Theta) + \sin(\omega - \Theta).$$ (Eq. 2-5)

Figure 2-2: Diagram of spatial frequency doubling imaging which uses only the +1 and -1 orders
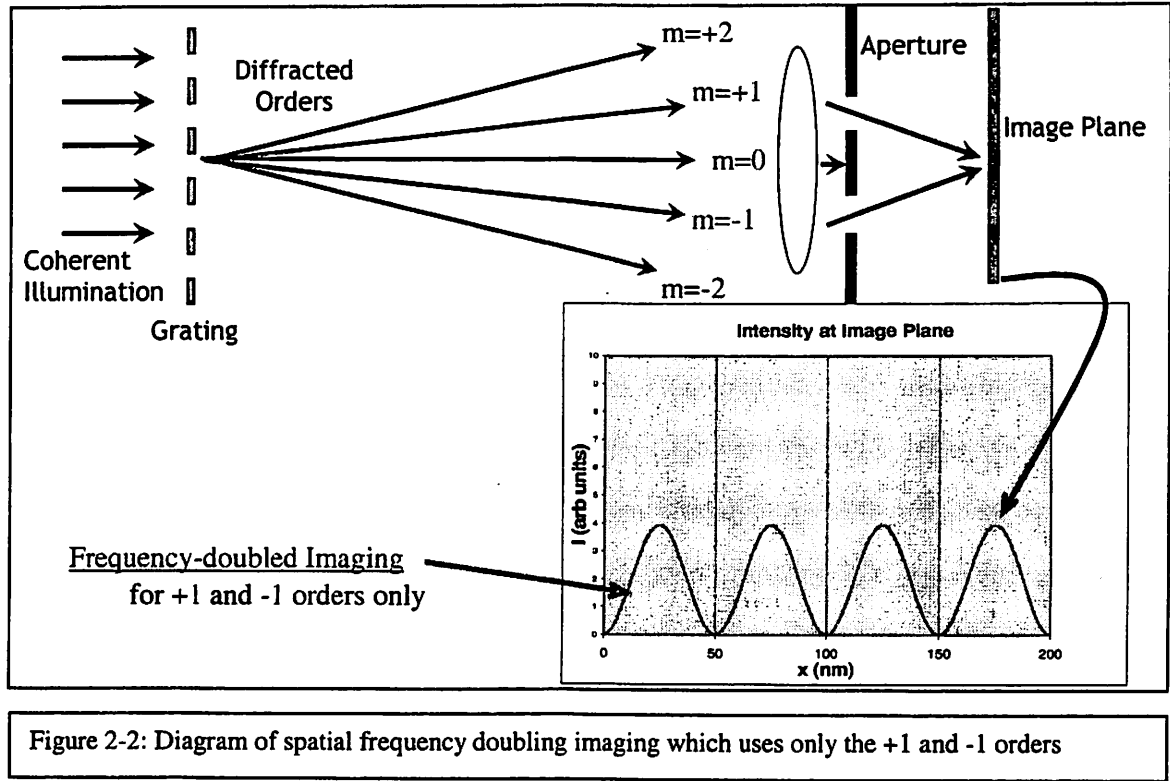
Which makes

$$I_{F2X}(\omega) = \left|E_{F2X}{}^2\right| \propto [\sin(\omega+\Theta)+\sin(\omega-\Theta)]^2 \qquad \text{(Eq. 2-6)}$$

as plotted in Figure 2-2. Combining these two imaging plots in Figure 2-3 shows clearly the high contrast achieved for the frequency-doubled case. Values for this example are p=100 nm and λ=13.4 nm.

Intensity at Image Plane

Conventional Imaging
for 0, +1, -1 orders

Frequency-doubled Imaging
for +1 and -1 orders only

I (arb units)

x (nm)
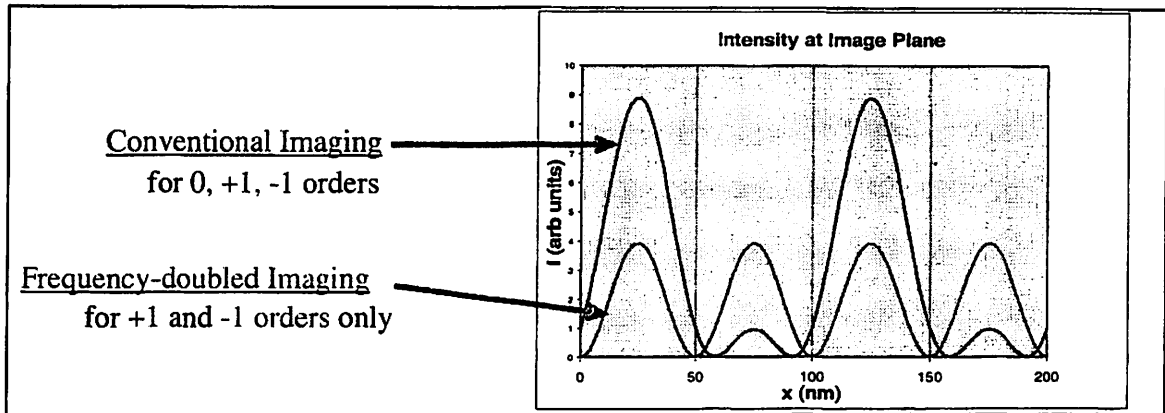
Figure 2-3: 1-D imaging plots for conventional and doubled imaging techniques.

An aperture stop was designed to block the 0th diffracted order generated by the grating while allowing the +1 and −1 diffracted orders to propagate through the system and reach the image plane. This will be discussed in Chapter 4. Chapter 5 will demonstrate experimentally this doubling effect, or what I have called the F2X system. That is short for 'spatial frequency doubling' or 'frequency two times'.

2.3 Simulations

Numerous simulations of the F2X system were run to further the understanding of the imaging properties. This included simulations on the relationship between coherence pinhole size and object grating size, aperture filter size and shape, and sensitivity to object alignment. All of these will be discussed in the next sections.

2.3.1 Full Model

The full MATLAB simulation for these experiments consisted of eight major steps:

1) Field incident on spatial coherence pinhole
2) Field interaction with pinhole
3) Propagation to object mask

23

4)	Modulation by object mask
5)	Propagation to aperture plane
6)	Modulation by aperture plane filter
7)	Imaged through 10× Schwarzschild
8)	Intensity at image plane calculated

Early on, the simulations started at step 4 – having a plane wave illuminate the object mask. This was an oversimplification of the setup since the simulated images at step 8 did not look like the real CCD image pattern. The illumination's spherical wavefront profile from the coherence pinhole gave rise to subtle features in the pupil plane image. As a consequence, steps 1 through 3 were added to the simulation.

Another important contribution to the early image problems (those with a step 4 start) was in step 4 itself due to object mask modeling. Initially, the mask was defined as a simple binary transmission mask. This was not accurate enough for the simulations. It turns out that the absorber portions of the mask let a little bit of light through. The nickel absorber actually transmits about 5% of the incident EUV light. When the mask simulations were changed to incorporate this, a good replica of the real CCD image was achieved. Figure 2-4 shows the difference between simulations with and without the pinhole diffraction compared to a CCD image of the real diffracted orders.
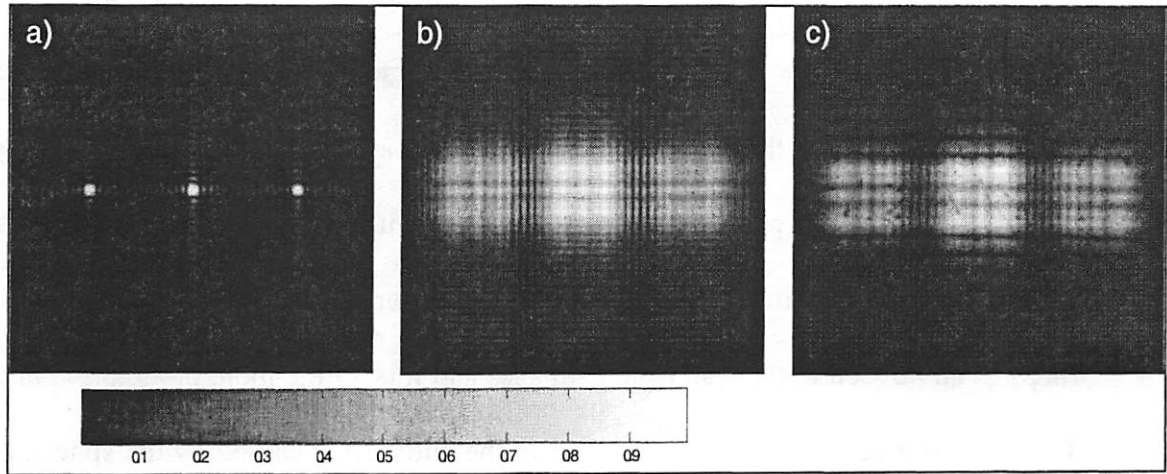
Figure 2-4: Each image contains three difracted orders in the pupil plane – 0th order in the center surrounded by +1 and -1. Each shows diffraction associated with printing 70-nm lines at the wafer. a) Simulated pupil plane image created from plane wave illumination of the object grating. b) Simulated pupil plane image created from diffracted illumination from the coherence pinhole onto the object grating. c) CCD Image of pupil plane showing actual orders on the 10×-Berkeley optic.

By using the fully extended numerical aperture, the system can theoretically achieve line widths as small as 12 nm. This can be calculated simply from the equation for the spatial frequency doubled linewidths:

$$R_{F2X} = \frac{\lambda}{4 \cdot NA}$$
(Eq. 2-7)

In the 10× Schwarzschild case, λ=13.4 nm and the largest possible NA is 0.29.

2.3.2 Aperture Size

Aperture size also plays an important role in imaging performance. Since these are coherent-based experiments there are ringing effects caused from the sharp edges of the aperture stop. This can be seen clearly in the following simulations where six configurations were analyzed. All of these simulations used a coherence pinhole of 2.0 μm.

Figure 2-5 shows the largest aperture openings of 3.3×2.8 mm and 2.2×2.8 mm (height × width). The window sizes are visible graphically when the color scale is distorted as shown in the figure. Once these orders are imaged through the 10× system, the resulting line and space pattern is shown along with two sample cutlines. In these first cases there is very little difference in imaging performance. Some slight horizontal ringing can be seen in the wafer-plane images and it is a little more pronounced in case 2. The curvature across the field, as shown in the cutlines, is caused by the spherical wave illumination of the object from the 2.0-μm coherence pinhole (see Section 2.3.4).

Figure 2-5: Simulations detailing imaging performance of dense 50-nm lines for large sized aperture openings (height × width). There is very little difference in these patterns as shown in the cutlines.
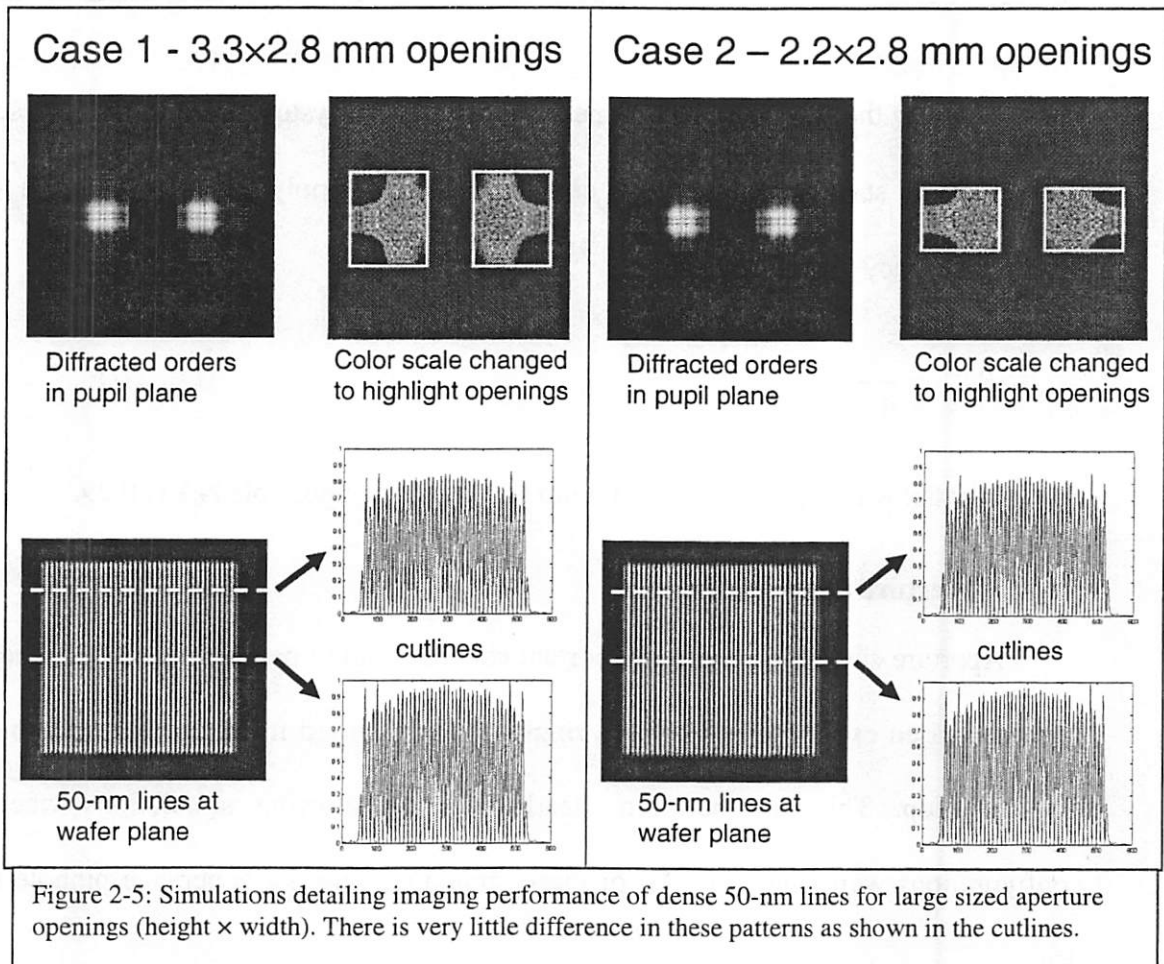
Next, in Figure 2-6, the apertures become a little smaller. But as can be seen in the cutlines, the 50 nm lines and spaces still have high contrast. Once again, there is some horizontal ringing in these cases.

Figure 2-6: Simulations detailing imaging performance of dense 50-nm lines for medium sized aperture openings (height × width). Imaging capability is still high.
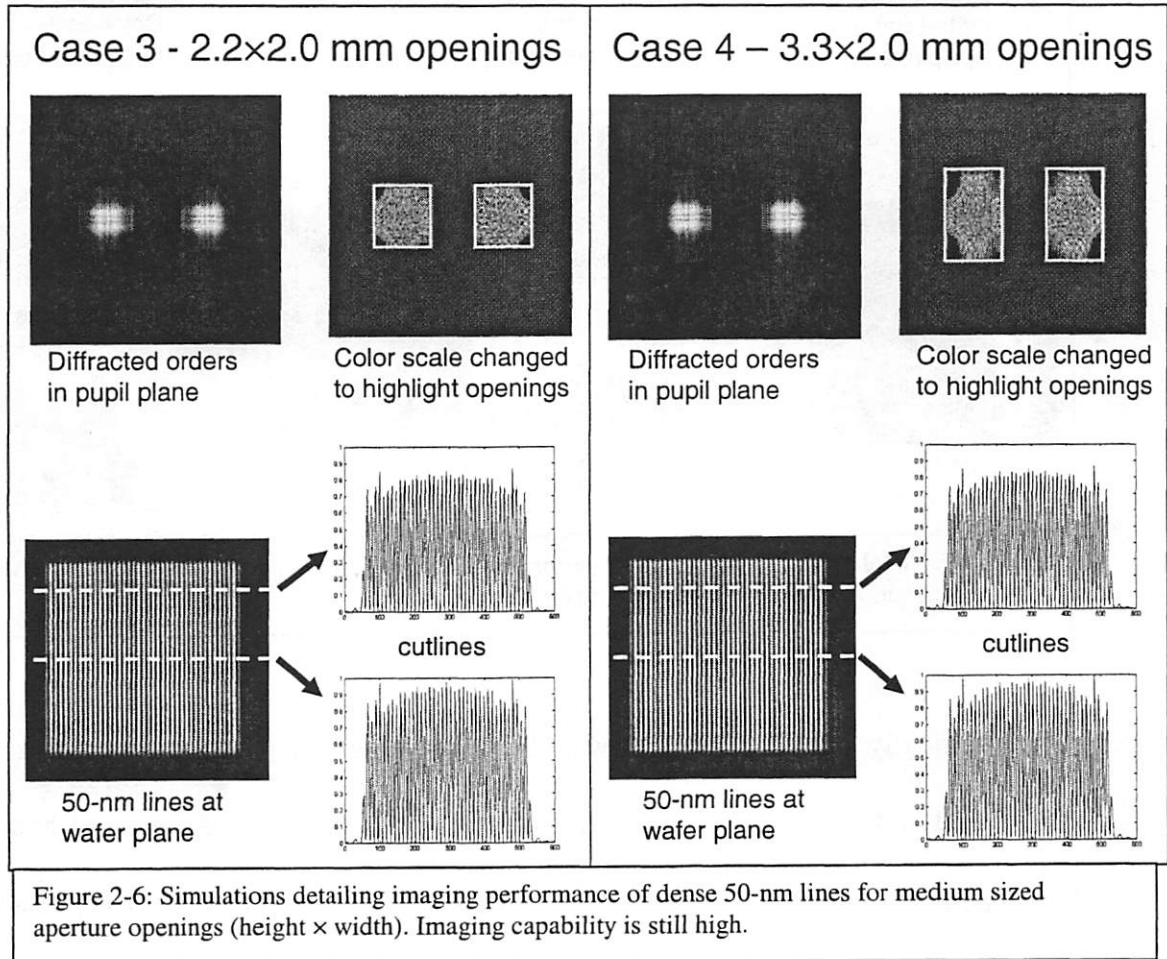
The last two cases are shown in Figure 2-7. Here the aperture sizes are approximately the same size as the diffracted orders in the pupil. Serious vertical coherence ringing is now visible in the cutlines, especially in case 6. Both cases also demonstrate very noticeable horizontal ringing in the wafer-plane images.

Figure 2-7: Simulations detailing imaging performance of dense 50-nm lines for small sized aperture openings (height × width). Imaging capability is degraded.
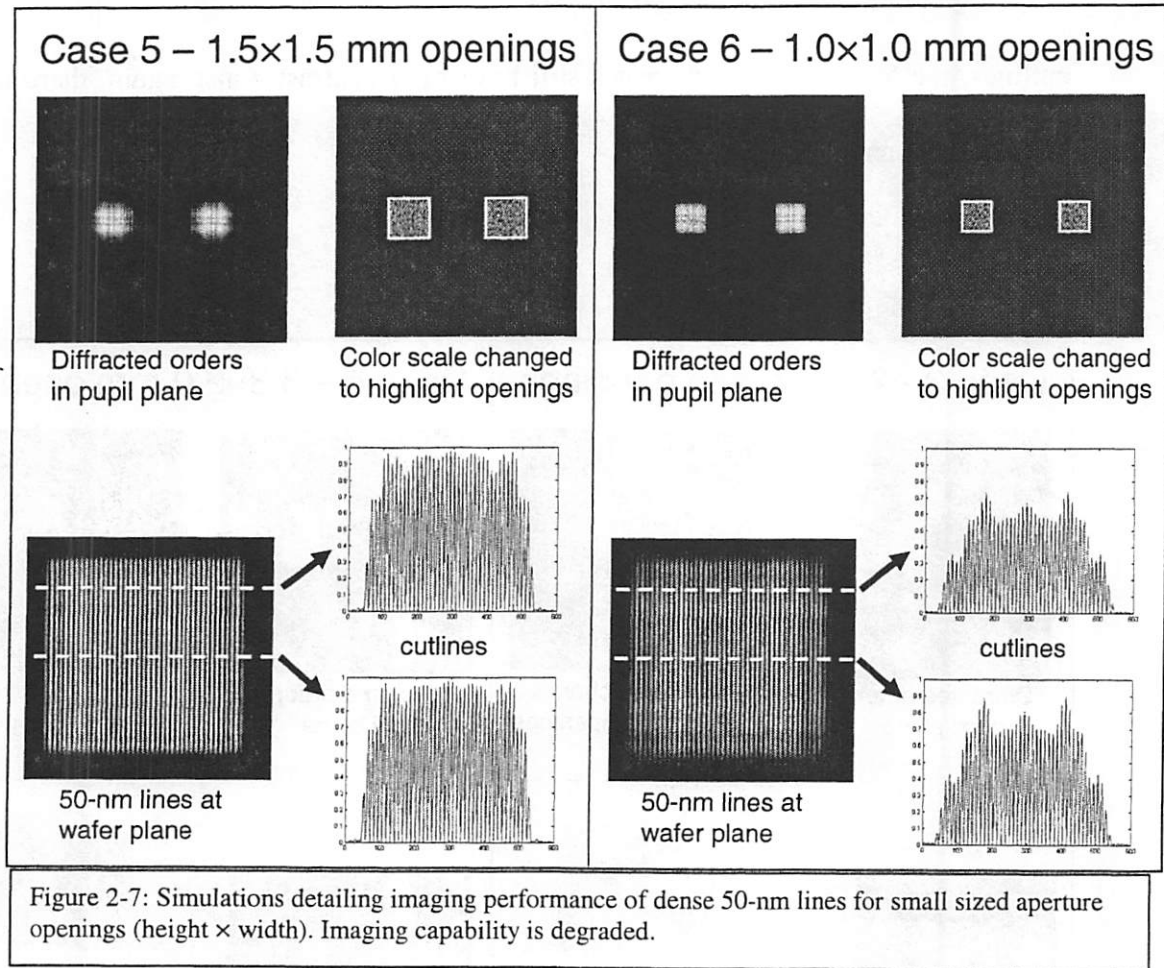
Originally, aperture openings were built just large enough to fit the orders (cases 5 and 6). After these simulations were run, the aperture stop was removed and larger openings were made. This was done in order to reduce the coherence effects associated with the aperture stops themselves.

2.3.3   Object Mask Size

Simulations were run to investigate object mask size in this system. The diffraction from the grating window sets limits for the mask. If the grating is smaller, then the printed field on the wafer will be proportionally smaller (by the 10× demagnification of the optic). Thus, for field size reasons, a larger grating is preferred. However, as the

grating gets bigger, so do the diffracted orders in the pupil plane. In fact, these orders can get so big that they start overlapping. When that happens they can no longer be filtered. If the 0th and +1 orders blend together then there is no way to use an aperture stop to block the 0th order for use in the spatial frequency doubling technique.

Figure 2-8 shows simulations using a 2-μm coherence pinhole illuminating various grating sizes. Shown for each window size are the diffracted orders in the pupil and the corresponding center cutline. The 0th order is in the center and the +1 and -1 orders are on the sides. The cutlines show clearly that a larger grating produces larger diffracted orders.
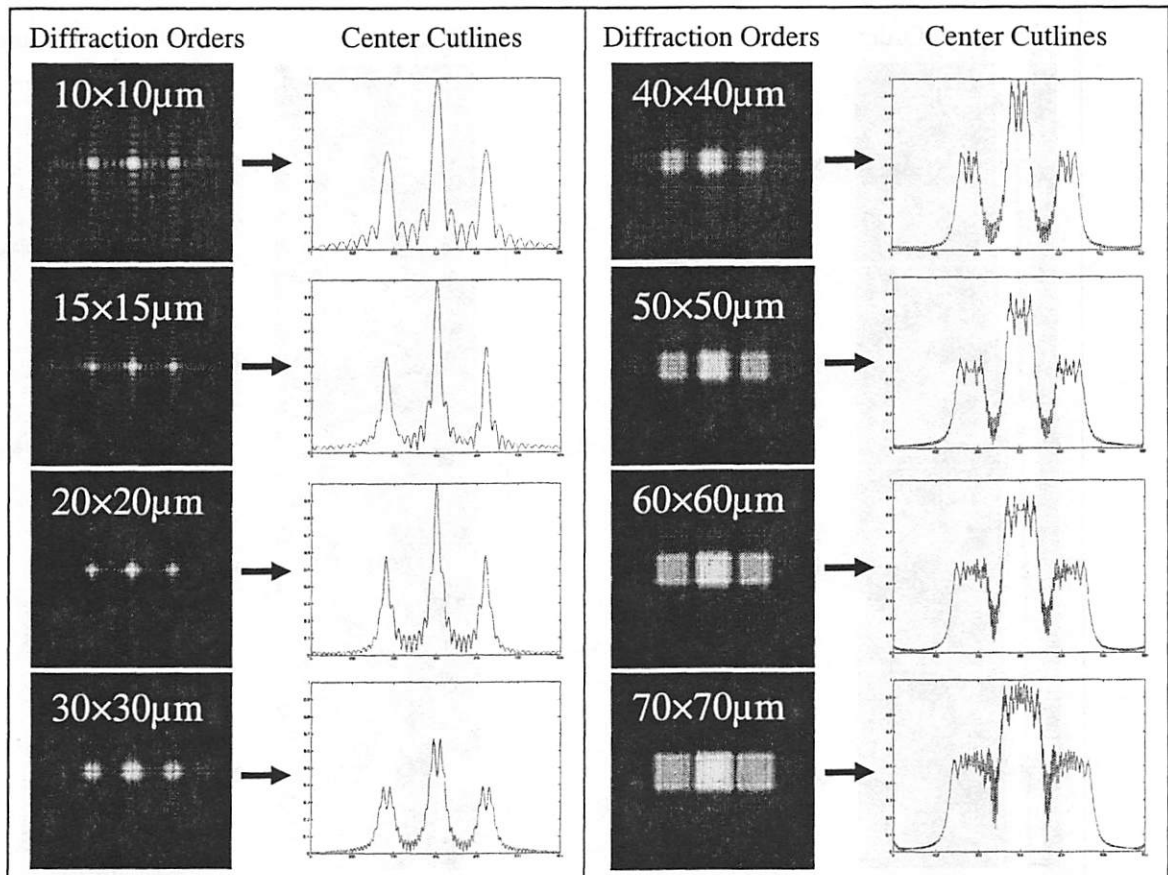
Figure 2-8: Diffraction orders for select object grating sizes. There is a **spherical wave** (from a 2-μm pinhole) illuminating the grating. Grating window dimensions are shown in white text on top of the coresponding orders. To the right of each order image is its center cutline.

29

Object size simulations can also be run with plane wave illumination of the grating. Figure 2-9 shows these calculations. In this case, as the grating window gets smaller, the diffracted orders get bigger. This makes sense when thinking about common diffraction systems. As an object gets smaller, light will diffract at a larger angle.

The reason that this same phenomenon is not seen in Figure 2-8 is because there are two competing effects. First, spherical wave illumination makes the orders larger in the pupil plane. The phase curvature hitting the grating keeps diffracting even more. This is countered by the second effect, where the larger the grating window the less diffraction.
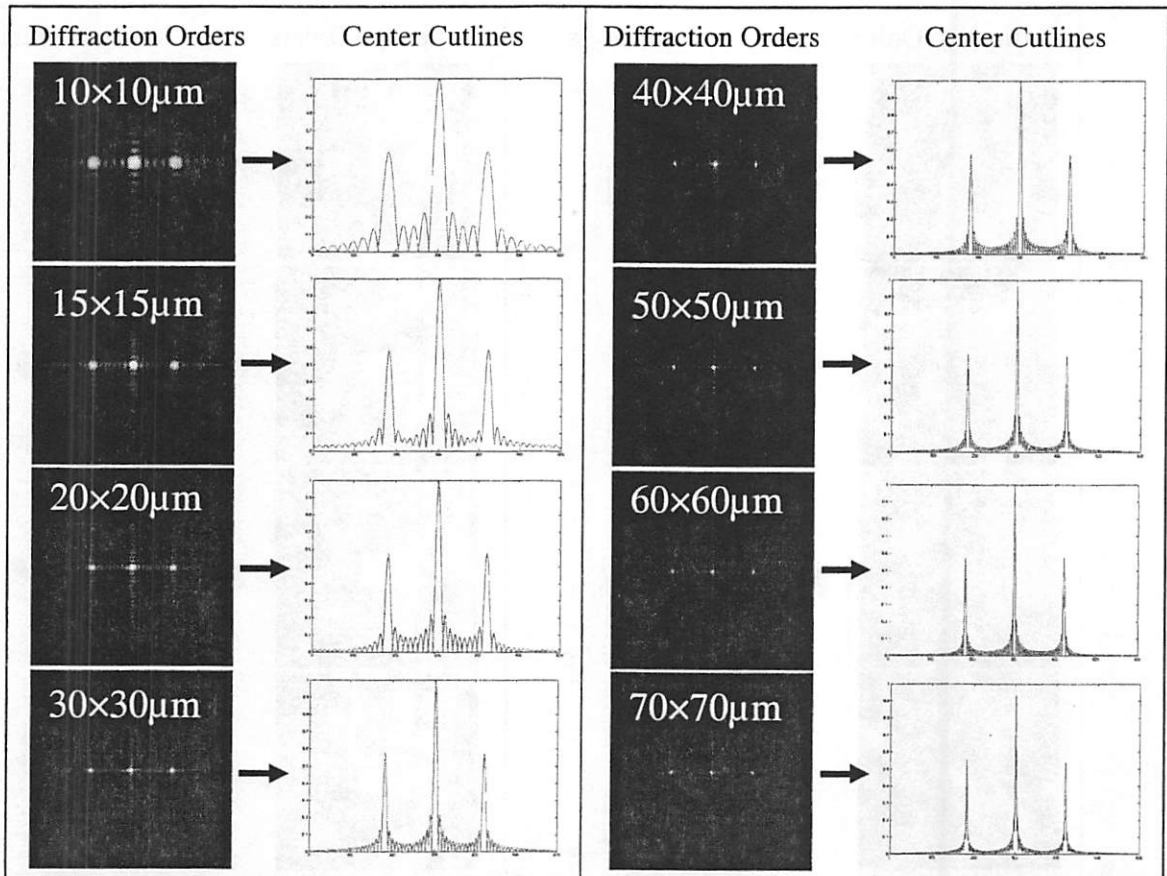
Figure 2-9: Diffraction orders for select object grating sizes. There is a **plane wave** illuminating the grating. Grating window dimensions are shown in white text on top of the coresponding orders. To the right of each order image is its center cutline.

There should be a point then where these two effects meet to form the smallest diffraction size possible in the pupil plane. To investigate this, Figure 2-10 compiles data from Figures 2-8 and 2-9. The width of each diffracted order was measured as a FWHM value (Full Width at Half the Maximum). It is called the footprint size since it is the size of the diffracted orders in the pupil plane. The pupil plane coincides with a mirror surface in the optic.

Figure 2-10: Diffracted order sizes in the pupil plane for two different illumination schemes. Window size is defined as the opening along one side of the object grating.
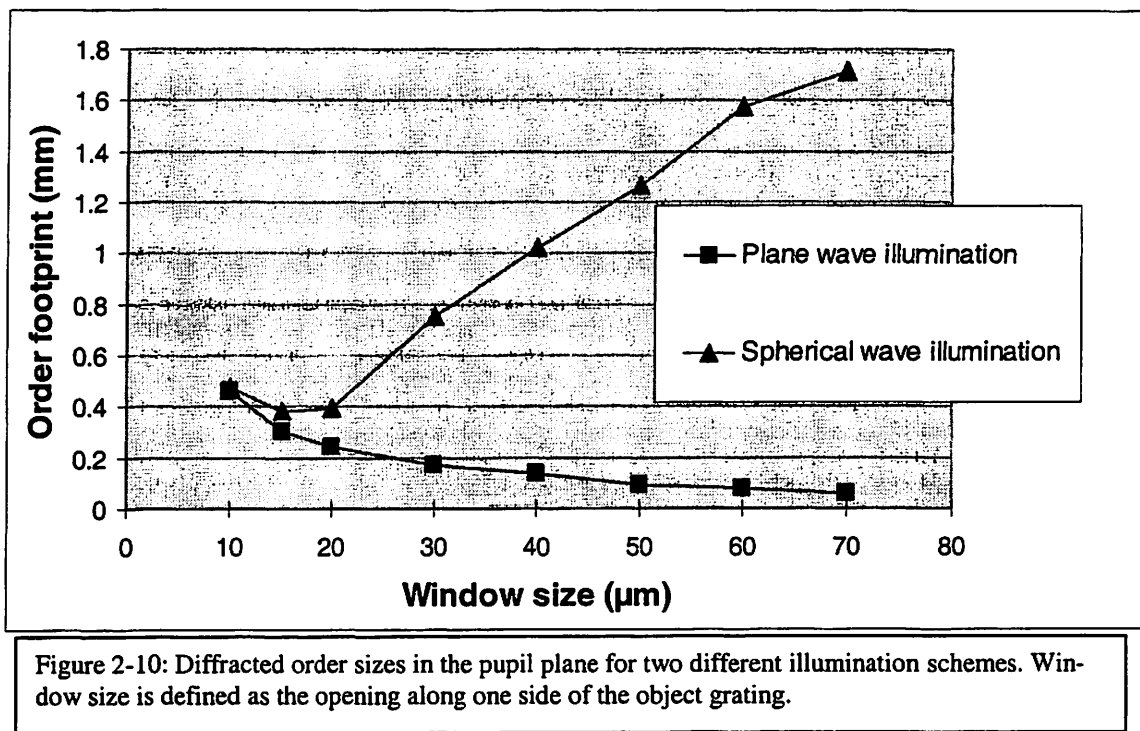
As Figure 2-10 shows, there is in fact a minimum footprint size in the spherical wave case for gratings around 15-20 μm on a side. Plane wave illumination also behaves as expected where a smaller grating window will create larger diffracted orders. It is also reassuring to see in these simulations that the spherical wave case starts following the plane wave case at 10 μm. The plane wave illumination case is the diffraction limit. If the spherical wave case produced a smaller footprint that would signal a problem with these

31

simulations. In this case at the 10 μm point, the grating window is so small that the spherical wave essentially looks like a plane wave. There is very little phase variation anymore over the window.

As mentioned above there is a tradeoff. The smaller the order footprints on the mirror surfaces then the less any mirror roughness will change the orders. However, the smaller footprints will decrease field size as well. A 40-μm window creates diffracted orders that are 1 mm in the pupil plane and creates a field on the wafer of 4×4 μm. A 20 μm window creates orders that are 0.4 mm and a field that is only 2×2 μm. It would not make sense to go to a 15×15 μm window since there is virtually no more reduction in order size. Experimentally, object masks were built for these experiments at 40 μm to get the larger field size. Later, multi-pitch masks used 20 μm windows for each feature size. Four of these fit inside a 40 μm square window. This configuration still gave a 4×4 μm field but each of the four pitches produced smaller orders in the pupil plane.

2.3.4   Coherence Pinhole Size

This section continues to look at diffraction. This time the size of the coherence pinhole, positioned before the object grating, is varied. The smaller the pinhole size, the more diffraction. That means there will be less phase variation and less amplitude variation in the field when it illuminates the mask. The downside is that there will be less light transmitted through the system.

Figure 2-11 shows the difference in imaging 50 nm lines and spaces using two different sized pinholes. One is 2 μm in diameter and the other is 0.5 μm.

Figure 2-11: Imaging performace for 50 nm dense lines and spaces for two different pinhole sizes. The object grating window is 40×40 µm.
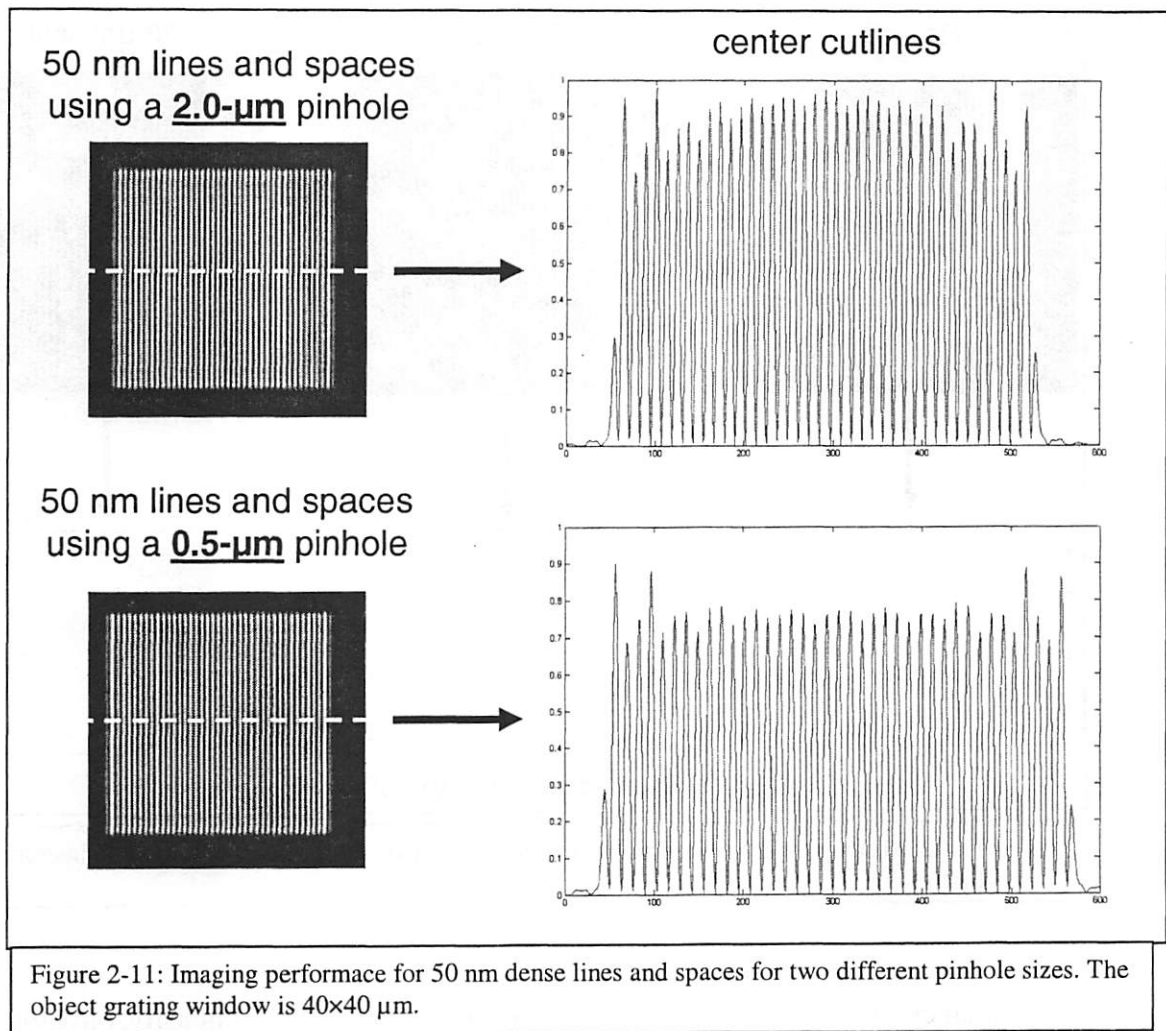
As can be seen in the cutlines, the contrast of the lines and spaces is slightly more even in the 0.5 µm case. Initially, experiments were done using a 2-µm pinhole. Later, during a series of system upgrades, a 0.5-µm pinhole was installed.

2.3.5 Object Alignment

If the object is not placed in the center of the pinhole diffraction spot then the misalignment will play a significant role in imaging degradation. Figure 2-12 compares a completely centered system to ones that have been misaligned by 10 and 20 µm.

No shift	10-µm shift	20-µm shift

Vertical cutlines down along the 50-nm features

Figure 2-12: Misalignmnet between the 2-µm pinhole and the object grating can result in intensity rolloff for each line.
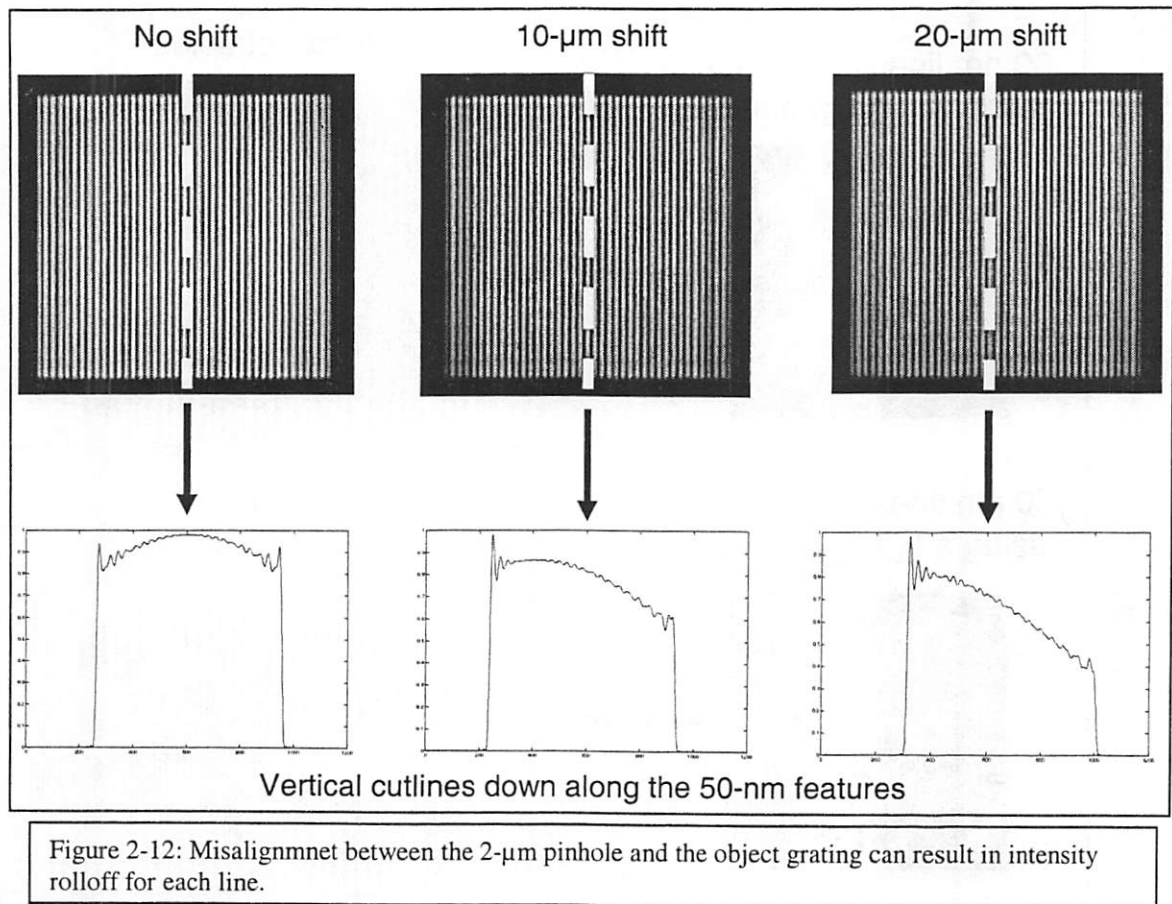
Each cutline follows an individual linewidth and show the intensity variation along the 50-nm feature. It is evident that alignment is important for imaging success in this system. This simulation helped build the case for insitu alignment capability for these experiments. That capability was added during system upgrades.

2.4 Similar Techniques

There are two other methods that have been used by others to print small features into photoresists for testing and development purposes. Both utilize interference to achieve this aim but do so in different ways. Their advantages are that they are essentially maskless and lens-less. They are also much simpler than the F2X method and as such,

they don't have the extensions to actual lithographic systems that spatial frequency doubling has. All three methods have great depth of focus properties. These other two methods will be discussed in the next two sections.

2.4.1 Two Beam Interference Lithography

Interferometric Lithography (IL) uses the sinusoidal standing wave created by two intersecting coherent light beams [4]. When a photoresist-coated wafer is set in the intersection plane then a periodic line and space pattern is exposed in the resist. As seen in Figure 2-13 the pitch printed will be

$$P_{IL} = \frac{\lambda}{2\sin\theta}.$$
(Eq. 2-8)

Interferometric Lithography
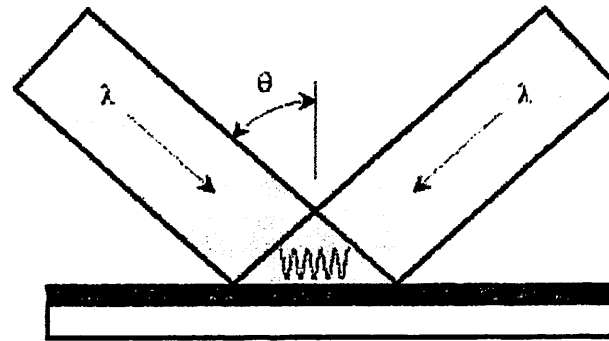
$$\text{period} = \frac{\lambda}{2\sin(\theta)} \qquad 135 \text{ nm at } 257 \text{ nm/}80^{\circ}$$

Fugre 2-13: Interferometric Lithography Diagram [4]

This configuration allows for printing near λ/2 and, as mentioned above, is maskless and lens-less which helps reduce cost and aberrations. This technique also allows for simple control of the aerial image contrast since the intensities of the intersecting beams can be varied. Unfortunately, this system is difficult to implement at EUV wavelengths.

2.4.2 Lloyd Mirror

The Lloyd mirror technique is a simple and relatively inexpensive way to print small features. It requires a temporally and spatially coherent source of EUV radiation. Figure 2-14 shows a schematic of the system. By using a grazing incidence optic one can create a phase difference between the normally incident beam and the reflected one [5]. This path length difference will cause interference fringes in the intersection volume. By

INTERFERENCE
FRINGE PATTERN

WAFER

GRAZING
INCIDENCE
MIRROR

INCIDENT
BEAM
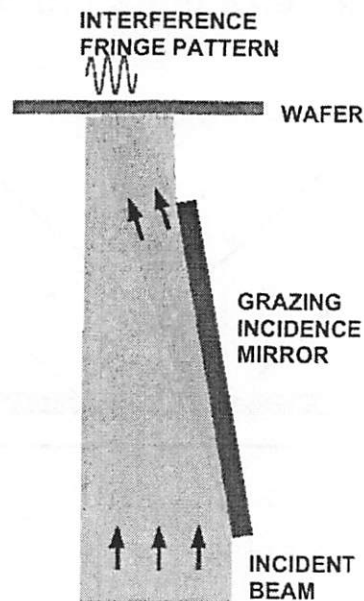
Figure 2-14: Diagram of Lloyd's mirror [6]

36

placing a resist-coated wafer in this volume, a periodic line and space pattern will be transferred.

The equation for the printable feature size is given by

$$P_{LM} = \frac{\lambda}{\sin\theta_1 + \sin\theta_2}.$$ (Eq. 2-9)

where θ_1 and θ_2 are the two angles from normal to the wafer plane [6]. Using angles in the range of 2-10 degrees will give features with sizes from 20-100 nm. Contrast is affected somewhat by the imbalance between the two beams. But with a suitably designed multilayer reflector, fringe patterns can be printed. Since this system has one beam reflecting off a mirror, the difference between the two field strengths causes a reduction in contrast. The spatial frequency doubling method uses balanced fields to achieve higher contrast. Also, in the F2X system, multiple pitches can be printed by simply changing the object mask. The Lloyd mirror system would require a different mirror (curved or stepped).

2.5 Conclusions

By using the F2X imaging system with the spatial frequency doubling technique, I can print well defined 50 nm features and smaller using a 10× Schwarzschild optic designed for only 100 nm lines. The reasons are twofold. First, I limit the sizes and orientations of the features I print. By imaging dense features in a single orientation, I reduce the space needed in the pupil. Secondly, by additionally blocking the zeroth order and reducing the space on the pupil further, I can get an additional factor of two in demagnification from the spatial frequency doubling.

37

Aberrations would be too great over the whole 10× pupil for lithography – it wasn't designed for full NA imaging. However, I can print a small range of frequencies in small fields. The doubling is a nice extra but it would not mean much if it didn't also allows the use of "more" of the NA. By compromising on the field of view this system makes effective use of a larger area of the optic.

This chapter discussed the theory and simulations used to help design the experiments. These included aperture size, object mask size, coherence pinhole size, and object alignment. Several other simulations will be shown in Chapters 3, 5, and 6.

The spatial frequency doubling technique shares similarities to two other methods described. The Lloyd mirror is simpler from a component and alignment standpoint. However, the technique used in this experiment is advantageous because it will give higher contrast due to the inherent field balancing of the two incoming orders. As mentioned above, all three methods have great depth of focus due to their interferometric nature.

Coherence is a double-edged sword for these experiments. In order to use the spatial frequency doubling and extend the limits of these optics, coherent imaging must be used. However, coherence will exaggerate any wavefront errors and it will add ringing from edges (and defects as shown in Section 5.6). Overall, this allows printing of small features but also enhances nonuniformities in the fields.

This research started by taking in-house interferometry knowledge and equipment and expanding on it. Minor modifications were needed initially in order to use the 10× optic in a novel way for high contrast aerial imaging. As the project grew in scope the

system was upgraded several times. The next chapter will discuss in more detail the EUV optics used to do these experiments. The chapter after that will detail the system and the upgrades.

2.6 References

[1]   T. Jewell and D. White, "Spatial frequency doubling lithography (SFDL) of periodic structures for integrated optical circuit technology," Journal of Lightwave Technology, Vol. 7, No. 9, 1386-1393 (1989).

[2]   T. Jewell and D. White, "Integrated optical circuit grating fabrication using 0.25 mu m optical lithography," Proc. SPIE, Vol. 993, 48-57 (1988).

[3]   B. Saleh and M. Teich, Fundamentals of Photonics, John Wiley & Sons, Inc., New York, 1991.

[4]   W. Hinsberg, F. Houle, J. Hoffnagle, M. Sanchez, G. Wallraff, M. Morrison, and S. Frank, "Deep-ultraviolet interferometric lithography as a tool for assessment of chemically amplified photoresist performance," J. Vac. Sci. Technol. B, Vol. 16, No. 6, 3689-3694 (1998).

[5]   J. Shin, G. Han, Y. Ma, K. Moloni, and F. Cerrina, "Resist line edge roughness and aerial image contrast," J. Vac. Sci. Technol. B, Vol. 19, No. 6, 2890 (2001).

[6]   H. Solak, D. He, W. Li, S. Singh-Gasson, F. Cerrina, B. Sohn, X. Yang, and P. Nealey, "Exposure of 38 nm period grating patterns with extreme ultraviolet interferometric lithography," Applied Physics Letters, Vol. 75, No. 15, 2328-2330 (Oct 1999).

[7]   M. Wei, D. Attwood, T. Gustafson, and E. Anderson, "Patterning a 50-nm period grating using soft x-ray spatial frequency multiplication," J. Vac. Sci. Technol. B, Vol. 12, No. 6, 3648-3652 (1994)

[8]   M. Wei, E. Gullikson, J. Underwood, T. Gustafson, and D. Attwood, "White-light spatial frequency multiplication using soft x-rays," Proc. SPIE, Vol. 2516, 233-239 (1995).

3   EUV Optics

3.1   Introduction

There have been many iterations of multilayer-coated optics used in EUV research. First, the 20× Schwarzschild demagnification tool used in the early 1990's printed rough 100 nm features using a laser plasma source [1]. Most recently, a 0.3 NA tool with low mirror roughness attached to an undulator beamline has been used to print dense 30-nm features [2]. In between there have been variations on the 10× Schwarzschild model and the two Engineering Test Stand (ETS) alpha tools. The ETS is a 4× tool that has an NA of 0.1 and is comprised of 4 mirrors. It was designed to print 100 nm features in a 1-inch arc field [3]. The ETS has mimicked a commercial lithography setup by printing images while scanning the EUV photons across the mask. These non-static exposures are still at least twice as big as will be required for EUV lithography commercialization, but it does demonstrate necessary advancements in implementation. The research covered in this thesis utilized two tools: the 10× Schwarzschild optics and the newest 0.3 NA optic called the Micro Exposure Tool (MET).

The work described above highlights EUV lithography progress in the United States. There are two other consortiums also working on EUV technologies. A European group is working on a 0.25 NA imaging system [12]. This system is still in development with a significant emphasis on optic polishing and source power. Japan is also working on an EUV lithography tool. It is a 0.3 NA optic that is similar to the MET except that it

uses aspherical mirrors [13]. At this time, the most imaging progress has been made by the US National Laboratories.

3.2 10× Schwarzschild Optics

Two-mirror, 10×-demagnification Schwarzschild optical systems have been used extensively in EUV lithography research. Two subjects of particular interest have been phase-shifting point diffraction interferometry (PS/PDI) [4] and microstepper imaging [5,6]. In these 10× EUV optical systems, a well-corrected off-axis circular sub-aperture with an NA ranging from ~0.07 to 0.09 is selected using an aperture stop. The full pupil of the system is annular with an NA of 0.29. Conventionally, the smaller sub-aperture is used in order to minimize wavefront aberrations over a larger field of view than would be allowed using the full annular pupil. The 0.08 NA system has a theoretical resolution limit for dense features of about 100 nm. By using the spatial frequency doubling technique, however, this limit can be surpassed and even smaller line and space features can be printed. A scaled diagram of the Schwarzschild setup is shown in Figure 3-1. This figure shows the system operating at its highest NA where the +1 and -1 orders hit the edges of the two mirrors. For larger features the system is operated in an off-axis configuration and an aperture stop placed on the primary mirror is used to physically block the 0th order.
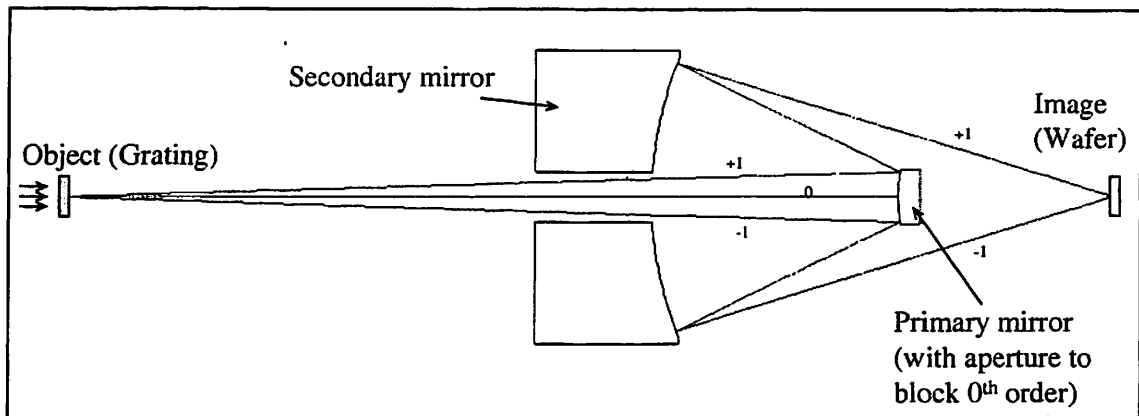
Figure 3-1: Scaled schematic of Schwarzschild objective.

There have been several iterations of the 10× optics. This research used three models. The first, called 10×-Berkeley, was a first-generation optic. Second was 10×-B2, a third-generation optic. Lastly was 10×-Intel, the newest system and the fourth generation, designed to be used in the F2X imaging station. The mirror roughness requirements for 10×-Intel, specified from MATLAB simulations, are discussed in the next section.

3.2.1 Mirror Surface Roughness

In order to get better performance out of this imaging technique, a higher quality optic was necessary. Several possibilities were investigated. One suggestion was to remove the multilayers of an existing optic and recoat the substrates with newer multilayers using more recent technology. This would have been the most economical option, but the quality of the substrates after multilayer removal could not be guaranteed. The best option, fabricating new substrates for coating, became a reality when Intel showed interest in using this tool for their own resist research. At that point, computer

simulations were run to get a fuller understanding of the impact mirror roughness would have on F2X experiments.

In general, low-spatial frequency roughness contributes to the blurring of features. Mid-spatial frequency roughness adds to small angle scattering that effects contrast. High-spatial frequency roughness is large-angle scattering which does not expose the photoresist but the associated loss reduces power throughput in the system [7].

It was possible to model in MATLAB both the low spatial frequencies (figure) and most mid spatial frequencies (flare). High-spatial frequency modeling required more memory than a desktop computer could handle. Since these high-spatial frequencies do not degrade image quality, they are not critical to the simulations. The spatial frequencies for figure in the 10× system are anything below 1 mm^{-1}. Mid spatial frequencies cover the range from 1 mm^{-1} to 1 μm^{-1}. Anything above 1 μm^{-1} are high spatial frequencies. Typically, mirror surface roughness is measured with optical profilers for low spatial frequencies, EUV scattering results for mid-spatial frequencies, and an atomic force microscope (AFM) for high-spatial frequency data.

Mirror roughness, or surface roughness, is usually measured as a power spectral density (PSD). An example of the PSD for the 10×-B2 optic is shown in Figure 3-2 [8].

Example PSD (10x B2 primary)

			RMS roughness (nm)
Figure (nm)	Region 1	up to 1 /mm	0.57
MSFR1 (nm)	Region 2	1 - 2.2 /mm	0.17
MSFR2 (nm)	Region 3	2.2 - 600 /mm	0.25
MSFR3 (nm)	Region 4	600 - 1000 /mm	0.05
HSF (nm)	Region 5	> 1000 /mm	0.21

Figure 3-2: Power spectral density plot for the 10×-B2 optic. Roughness values are shown in the table on the right.
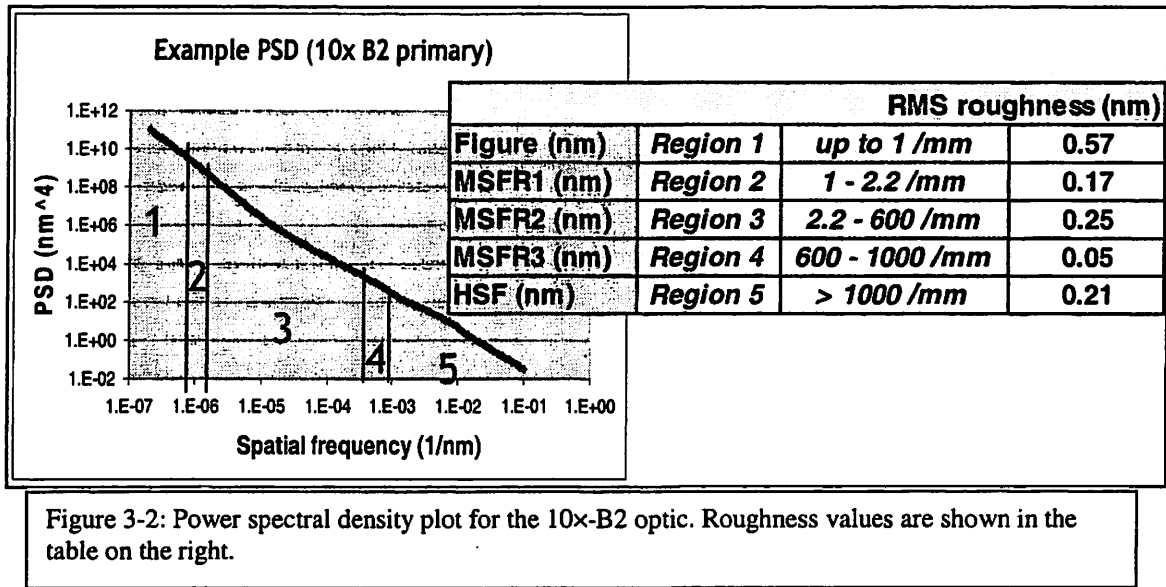
The simulation procedure followed these steps:

1) Created a power spectral density (PSD) plot

2) PSD conversion to a 2-D roughness field

3) Add roughness as a phase deviation in the pupil plane

4) Simulate imaging system as in Chapter 2

The power spectral density of a surface is proportional to the square of the Fourier Transform of the surface [9]. Therefore, a rough surface can be created by working backwards. First, a PSD is created and the strength of the figure and flare amplitudes are programmed. The square root of the PSD is taken and a random phase is added over a plane. Then by reverse transforming this field a surface map is created. The MATLAB code contained a variable to change the relative strength of the figure and flare. Figure 3-3 shows how this multiplier could change the strength of the figure with respect to the flare. Values range from figure being one fifth the strength of the flare all the way to figure being six times the strength of the flare.

45

Figure 3-3: The ratio of figure strength to flare strength as determined by a multiplier variable in the PSD calculation.
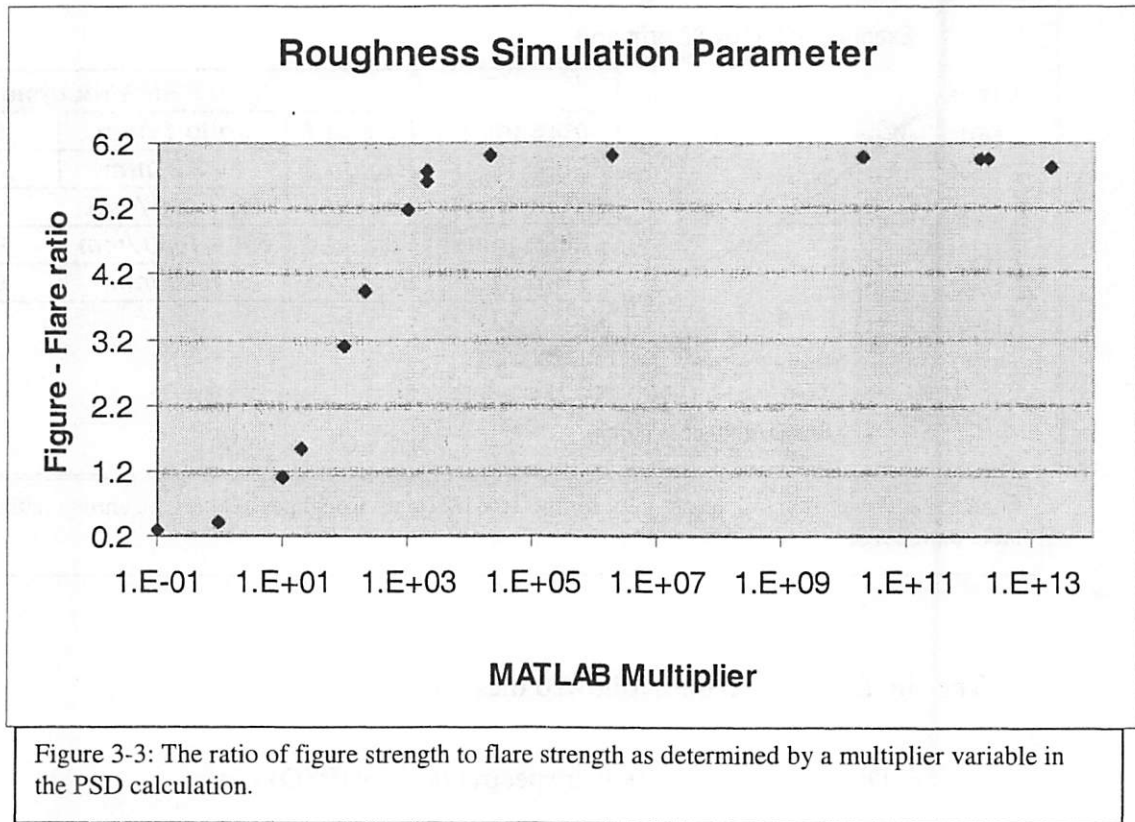
The surface roughness map that is created in MATLAB acts as a phase variation from a perfect imaging system. This phase map is placed in the aperture plan and distorts the phase information of the diffracted orders. This phase deviation in turn creates field nonuniformities in the image plane.

Three sample PSD plots are shown in Figure 3-4 with their corresponding surface roughness. The same phase map was used for all three cases to show how the PSD alone can change the surface structure.

Power Spectral Density Plots

1.6e-7 to 6.0e-5 (1/nm)   1.6e-7 to 6.0e-5 (1/nm)   1.6e-7 to 6.0e-5 (1/nm)

Corresponding Surfaces

Figure 3-4: Three PSD plots and their corresponding created surfaces using the same phase map. On the left, a relatively flat PSD creates a surface with balanced roughness. In the center, as the figure is increased relative to the flare, more long range roughness appears. On the right, as this imballance grows, all the mid-spatial frequencies are dominated by the lower frequencies.

Using this technique, simulations were run to see what limits needed to be set to help decrease field nonuniformities. The object consisted of a 40-μm square mask containing a 2-μm period grating. This setup produced 50-nm lines and spaces in the image plane. Lastly, a 2-μm pinhole illuminated the object and 3.3×2.8-mm aperture openings were used in the pupil plane. By varying the amplitudes of the mirror surface errors (the roughness phase map) in the pupil plane, imaging performance was investigated.

Figure 3-5 shows the results of keeping figure below 0.2 nm and sweeping the mid-spatial frequency roughness (MSFR) from 0.6 to 0.1 nm rms. There are two surfaces

shown. Each surface was created from a different random phase map added to the generated PSD. As can be seen, the nonuniformities in the field smooth out around 0.1 nm for both surfaces. The field-contrast variation ranges from 22% when MSFR is 0.6 nm to 5% when MSFR is 0.1 nm. In addition, the linewidth-intensity difference ranges from 50% when MSFR is 0.6 nm to only 14% when MSFR is 0.1 nm.
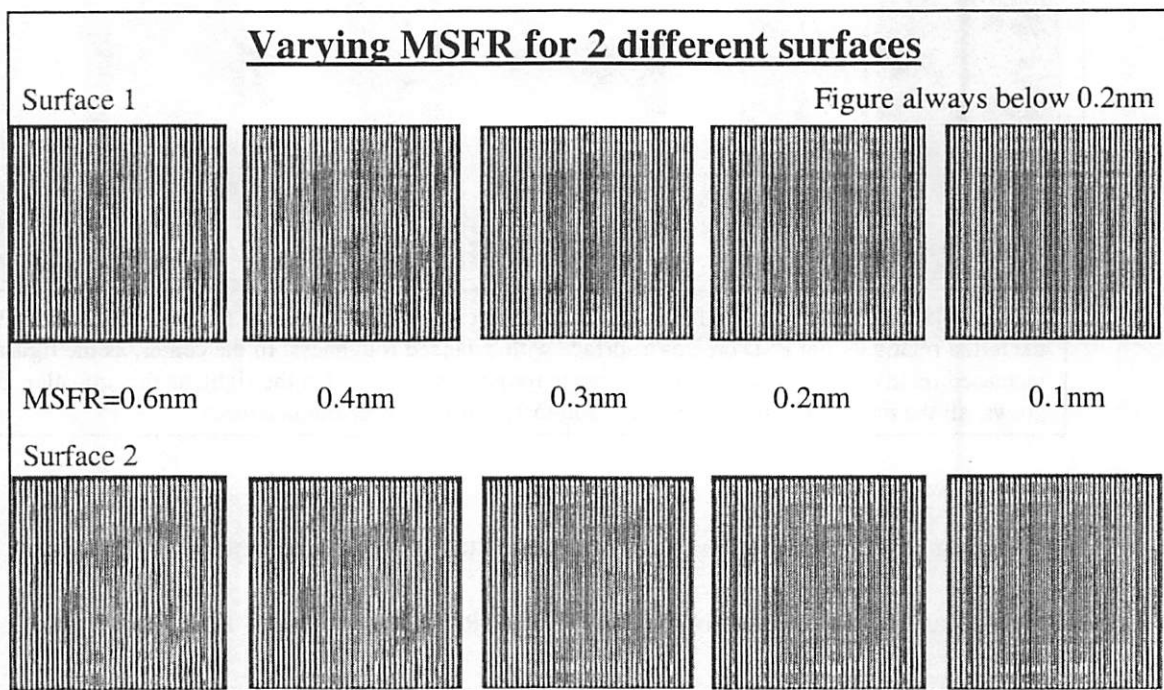
Figure 3-5: Imaging performance of 50-nm dense lines and spaces when MSFR is added to the optic. As MSFR decrease the field nonuniformities decrease. The difference between these two surfaces are from different randomly generated phase maps.

Simulations were also run where MSFR was held constant and figure was varied. Figure 3-6 shows three cases for three different MSFR values. The amount of figure roughness varies by quite a bit in each case but the image pattern changes very little. This is as expected for the F2X experiments. Since only small regions of the optic are being used during imaging, figure roughness will only add a phase difference between the

orders. That phase difference will show up as a change in focus rather than impact the imaging. Also shown in Figure 3-6, whatever field nonuniformities are evident at high figure, they are still showing up at low figure. As far as mirror roughness is concerned, mid-spatial frequencies are the main contributor to the field nonuniformities. In Figure 3-6, field-contrast variations are 17%, 9%, and 5% (top to bottom). The linewidth-intensity differences are 45%, 20%, and 14% (top to bottom).

MSFR = 0.40nm

Figure =2.10nm   Figure = 0.43nm

MSFR = 0.20nm

Figure = 1.05nm   Figure = 0.22nm

MSFR = 0.10nm

Figure = 0.53nm   Figure = 0.11nm

Figure 3-6: Imaging performance for 50-nm dense lines and spaces as figure is varied significantly. Three different MSFR values are shown.
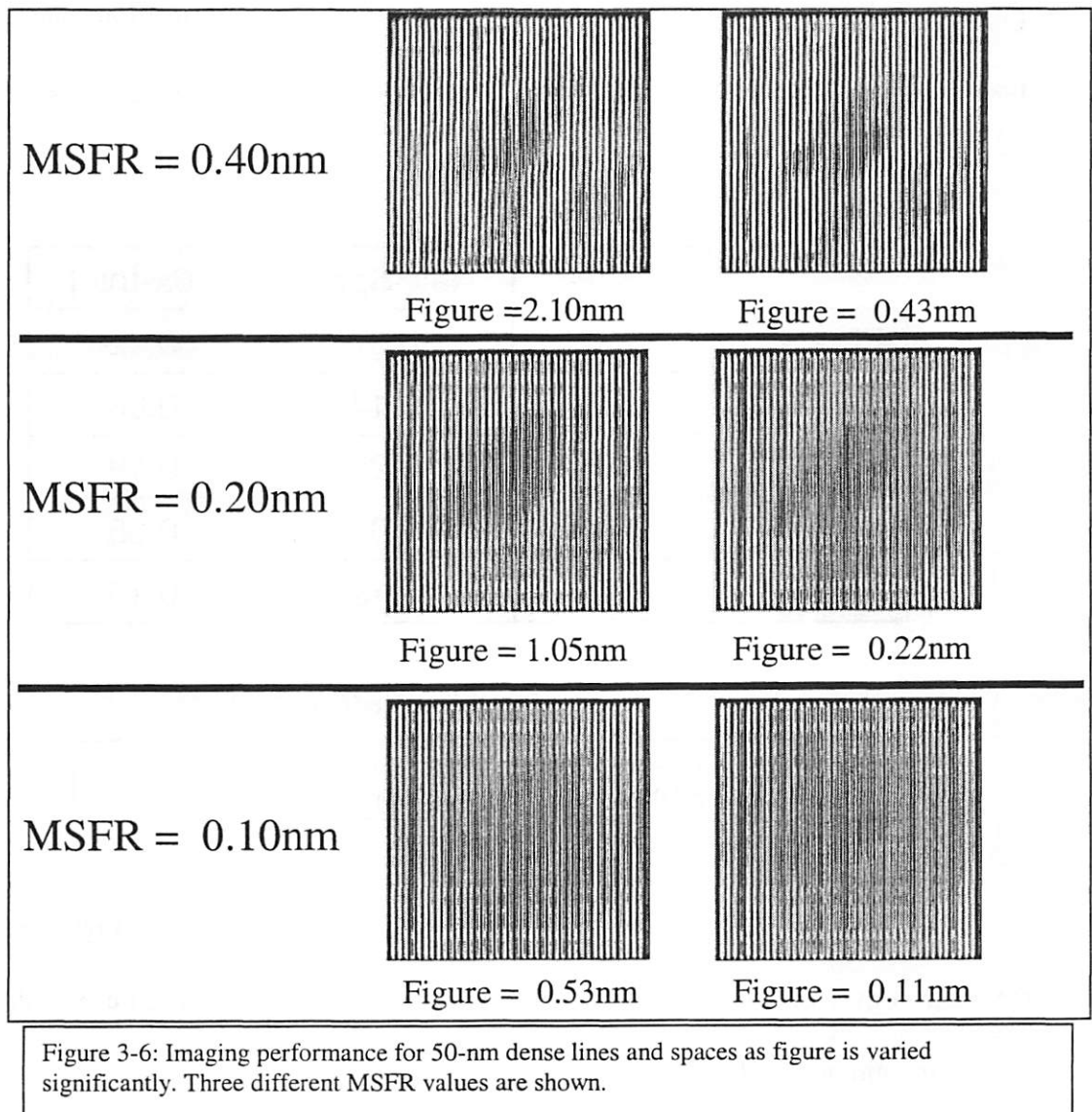
Based on discussions with Sang Hun Lee of Intel it was decided to split up the mid-spatial frequency roughness into three parts. This is because select regions of the mid-spatial frequency roughness were the dominating concern when printing using the F2X technique. Figure 3-2 showed this separation. Instead of asking for a new optic that had 15-20% improvement over the mid-spatial frequency range of the 10x-B2 optic, more stringent requirements were placed in the first MSFR range (region 2 in Figure 3-2). Figure 3-7 shows the 10x-B2 data compared to the requested specifications and the actual results. Key improvements were made in the necessary spatial frequency ranges.

	10x-B2	New Specs	10x-Intel
Figure	0.57	0.57	0.42
MSFR1	0.17	0.14	0.08
MSFR2	0.25	0.20	0.18
MSFR3	0.05	0.04	0.05
HSF	0.21	0.18	0.19

all values are nm rms

Figure 3-7: Chart showing 10x-B2 values, the agreed upon vendor specifications, and the actual optic results before cutting.

PSD plots for the 10x-Intel optic are shown in Figure 3-8 and 3-9. Figure 3-8 shows the metrology tools that were used to make the measurements. Figure 3-9 shows the composite and best-fit lines of the data.

Figure 3-8: PSD plot of 10×-Intel showing metrologies used in the measurements. [10]

Figure 3-9: PSD data for 10×-Intel showing composite and best fit plots. [10]
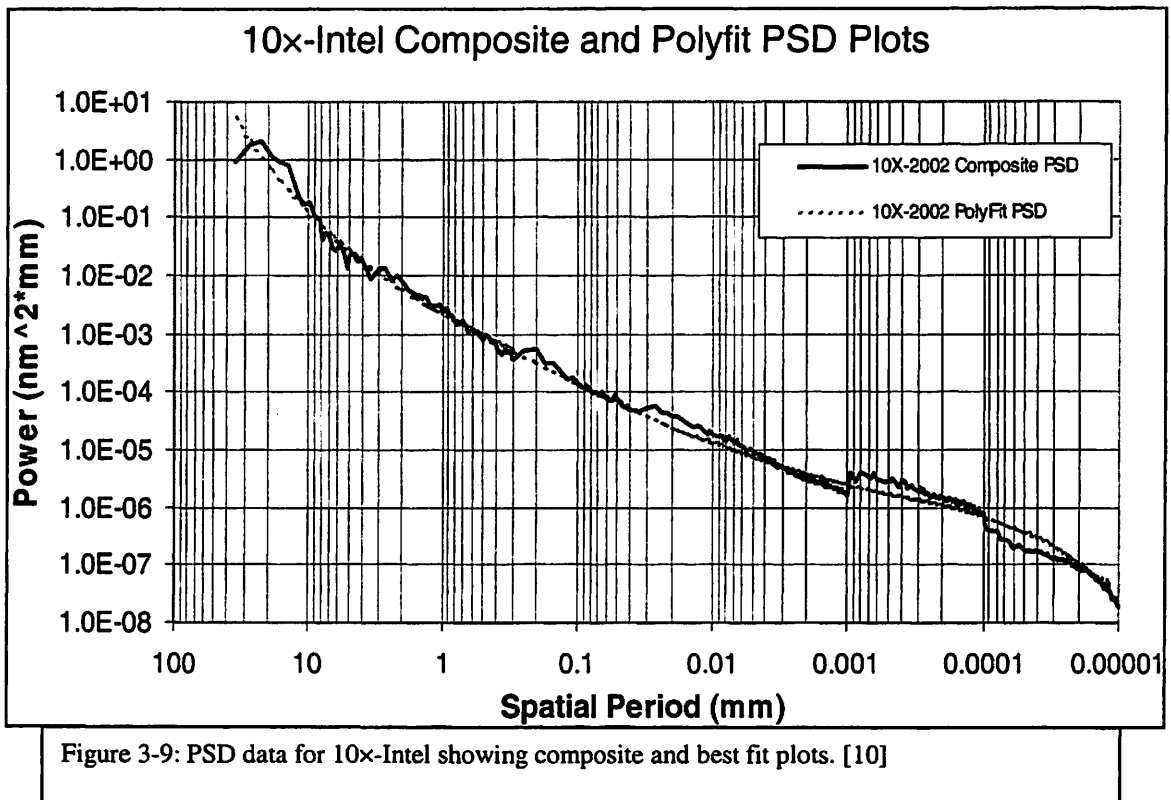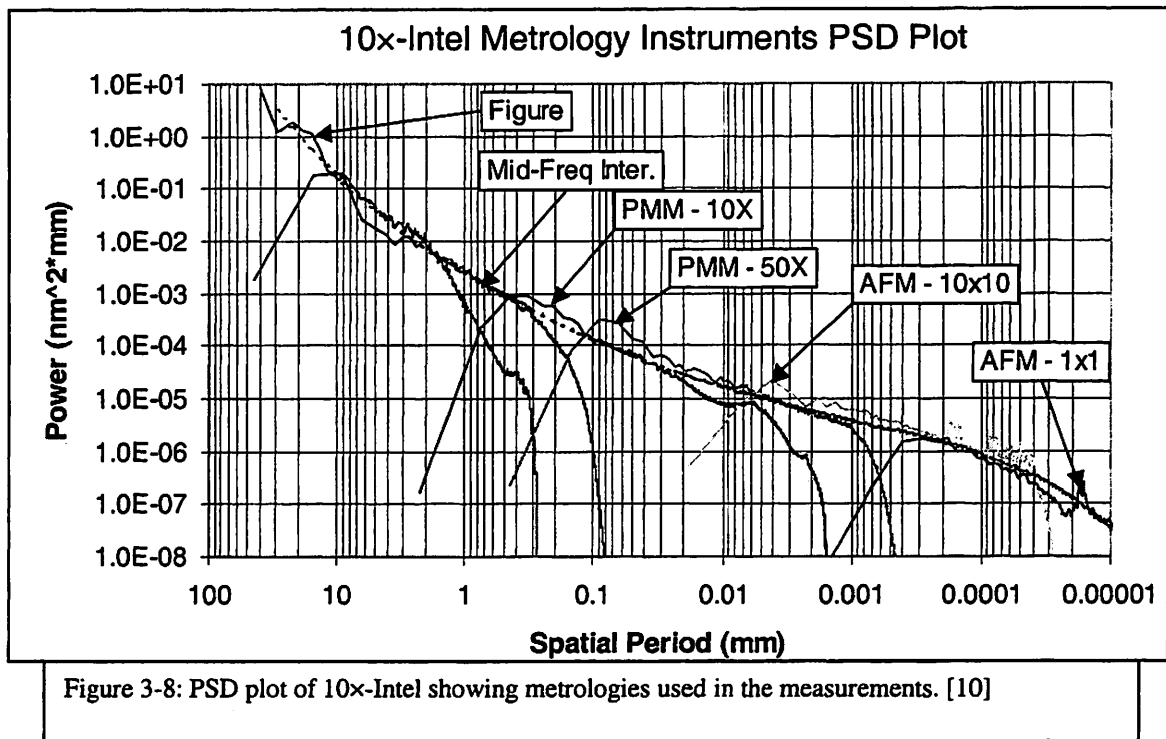
Two primary mirrors and two secondary mirrors were polished to within the above specifications by Tinsley Corporation for the 10x-Intel optic. Based on polishing data and interferograms of the surfaces, a primary and a secondary mirror were chosen for coating. The multilayer coating and 0.08-NA visible-light interferometry was done at Sandia and Lawrence Livermore National Labs. When the optic was ready to be assembled, each mirror's rotational position needed to be determined. These calculations are detailed in the next section.

3.2.2 Clocking The Mirrors

Once the new substrates were multilayer coated, the two mirror's orientations with respect to one another needed to be determined. See Figure 3-10 for a conceptual diagram of clocking this two-mirror system. The best performance of this optic in 0.8-NA apertures around the optic was calculated through an iterative procedure using Code V [14]. Code V is an optical design software package with optimization and analysis routines. The optics were clocked using 10° steps. First, the primary mirror was kept fixed and the secondary mirror was rotated around in 10° steps and wavefront error was measured. Then the primary mirror was rotated 10° and the secondary went all the way around again. When low wavefront areas were discovered, simulations were redone in those areas with 5° resolution. Ultimately, over 1,500 wavefronts were calculated.

Figure 3-10: Clocking a 10× optic by rotating both the primary and secondary mirrors around the optical axis to find the best wavefront.
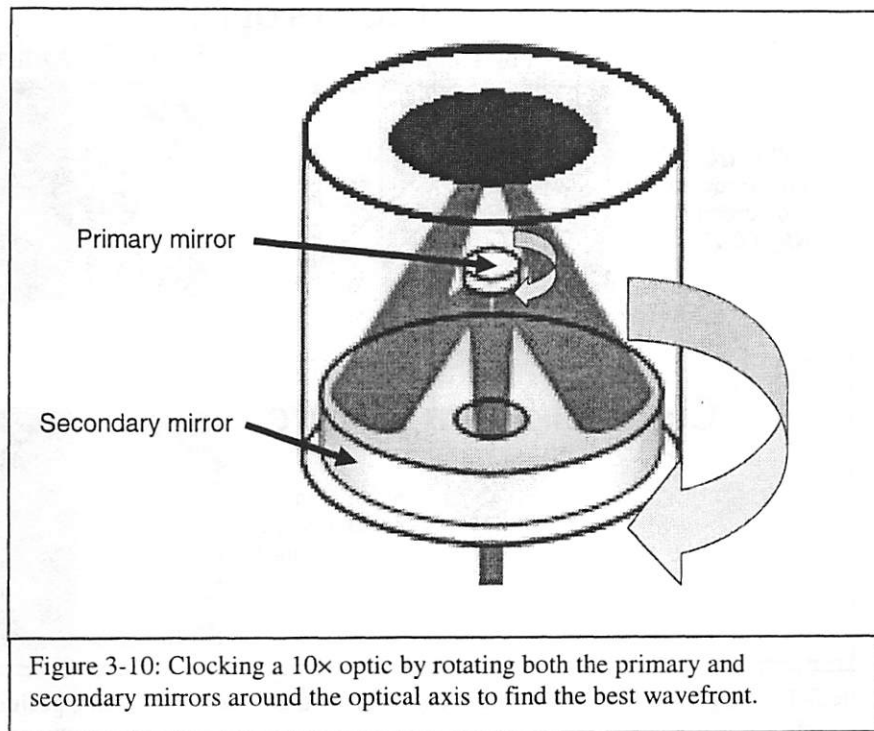
Figure 3-11 shows the full primary and secondary interferograms used in the Code V clocking simulations. The smallest wavefront error is achieved when the circled areas are combined. That wavefront is shown at the bottom of the figure in its corresponding 0.08 NA sub-aperture.
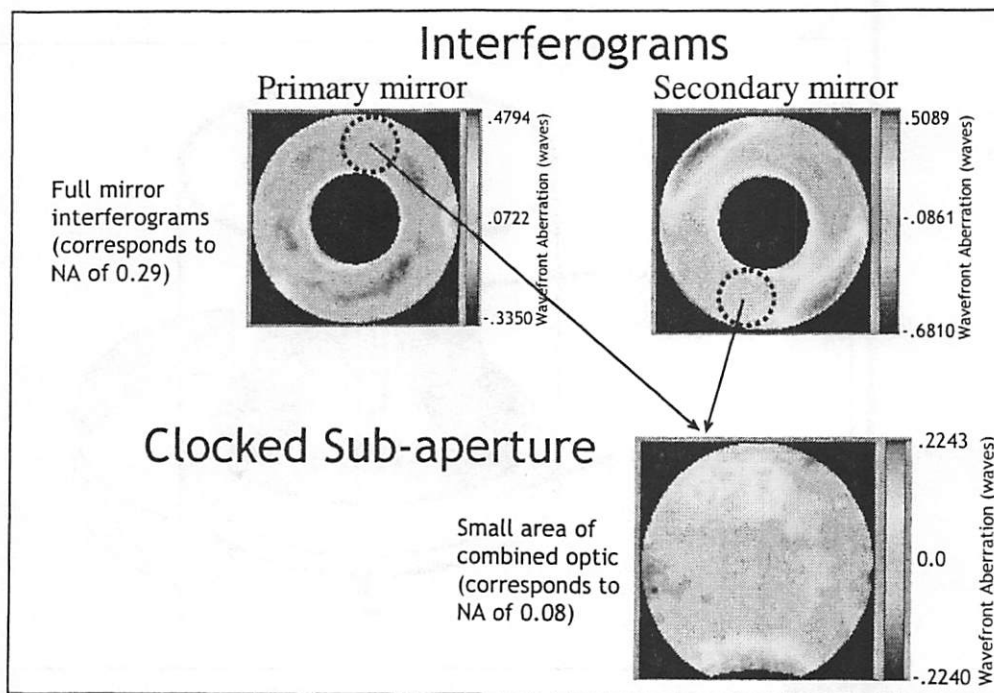
Figure 3-11: Primary and secondary mirror interferograms. The best clocking positions are denoted with circles and combined to show the wavefront error in the smaller sub-aperture.

Figure 3-12 shows the clocked sub-aperture from Figure 3-11 denoted as the 0° field alongside the wavefront from the other side of the optic.
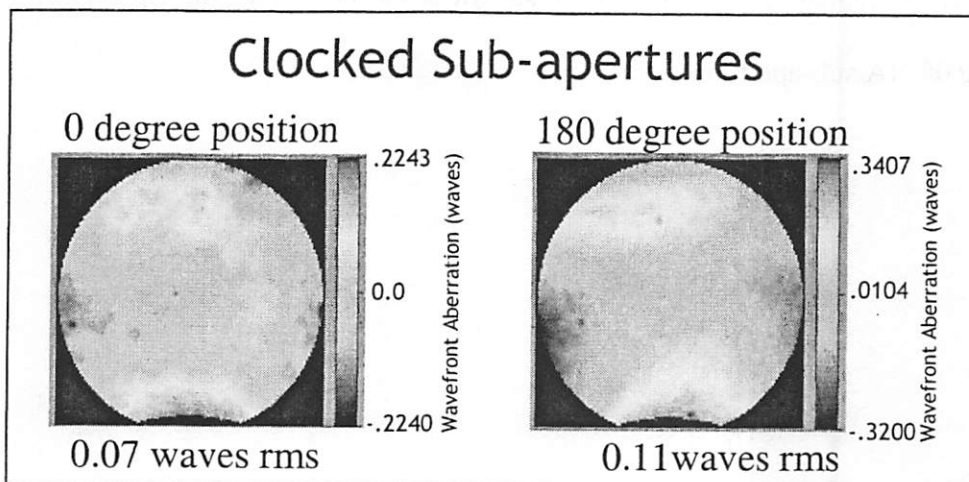
Figure 3-12: Clocked sub-apertures of the 10×-Intel optic and corresponding wavefront errors.

3.2.3 Interferometry

Visible light interferometry was done next on 10x-Intel at Lawrence Livermore National Laboratory. Their lensless interferometry approach indicated 0.36-nm rms wavefront error for the first 36 Zernikes. For spatial frequencies up to 30 mm^{-1} there was a 0.49 nm rms error. These values are for a 0.07 NA sub-aperture. Details for the first 37 Zernike polynomials (including coma, astigmatism, and trefoil) are displayed in Appendix A. The Zernike polynomials are a set of orthogonal functions over a unit circle. The lowest 37 polynomials are used to describe the low-spatial frequency aberrations of interest in the 10x system.

After the visible light interferometry and alignment measurements were finished, EUV interferometry using the PS/PDI technique developed at Lawerence Berkeley National Laboratory (LBL) was done [4]. With the assistance of Ken Goldberg from LBL, the analysis was done on the 0° sub-aperture of the 10x-Intel optic. It turned out that astigmatism was the main culprit in the wavefront error. After four alignment iterations consisting of slight positioning corrections of the primary mirror the astigmatism was reduced almost to zero. This was done using the primary mirror's tilt adjustments. In the housing, the secondary mirror (larger mirror) is held in place but the smaller, primary mirror is attached to two locking arms which allow it movement to help remove aberrations in the wavefront.

The EUV and visible-light wavefront measurements are shown in Fig 3-13. The EUV measurement domain covers nearly the entire 0.088 NA sub-aperture. The outer edge of the primary mirror clips the beam on the side closest to the Schwarzschild

objective's axis of rotation (the bite out of the circle). The visible-light measurements are restricted to 0.07 NA.
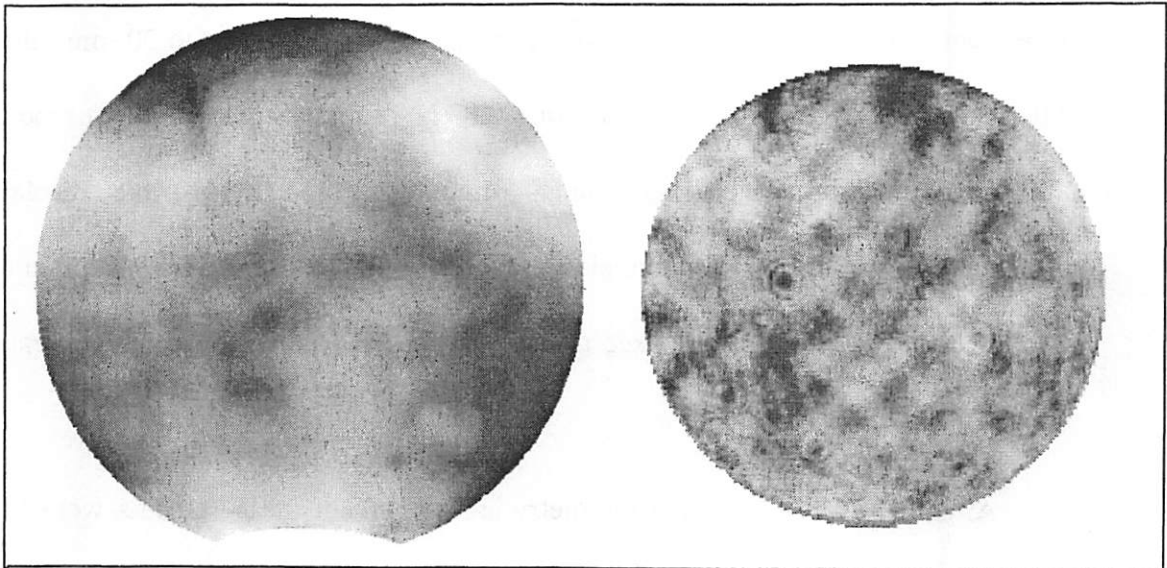
Figure 3-13: EUV (left) and visible-light (right) wavefront measurements. As shown, the EUV data covers 0.0876 NA while the visible-light data covers 0.07 NA. The wavefront phasemaps are shown on the same range: [−3.420, 1.975] nm. Between the two wavefronts, there is an 8° rotation in the raw data related to the orientation of the CCD and the optic during testing. Piston, tilt and defocus have been removed from both wavefronts.

Figure 3-14 compares the wavefronts from both the visible and EUV measurements when restricted to the 0.07 NA. An 8° rotation is applied to the visible-light Zernike coefficients to bring the two measurements into agreement.
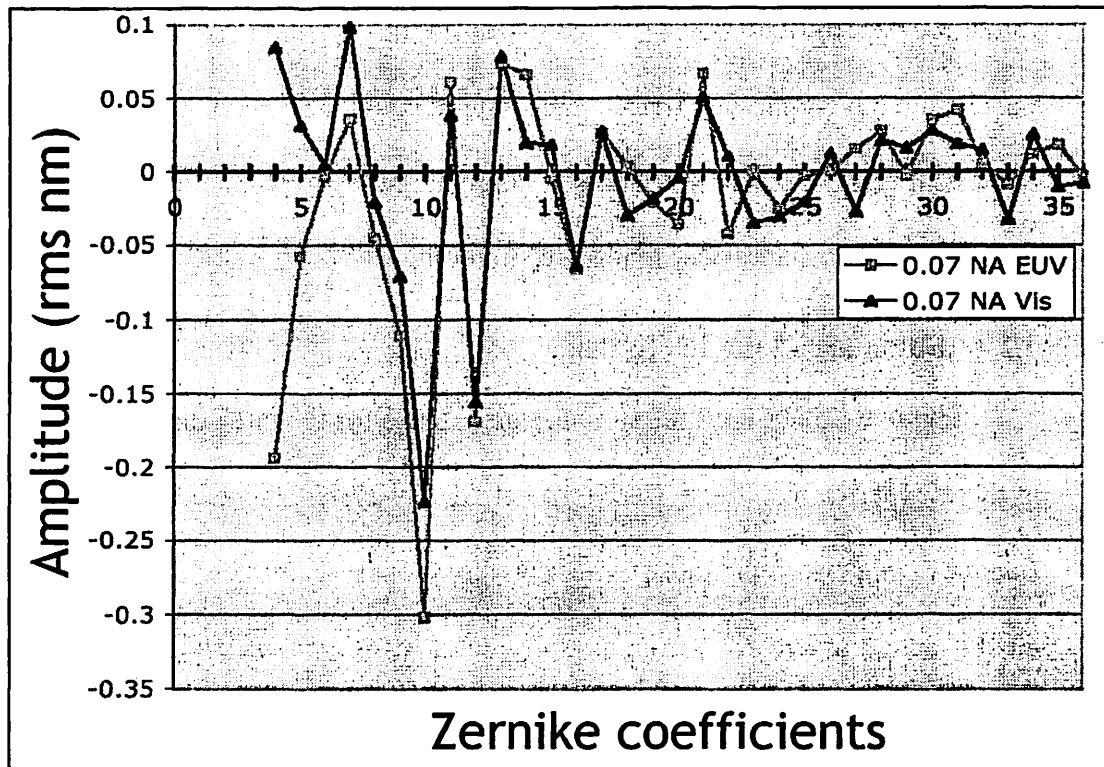
Figure 3-14: Zernike coefficient comparison beween EUV and visible interferometries for 10x-Intel.

Appendix A contains a detailed list of the Zernikes for EUV at 0.876 NA and EUV and visible for 0.07 NA.

The overall wavefront measured for the larger NA at EUV was 0.74 nm rms. This is comparable if not a little higher than the 10x-B2 optic (0.67 nm rms). Also, a through-wavelength scan was done to look at the multilayer response. There was no ringing during the sweep which suggests that the multilayers were laid down very well. After interferometry measurements were complete the interferometry chamber was replaced and the system was switched over to the imaging configuration.

Figure 3-14 also shows that trefoil is the largest single contributor in the wavefront error (Zernike coefficient number 10). If all of the astigmatism in the system were

57

removed, the 10×-Intel could reach a wavefront of 0.69 nm rms (.088 NA). However, by mathematically removing trefoil, the system could achieve 0.48 nm rms (.088 NA) wavefront error. Unfortunately, this is not an alignment variable as is astigmatism, but it does highlight the large contribution from trefoil.

3.2.4 Summary of the 10× Systems

Figure 3-15 shows three sub-aperture images for the three different 10× optics used in these experiments. These were taken at EUV wavelengths using a CCD camera. 10×-Berkeley clearly had the most defects on the multilayer mirrors. Care was taken to steer the diffraction orders away from the spots but it was never entirely possible.

| 10×-Berkeley | 10×-B2 | 10×-Intel |
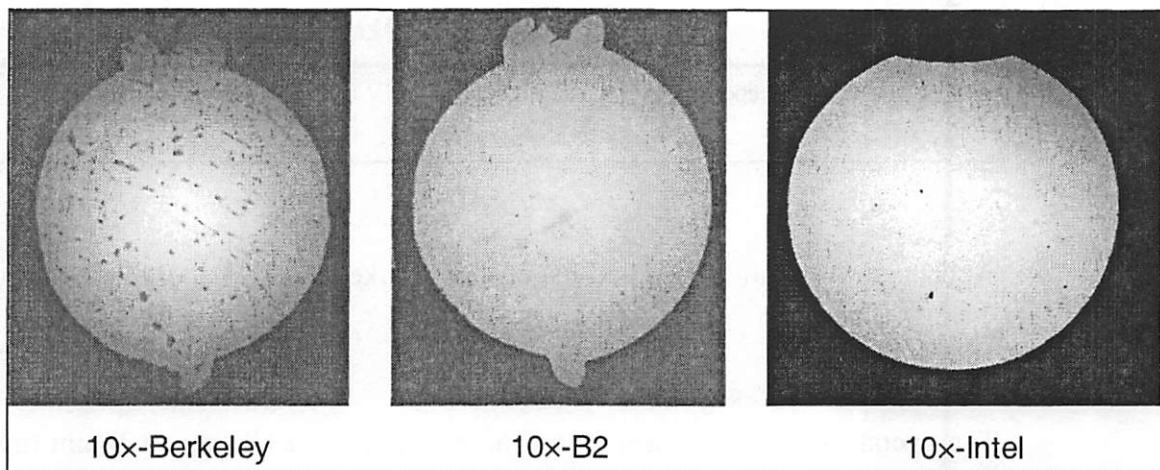
Figure 3-15: CCD images of the pupil plane for three different 10× optics.

The two most recent optics, 10×-B2 and then 10×-Intel, are the most similar. The main comparison should be made between these two optics. Figure 3-16 shows magnified images of the 10×-B2 surface.
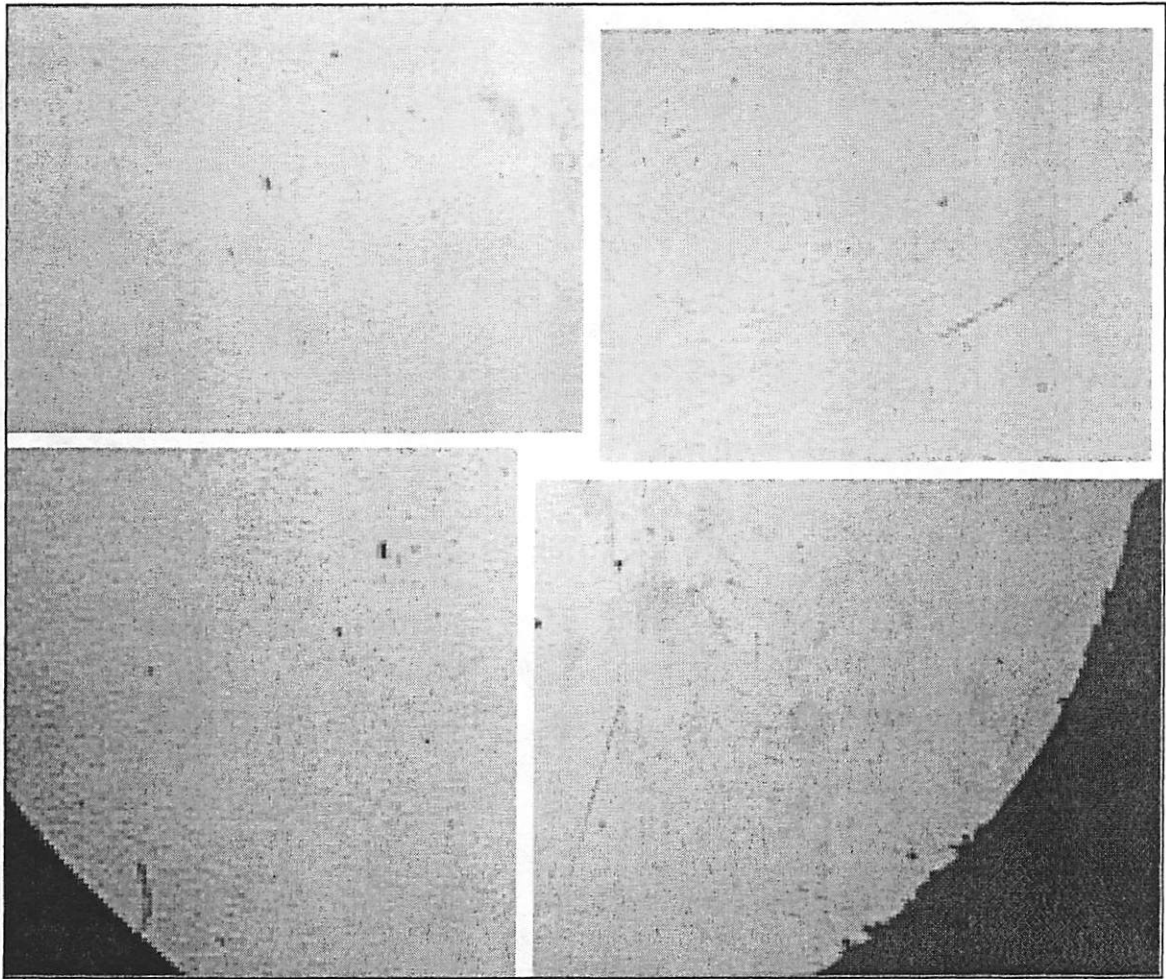
Figure 3-16: Magnified images of 10×-B2 showing optic surface at EUV wavelengths.

Figure 3-17 shows magnified images of the 10×-Intel surface.
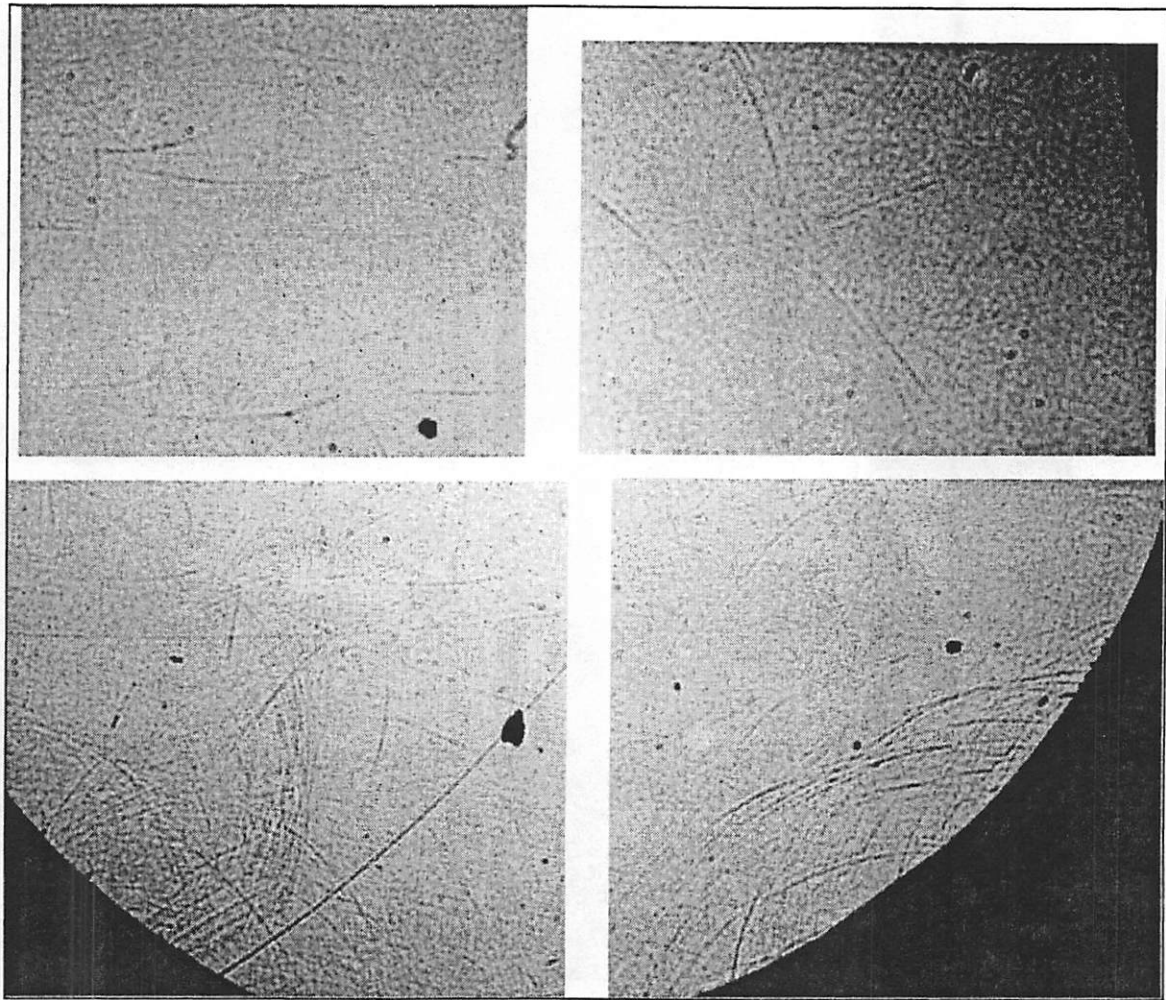
Figure 3-17: Magnified images of 10×-Intel showing optic surface at EUV wavelengths.

It is evident that there is a higher density of repetitive scratches in the new 10×-Intel optic. As mentioned above, these images do not mean that any specifications were misquoted or were not reached. But rather, it appears that a polishing technique was used that created a new roughness pattern that had not been seen before. A simulation on the effects of these scratches is shown in Section 5.6.

3.3   Micro Exposure Tool (MET)

One of the newest EUV imaging systems in the world, the Micro Exposure Tool (MET), was used in the aerial imaging contrast experiments. It has a larger NA (0.3) than any other current EUV tool and is designed to print down to the 32nm node but should be able to go even farther when printing in monopole and dipole modes. It is a 5× reduction system and uses two mirrors. The field size is 0.2×0.6 mm^2.

Wavefront error was measured at-wavelength by Ken Goldberg and Patrick Naulleau of Lawrence Berkeley National Laboratory and shown to be 0.8 nm rms in the first 37 Zernikes [11]. One great advantage to this tool, which is also attached to the highly coherent ALS, is that it has a set of rotating mirrors which can program any desired pupil fill into the system. Therefore, coherence can range from 0.1 to 1 and all manner of illuminations (annular, monopole, dipole, quadrupole) are possible.

3.4   Conclusions

The EUV 10× Schwarzschild optic design has gone through four generations. It started with the 10×-Berkeley, went through the 10×-A and 10×-B series, and ended with the 10×-Intel. Each subsequent generation has had improvements in the polished substrates and in better multilayer depositions.

This chapter discussed the procedure to create the specifications for the 10×-Intel optic system. This included roughness simulations and specification negotiations. After the mirrors were made, work was done on clocking the mirrors and measuring the assembled optic's performance at EUV wavelengths.

One of the biggest hurdles in this research was working to overcome exposure field nonuniformities. A huge improvement was made with the 10x-Intel optic since full field images were achieved (as will be shown in Chapter 5). More improvements could have been possible with even better polished optics or a reduction in certain polishing scratches that will be discussed in Section 5.6.

3.5 References

[1] G. Kubiak, D. Tichenor, M. Malinowski, R. Stulen, S. Haney, K. Berger, L. Brown, J. Bjorkholm, R. Freeman, W. Mansfield, D. Tennant, O. Wood II, J. Bokor, T. Jewell, D. White, et al., "Diffraction-limited soft x-ray projection lithography with a laser plasma source," J. Vac. Sci. Technology B, Vol. 9, No. 6, 3184-3188 (1991).

[2] P. Naulleau, K. Goldberg, E. Anderson, K. Bradley, R. Delano, P. Denham, B. Gunion, B. Harteneck, B. Hoef, H. Huang, K. Jackson, G. Jones, D. Kemp, J. Liddle, R. Oort, A. Rawlins, S. Rekawa, F. Salmassi, R. Tackaberry, C. Chung, L. Hale, D. Phillion, G. Sommargren, J. Taylor, "Status of EUV micro-exposure capabilities at the ALS using the 0.3-NA MET optic," Proc. SPIE, Vol.5374, No.1, 881-891 (2004).

[3] W. Ballard, D. Tichenor, D. O'Connell, L. Bernardez II, R. Lafon, R. Anderson, A. Leung, K. Williams, S. Haney, Y. Perras, K. Jefferson, T. Porter, D. Knight, P. Barr, J. Van de Vreugde, R. Campiotti, M. Zimmerman, T. Johnson, L. Klebanoff, P. Grunow, S. Graham Jr., D. Buchenauer, W. Replogle, T. Smith, J. Wronosky, J. Darnold, K. Blaedel, H. Chapman, J. Taylor, L. Hale, G. Sommargren, E.

Gullikson, P. Naulleau, K. Goldberg, S. Lee, H. Shields, R. St. Pierre, and S. Ponti, "System and process learning in a full-field, high-power EUVL alpha tool," Proc. SPIE, Vol.5037, 47-57 (2003).

[4] H. Medecki, E. Tejnil, K. Goldberg, and J. Bokor, "Phase-shifting point diffraction interferometer," Optics Letters, Vol. 21, No. 19, 1526-1528 (1996).

[5] J. Goldsmith, K. Berger, D. Bozman, G. Cardinale, D. Folk, C. Henderson, D. O'Connell, A Ray-Chaudhuri, K. Stewart, D. Tchenor, H. Chapman, R. Gaughan, R. Hudyma, C. Montcalm, E. Spiller, J. Taylor, J. Williams, K. Goldberg, E. Gullikson, P. Naulleau, and J. Cobb, "Sub-100-nm imaging with the EUV 10x Microstepper," Proc. SPIE, Vol. 3676, 264-271 (1999).

[6] J. Cobb, P. Dentinger, L. Hunter, D. O'Connell, G. Gallatin, W. Hinsberg, F. Houle, M. Sanchez, W. Domke, S. Wurm, U. Okoroanyanwu, and S. Lee, "EUV photoresist performance results from the VNL and the EUV LLC," Proc. SPIE, Vol. 4688, 412 (2002).

[7] E. Gullikson, S. Baker, J. Bjorkholm, J. Bokor, K. Goldberg, J. Goldsmith, C. Montcalm, P. Naulleau, E. Spiller, D. Stearns, J. Taylor, and J. Underwood, "Scattering and flare of 10x projection cameras for EUV lithography," Proc. SPIE, Vol. 3676, 717 (1999).

[8] Eric Gullikson data file, Lawrence Livermore National Laboratory

[9] J. Elson and J. Bennett, "Calculation of the power spectral density from surface profile data," Applied Optics, Vol. 34, No. 1, 201-208 (January 1995).

[10] ASML/Tinsley data for 10×-Intel

[11] K. Goldberg, P. Naulleau, P. Denham, S. Rekawa, K. Jackson, J. Liddle, and E. Anderson, "EUV interferometric testing and alignment of the 0.3-NA MET optic," Proc. SPIE, Vol. 5374, 64-73 (May 2004).

[12] H. Meiling, V. Banine, P. Kuerz, and N. Harned, "Progress in the ASML EUV program," Proc. SPIE, Vol. 5374, 31-42 (May 2004).

[13] T. Oshino, S. Takahashi, T. Yamamoto, T. Miyoshi, M. Shiraishi, T. Komiya, N. Kandaka, H. Kondo, K. Mashima, K. Nomura, K. Murakami, H. Oizumi, I. Nishiyama, and S. Okazaki, "Fabrication of aspherical mirrors for EUV projection optics set-3 of HiNA," Proc. SPIE, Vol. 5533, 10-19 (October 2004).

[14] Code V, Optical Research Associates, 3280 E. Foothill Blvd., Pasadena CA 91107; www.opticalres.com.

4   Experimental Systems

4.1   Introduction

The EUV imaging tools developed to do this research have taken advantage of the Advanced Light Source (ALS) at Lawrence Berkeley National Laboratory. This undulator synchrotron provides a path to achieving coherence at short wavelengths, including EUV's 13.4 nm lithography point [1]. This chapter introduces the hardware and control systems that were built in order to run the F2X experiments.

4.2   Design

It was discussed in Chapter 2 how the spatial frequency doubling technique requires the use of a special pupil-plane aperture stop and spatially coherent illumination. The full experimental configuration is shown in Figure 4-1.
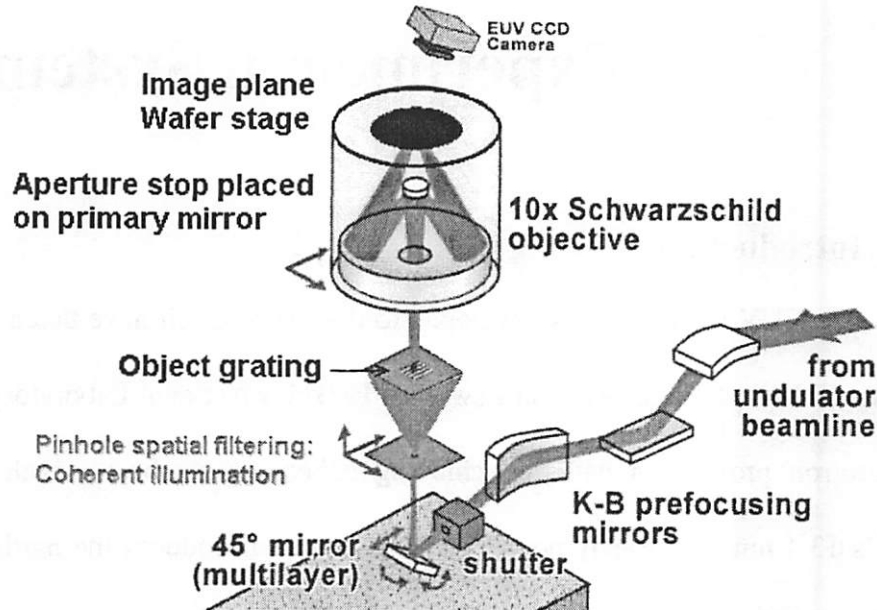
Figure 4-1: F2X Experimental Setup at Beamline 12.0.1 (ALS)

Spatially coherent, monochromatic EUV radiation was provided by an undulator beamline (beamline 12.0.1 at the ALS). The optical configuration was based on several reversible modifications made to the phase-shifting/point-diffraction interferometer (PS/PDI) station operated on this beamline [2]. The light path, containing a grating monochromator followed by a Kirkpatrick-Baez mirror pair (K-B), delivered radiation from the undulator to the imaging station.

The undulator beamline provides continuously tunable illumination from 5-nm to 25-nm wavelengths with spectral resolving power as high as $\lambda/\Delta\lambda \sim 1000$. A flat, multilayer-coated turning mirror was mounted at an angle of incidence near 45° to direct the beam vertically. Near the focal plane of the K-B pair, a spatial filter pinhole,

originally 2 μm in diameter, provided uniform and coherent illumination of the transmission object which sat 1.08 cm above the pinhole.

A 40 × 40 μm square transmission grating was used as the object, and was mounted on a 3-axis translation stage. More information on the object masks is provided in Section 4.3. The 10×-Schwarzschild optical system, described in Section 3.2, was used as the imaging optic. A specially designed aperture stop was mounted in the entrance pupil of the system. Figure 4-2 shows the aperture stop used in the experiment.
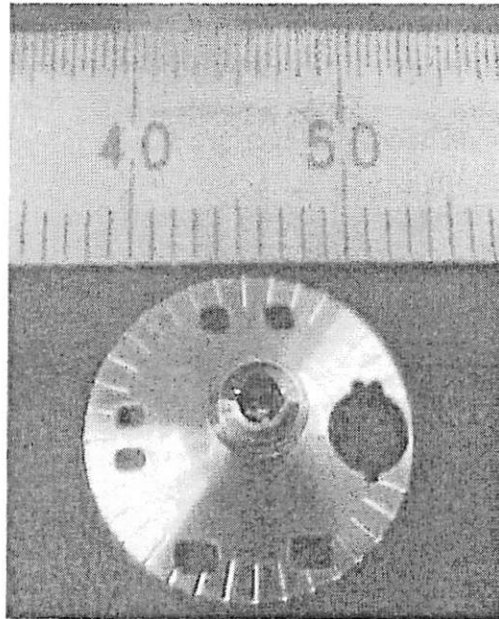
Figure 4-2: Aperture stop which sits against the primary mirror

Three aperture pairs are shown with different separations that are designed to print 70-100 nm, 40-50 nm, and 20-30 nm dense lines. For each grating object, the appropriate aperture stop was selected. The 4-mm 'circular' aperture on the right side was used to align the object illumination and is asymmetric to help determine aperture orientation when viewing the pupil from a CCD camera. A wafer translation stage is located at the

image plane of the optical system and enabled multiple fields be exposed on each 4-inch wafer.

Beam alignment was performed using an EUV-sensitive CCD camera that was placed on top of the imaging system and used when there was not a wafer in the image plane. The Schwarzschild objective projected an enlarged image of the entrance pupil onto the 1-inch-square CCD, and allowed adjustments to be made in real time. Figure 4-3(a) shows the projected pupil illumination pattern from a 2.8-μm pitch grating with the zeroth, +1, and −1 orders present. Figure 4-3(b) has the central, zeroth-order light blocked by the aperture stop. The +1 and −1 orders have been directed through the optic. The dotted rings mark the position of the aperture pair.
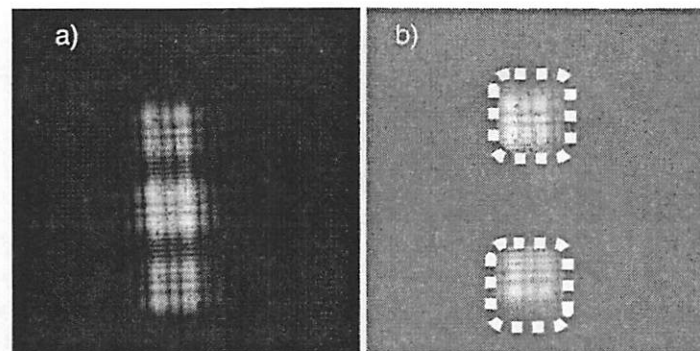
Figure 4-3: CCD camera images a) without aperture stop, b) with aperture stop blocking the zeroth order. The aperture openings are marked in the picture by white dashes.

4.2.1 Experiment Apparatus

The spatial frequency doubling (F2X) imaging station was housed in a vacuum chamber that consisted of three main parts: the object housing, the optic chamber, and the load-lock assembly. Figure 4-4 shows a diagram of the major parts of the imaging system.
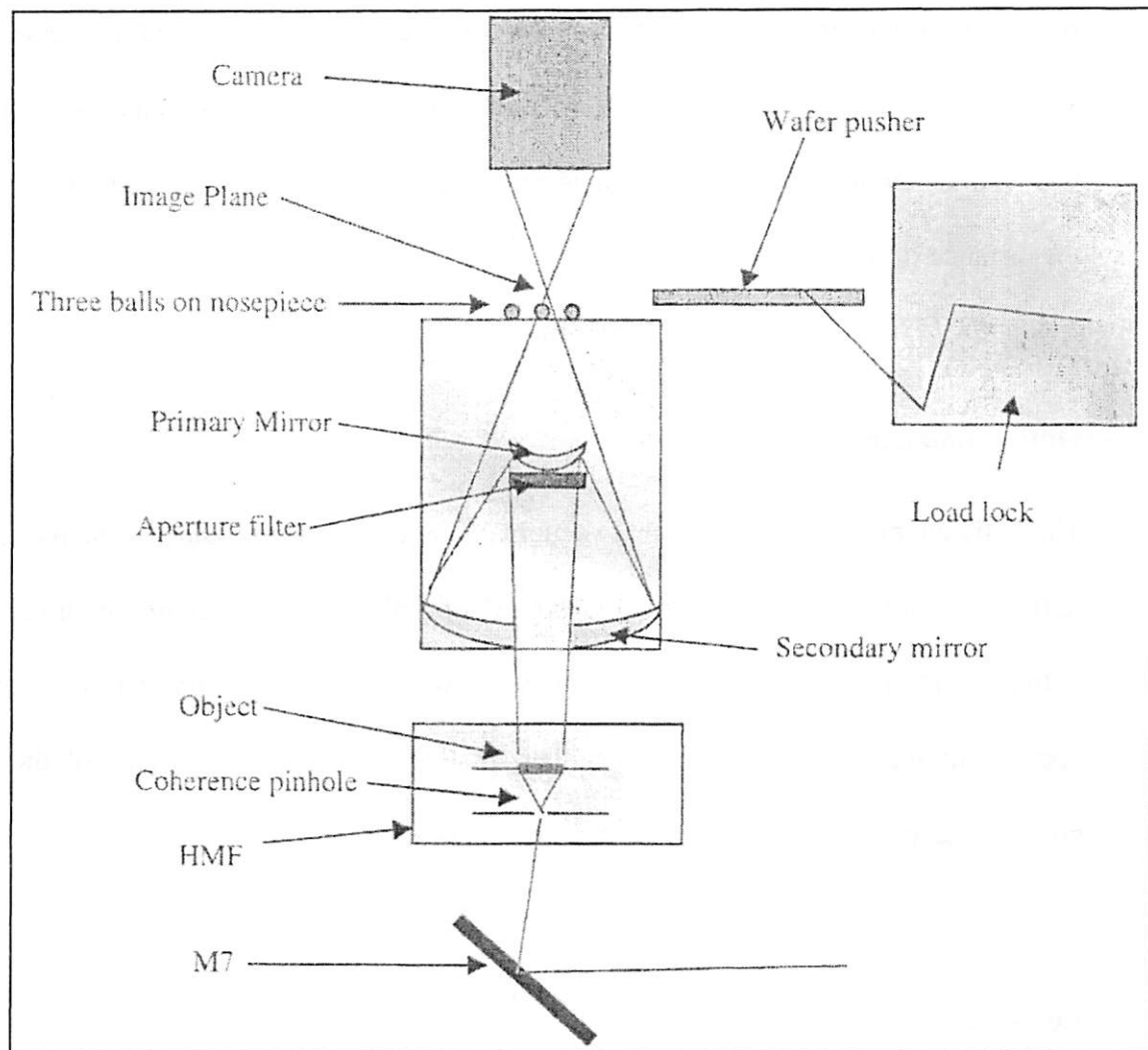
Figure 4-4: Diagram of the F2X system.

Object Housing:

The object housing (labeled HMF in Figure 4-4) was a structure, situated before the optic chamber, used primarily as a mount for the pinhole and object grating. It was translatable in the X, Y, and Z axes, independent from the optic chamber. As mentioned above, near the focal plane of the K-B pair, a illumination pinhole was used as a spatial filter before the EUV photons illuminated the object. The X-Y controls were used to position the housing such that the incoming light was centered directly onto the pinhole. When this

was out of alignment, imaging performance would degrade as simulated in Section 2.3.5. The object grating was mounted 10.795 mm above the pinhole. A transmission grating was used as an object mask. The Z-axis provided focus control in the system by altering the distance of the object from the optic.

Optic Chamber

The optic chamber was a cylindrical vacuum chamber that housed the 10× Schwarzschild optic. The aperture stop was mounted in the pupil plane of the system which coincided with the primary mirror. Above the image plane was the EUV-sensitive CCD camera. An opening in the side of the optic chamber, in line with the image plane of the optic, provided access for the wafers by way of the load-lock.

Load-lock:

The load-lock arm doubled as the wafer translation stage. It was level with the image plane of the optical system, defined by three ball bearings built into the 10× housing. The load-lock is a small, rectangular vacuum chamber equipped with an extendable arm and U-shaped wafer holder. A computer controlled motor translated the arm and wafer in and out of the optic chamber. Once the wafer reached the ball bearings, the wafer would ride up onto them and no longer be sitting in the wafer holder. A rise on the wafer holder would push the wafer along a line for the exposure series. The load-lock vastly increased the throughput for the F2X system by reducing the amount of time it took to load, expose, and remove each wafer. Only a small portion of the system needed to be exposed to air,

significantly reducing pump-down time. This also allowed for enhanced alignment repeatability of the system between wafers. Previously, after alignment of the system, vacuum had to be broken and the chamber lid replaced with a translator device.

4.2.2 Wafer Handling/Resist Processing

Preparation:

The F2X system was equipped to handle 4 inch wafers. Initial wafer preparations were done at the UC Berkeley Microlab, where Hexamethyldisilazane (HMDS) was applied using a prime oven for 10-60 seconds. HMDS was used to help photoresist adhesion to the silicon/silicon dioxide wafer. The wafers were then individually packaged and brought to the synchrotron and placed in a small cleanroom. When ready for exposures, a wafer was prepared by spinning on a test resist and performing a post application bake (PAB). The spin-on speed was determined empirically by measuring resist thickness using a profilometer and chosen so that there was approximately a 2.5:1 ratio of resist thickness to desired linewidth. PAB was performed according to the resist manufacturers' instructions. The resist-coated wafer was then repackaged in a container and covered in aluminum foil to block resist exposure to room lights. At the imaging station, the wafer was removed from its packaging and placed onto the load-lock arm. The load-lock chamber was then pumped down and the wafer was inserted into the optic chamber for exposure.

71

Exposure:

As the wafer was brought into the chamber it was placed on the three ball bearings which defined the image plane. The wafer was then decoupled from the load lock arm, except when pushed to the next exposure spot. Dose control was accomplished by undulator tuning and altering the length of time a beamline shutter was open to admit light. The dose parameters were given to a computer program that controlled the exposure run. The program automatically opened and closed the shutter for each exposure and then translated the wafer forward. Typical operations separated the exposed 4-μm fields by 50 μm. Light intensity was monitored manually during the exposure run and adjusted as needed to maintain dose parameters. Before there was a load lock, the wafer translation was done by hand using a mechanical feedthrough.

Development:

After exposing, the wafer was removed from the load-lock, placed in a container and wrapped in aluminum foil. It was then brought back to the cleanroom where the post exposure bake (PEB) and development were performed. Delay time between removal from the load-lock and PEB start was approximately 30 seconds.

4.3 Object Masks

Three sets of object masks were fabricated for these experiments. The first two were transmission masks used in the 10× Schwarzschild system and the last was a

multilayer reflection mask used in the MET for the aerial image contrast experiment (discussed in 6.3.1).

The transmission masks for the 10× Schwarzschild F2X experiments needed to be sized according to the overall 20× demagnification from the mask. For example, a 2-μm-pitch object prints 50-nm lines and spaces at the image plane. The first mask set was fabricated in the UC Berkeley Microlab by Chang Cho. The masks were an open stencil design as shown in the scanning electron microscope (SEM) images of Figure 4-5. Nickel was layered over a silicon nitride (Si_3N_4) frame to create the absorber regions. The darker regions in the Figure are the open areas. The variations seen in these open areas are actually on the surface of the SEM stage. The pitch for this mask is 2 μm and the closed-to-open linewidth ratio is 1.22:1.
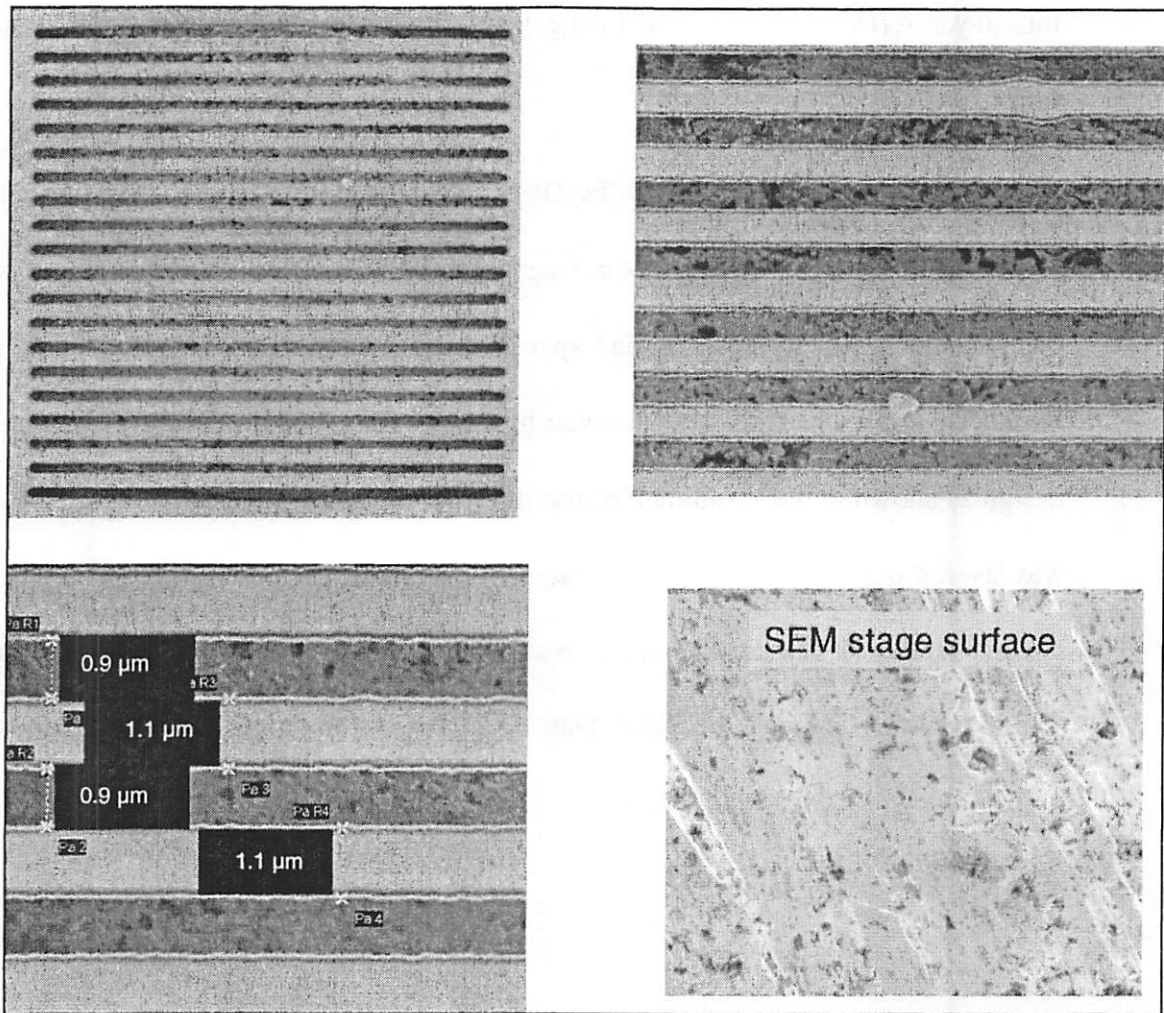
Figure 4-5: Three SEM pictures of an open stencil mask designed to print 50-nm dense lines and spaces at the wafer plane. The lower right picture shows the SEM stage at the same magnification. Since this is open stencil all the images show the stage below.

The second set of transmission masks were made at Lawrence Berkeley Lab's Nanowriter facility. They were also silicon nitride windows with nickel absorbers patterned on top. Rather than being open stencil, these masks had the silicon nitride layer covering the whole window. This makes for sturdier masks but the tradeoff is that there is some attenuation of the transmitted light through the silicon nitride. Single pitch and multiple pitch masks were made using the e-beam writer. For the multiple pitch masks, each pitch on the mask covered a quarter of a 40×40-µm square which produced a 2×2-

μm field on the wafer (the full image still being a 4×4-μm field). Simulations were done

on several different configurations for the multiple pitches before this design was chosen.

In the end, the four-square pattern on the far right was chosen because it did the best to

balance aperture shape conformity and line uniformity over each pitch. Figure 4-6 shows

a summary of these simulations.
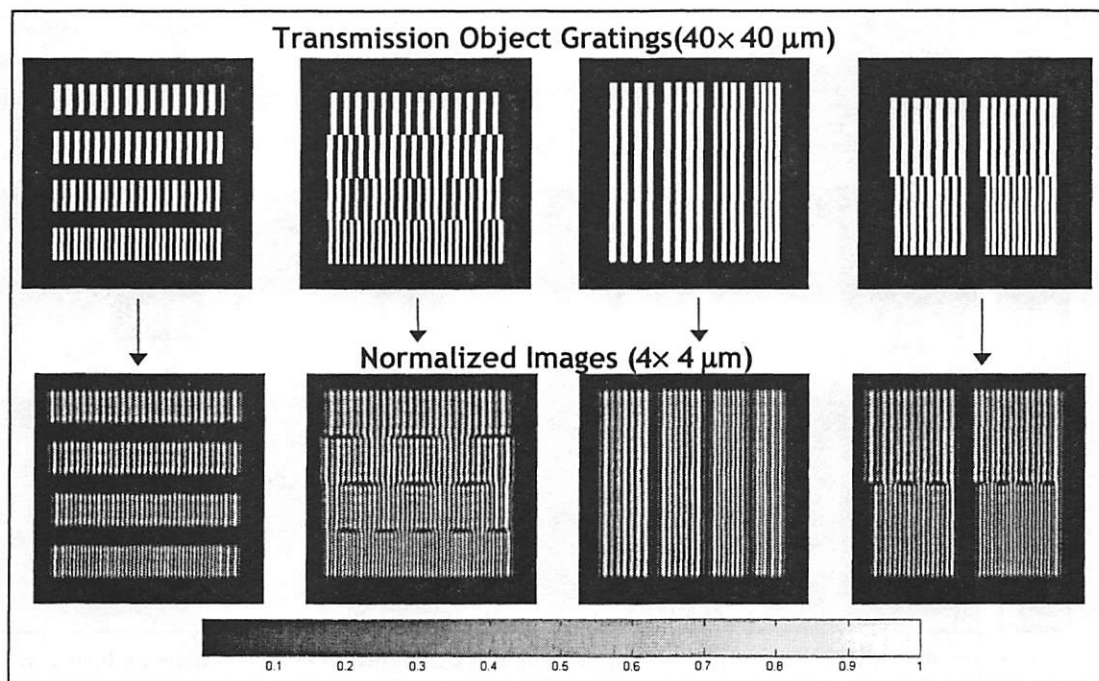
Figure 4-6: Simulations combining multiple-pitch gratings with the spatial doubling technique. Each layout prints 70, 60, 50, and 40 nm dense lines and spaces.

The e-beam written object masks were later imaged with a SEM. Figure 4-7 shows

a mask designed to print 40 nm features on the wafer (the pitch is just above 1.6 μm).

These masks used nickel as the absorber material. The grainy pattern in the transmitting

area (darker region) is normal from the Nanowriter mask process. On top of the silicon

nitride membrane in this transmitting region, there is 6 nm of chrome and then 12 nm of gold. These two layers attenuate the light by 55% [3].
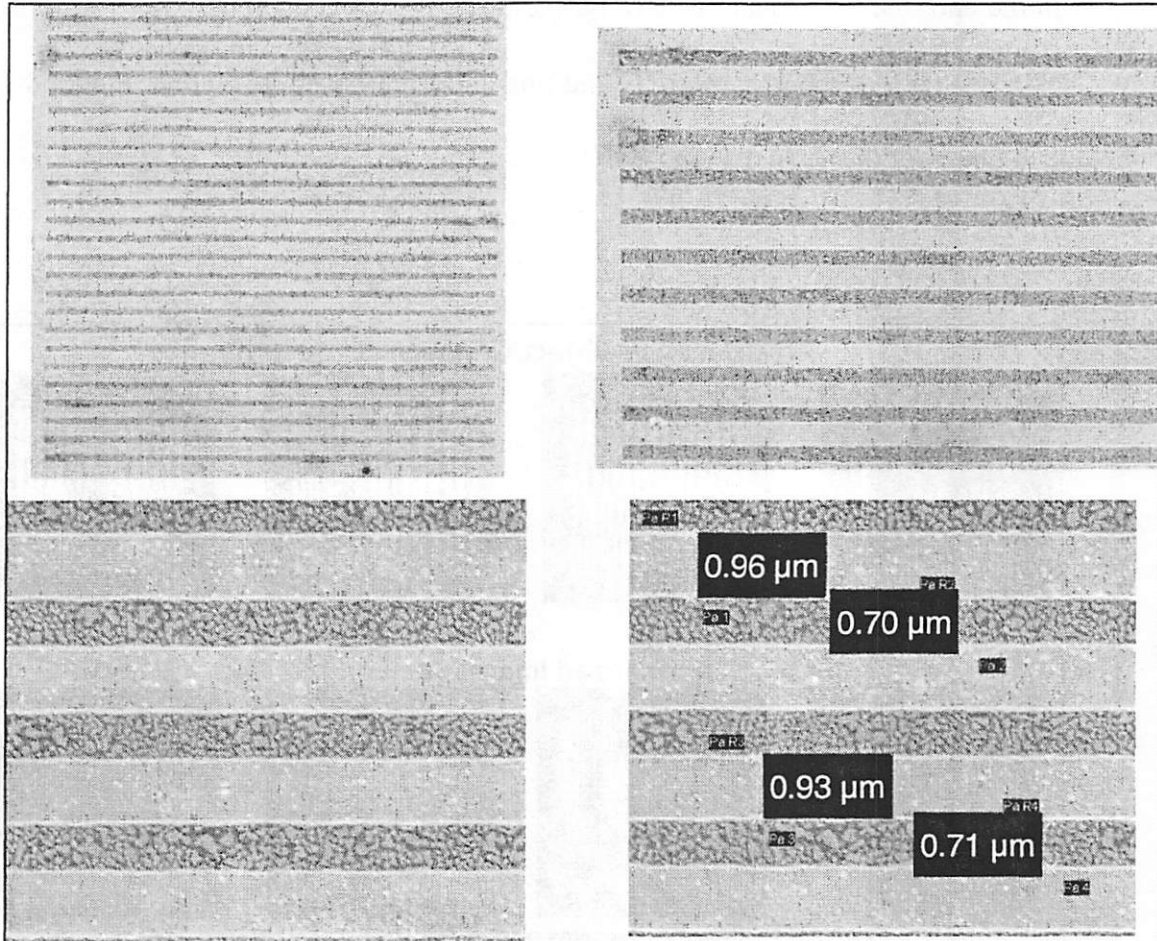
Figure 4-7: SEM pictures of an e-beam written mask designed to print 40-nm dense lines and spaces at the wafer plane. The darker area is the transmission region consisting of silicon nitride, chrome, and gold.

Figure 4-8 shows an example of a multi-pitch mask. This mask was programmed to print 70, 60, 50, and 40 nm features on the wafer. Its corresponding mask sizes are 1.4, 1.2, 1.0, and 0.8 μm. Once again, the chrome and gold on top of the silicon nitride can be seen magnified in the lower right corner.
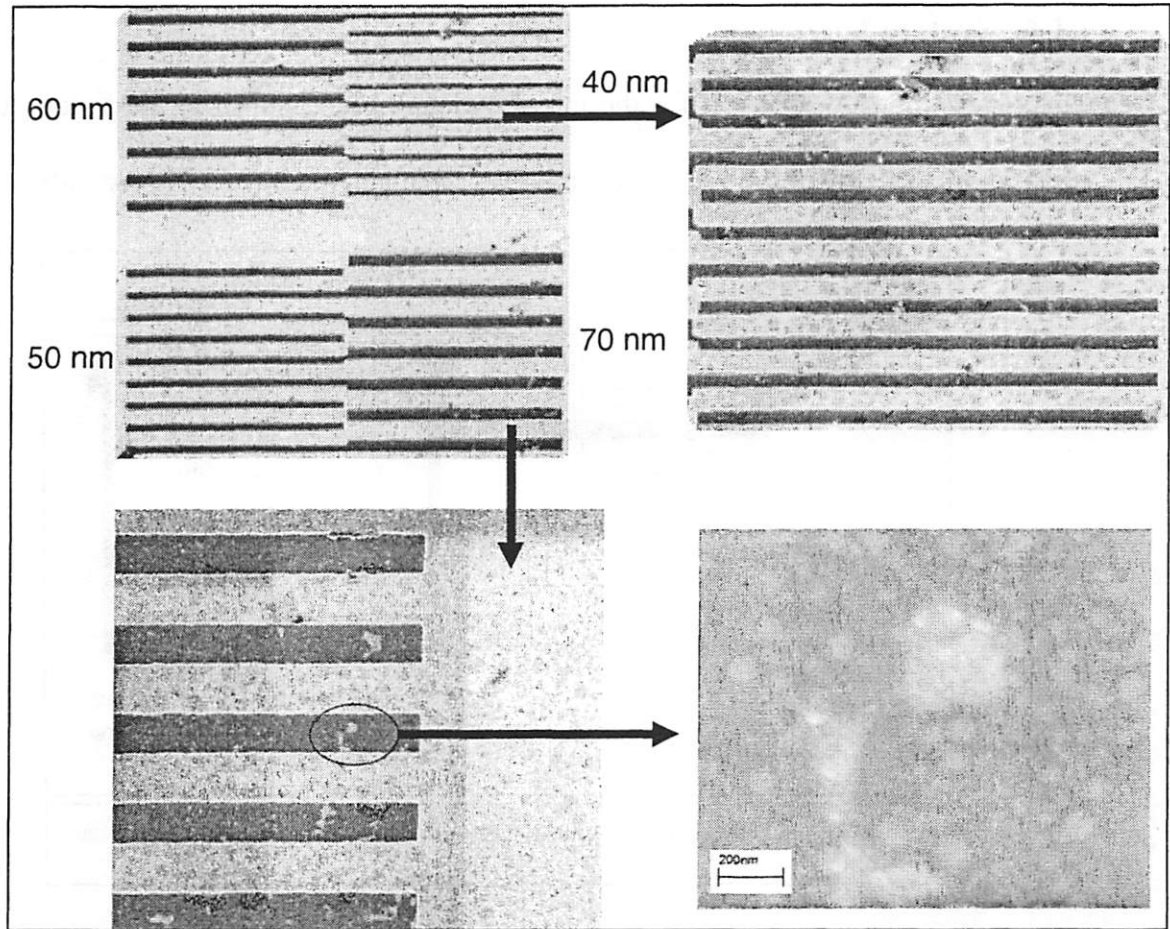
Figure 4-8: Multi-pitch masks written by e-beam tool. The upper left shows all four pitches and the sizes programmed for the wafer plane. The upper right is a zoomed in picture of the 40-nm features. The lower left is a zoomed in picture of the 70-nm lines. The lower right zooms in even more to show the transmission area.

It was found that these e-beam masks were also not quite equal line and space. For example, on the multiple pitch masks, the closed to open linewidth ratios were not 1:1 but ranged from 1:24:1 (1.4-μm lines) to 1.50:1 (0.8-μm lines). As my experiments will show, this still allows for patterns to be printed in photoresists. It will, however, degrade the light throughput somewhat.

4.4 System Upgrades

The first modification for the interferometry system consisted of adding a wafer translator to the top of the vacuum chamber. A schematic is shown in Figure 4-9.

Figure 4-9: Schematic of the wafer translator housing that was placed above the 10x optic.
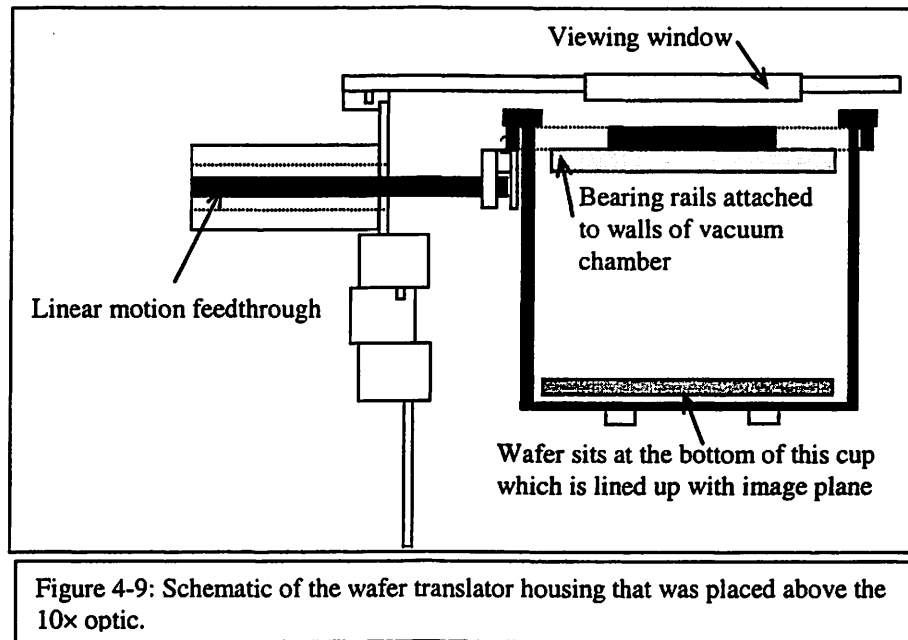
The cup, holding a wafer, would be lowered into a bearing-rail slider. Once the wafer was sitting on the 3-plane of the optic, the wafer would be pushed from the side by the cup. Pushing was done by way of a motion feedthrough. The first images were taken with this setup. The wafer was moved by hand. Dose control was through a simple computer program that would open the shutter once for an entered time.

Wafer exposures took a considerable amount of time. First, the system would be aligned using the CCD camera. The system would then be vented to air and the CCD would be replaced with this translator housing, all without trying to disturb the alignment. Then a wafer would be exposed several hundred times with manual translation between each exposure. Once the wafer was removed and processed, the CCD camera was

reattached in order to check alignment. These vacuum vent and pump steps took time and so wafer throughput was around 1-2 per eight-hour shift. But these exposures were not guaranteed to be aligned. Several upgrades improved this throughput and allowed alignment to be done immediately before exposing a wafer and without the need to vent the vacuum system.

Besides the e-beam-written grating masks mentioned in the previous section, there were other upgrades that allowed for better alignment and higher (~6×) throughput. This included switching from a 2.0 μm to a 0.5 μm pinhole before the mask. This pinhole is for spatial filtering and increases the coherence of the illumination. This smaller pinhole helped in producing more uniform illumination of the object grating. Simulations of this are shown in Section 2.3.4. Other modifications to the system included the previously noted wafer transfer load-lock, computer driven motors, and finer dose control. Further, as discussed in Chapter 3, a new optic using the 10×-Schwarzschild configuration was fabricated for use in the F2X system.

Original experiments were also done using a tabletop oven to do the post exposure bake (PEB). The upgrades incorporated a new hotplate which was housed in an amine-filtered clean room. This clean room also grew to house resist spinning, baking, and developing equipment. A new vacuum chamber was built to handle the load lock and allowed for significantly quicker pump down times by up to 50%.

Software was developed by Ken Goldberg of Lawrence Livermore National Laboratory to control the load-lock arm and shutter control, both of which previously had to be done manually. Focus and undulator control, however, were still manual.

4.5 Conclusions

The aim of this chapter was to lay out the design and procedures used for this research. The system has gone through some major modifications over the course of this project. The most significant being the new optic, load lock system, and clean room apparatus. Combined, these upgrades resulted in reliable and repeatable alignment and imaging performance. The throughput increase of 6× allowed for many more experiments as well as many more resists to be tested.

Many different object masks were used in these experiments. After successful printing with single pitch masks, an extension to multiple pitch masks was accomplished. The second set of masks had better fidelity since they were written by an e-beam tool, but line widths and spotted transmission regions degraded somewhat the ultimate performance of these masks (more on this in Chapter 5).

4.6 References

[1]   D. Attwood, P. Naulleau, K. Goldberg, E. Tejnil, C. Chang, R. Beguiristain, P. Batson, J. Bokor, E. Gullikson, M. Koike, H. Medecki, and J. Underwood, "Tunable coherent radiation in the soft x-ray and extreme ultraviolet spectral regions," IEEE Journal of Quantum Electronics, Vol. 35, No. 5, 709-720 (May 1999).

[2]   H. Medecki, E. Tejnil, K. Goldberg, and J. Bokor, "Phase-shifting point diffraction interferometer," Optics Letters, Vol. 21, No. 19, 1526-1528 (1996).

[3]   http://www.cxro.lbl.gov/optical_constants/filter2.html

5   Resist Performance with 10× Imaging Tools

5.1 Introduction

Photolithography results using the spatial frequency doubling technique are presented in this chapter. Scanning electron micrographs of the various photoresists are shown for several different exposure configurations. All SEM images are taken without a gold coating on the resist unless specifically stated. Single-pitch and multiple-pitch imaging were by far the workhorses of this research. This chapter also touches on other experiments, besides the F2X technique, using the 10× tools and the ALS. This includes several monolayer exposure attempts as well as a proof-of-principle phase-shifting mask result. Some non-chemically amplified resists were also tested and their results are included here. Features range from dense 140-nm lines to dense 30-nm lines covering a range of different resists. Loose-pitched linewidths were measured down to 25 nm. The coherence level for all of these 10×-system exposures was 0.8.

5.2 Single-pitch Exposures

The first optic used for exposures was the 10×-Berkeley. It exposed high-resolution patterns that extended well beyond the conventional resolution limit of 100 nm. First, printing was done without the 0th-order blocking aperture and allowed all three orders (0,+1, -1) through the system. Then the aperture was installed and printing was done

using the spatial frequency doubling technique (+1 and -1 orders only). Results for these conventional and doubled images are shown in Figure 5-1. The resist used was Shipley's EUV-2D. This resist is still the baseline for all EUV lithography systems at the national labs (Sandia, Lawrence Livermore, and Lawrence Berkeley). The sensitivity for EUV-2D is 6.8mJ/cm^2. Also included in the figure are the CCD images of the pupil plane for both cases.

Figure 5-1: Left – Conventional imaging with lowest three orders (0, +1, -1). Right – Spatial frequency doubling without the zeroth order. Resist images are EUV-2D. Thickness – 100 nm.
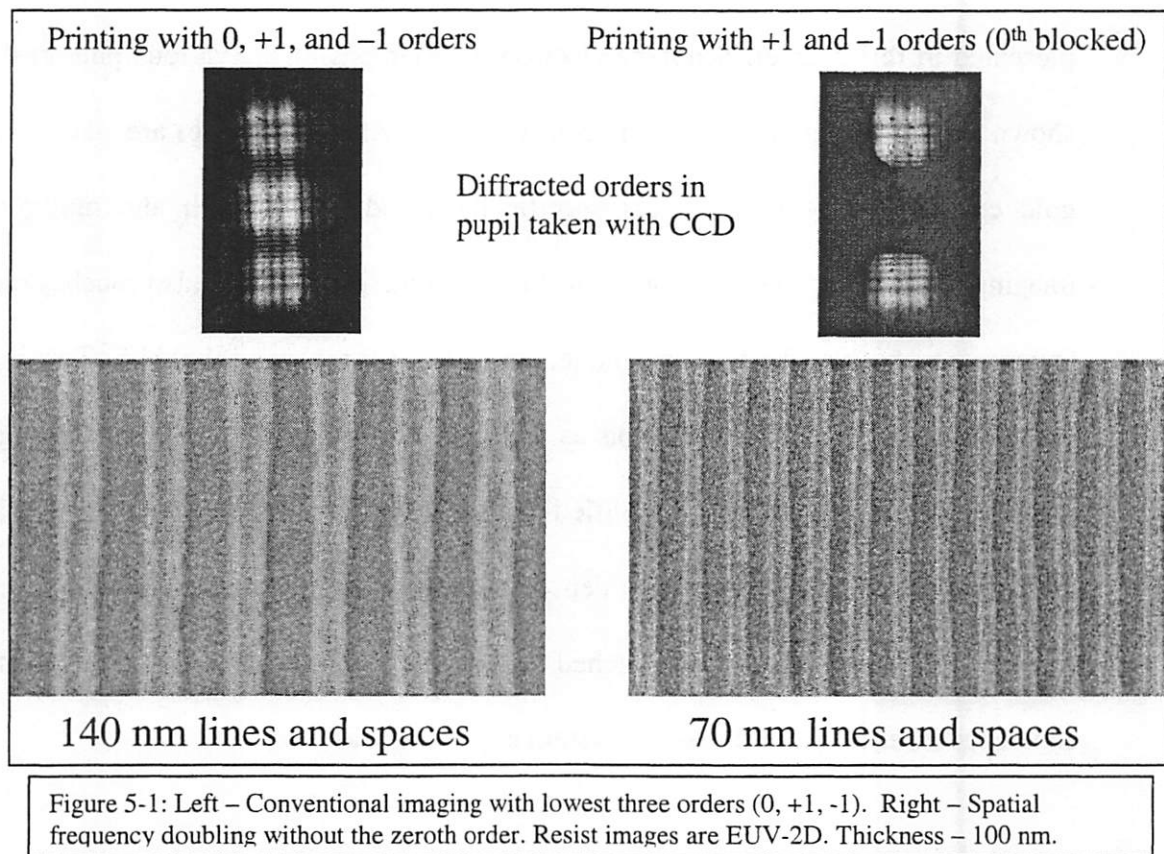
The image on the right in Figure 5-1 shows the first spatial frequency doubling ever done using the F2X system.

Figure 5-2 shows 50-nm line and space patterns in the EUV-2D resist. This image was also taken after work was done on setting up better resist processing conditions at the beamline.
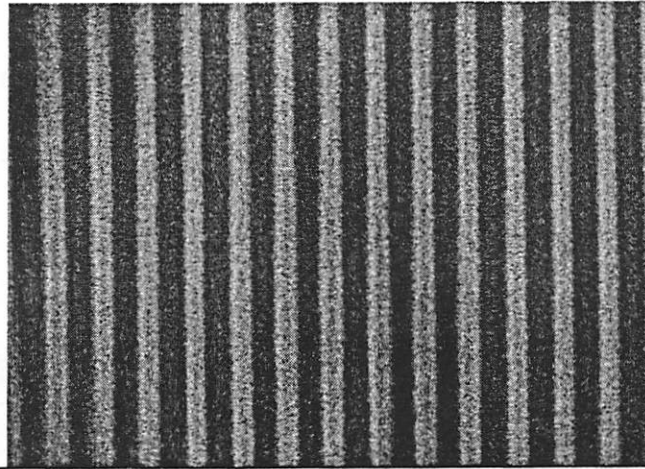
Figure 5-2: 50-nm lines and spaces with EUV-2D. (thickness - 100 nm)

What is not shown in this line and space pattern is the total 4-μm × 4-μm field. Figure 5-3 shows the full resist field for the 50-nm linewidth image taken in Figure 5-2.
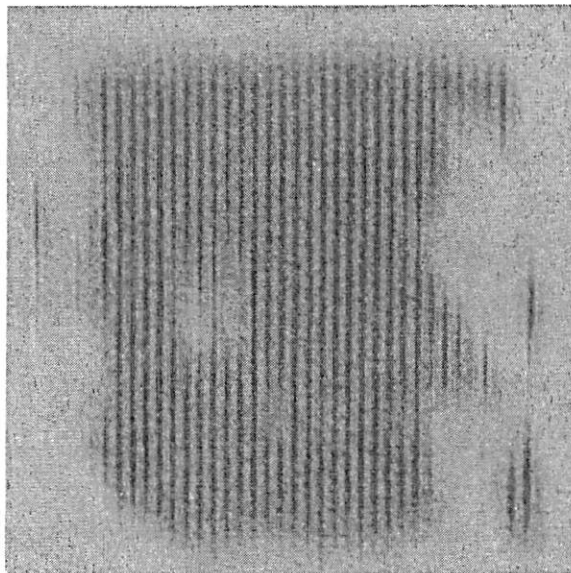
Figure 5-3: Full 4-μm × 4-μm field in EUV-2D. Field should be a full square.

A lot of work goes into steering the diffraction orders in the pupil such that a patch of the field will print well. Defects on the mirror surfaces of 10×-Berkeley, as shown in Section 3.2.4, made full-field imaging difficult but not impossible. When these resists were exposed, alignment control was also not robust (discussed in Section 4.2). Figure 5-4 shows two typical examples of field nonuniformity when defects are more abundant on the orders. Coherent illumination also amplifies these effects (there is more discussion of coherence in Section 5.6).
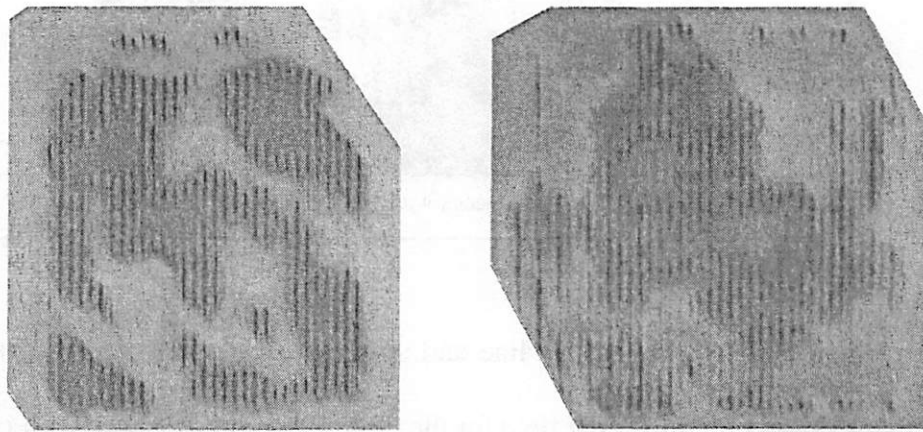
Figure 5-4: Two examples of field nonuniformity caused by defects on the multilayer mirrors. The resist is EUV-2D.

Figure 5-5 shows the best 40-nm results using EUV-2D and the 10×-Berkeley optic. Dense 30-nm features were attempted in EUV-2D but no lines would print. It was suggested based on this result that the resolution limit for EUV-2D might have been reached [1]. Others have since backed up this claim. Resist work done using the Engineering Test Stand (ETS) Set-2 optic suggested that the Gaussian resist point-spread function had a full-width half maximum of 50-55 nm [2]. Also, lithographic modeling done at Intel has shown a resist point spread function for EUV-2D to be 50 nm [3]. Being

able to print 40-nm dense lines and spaces using the 10× system is pushing the limits of EUV-2D.
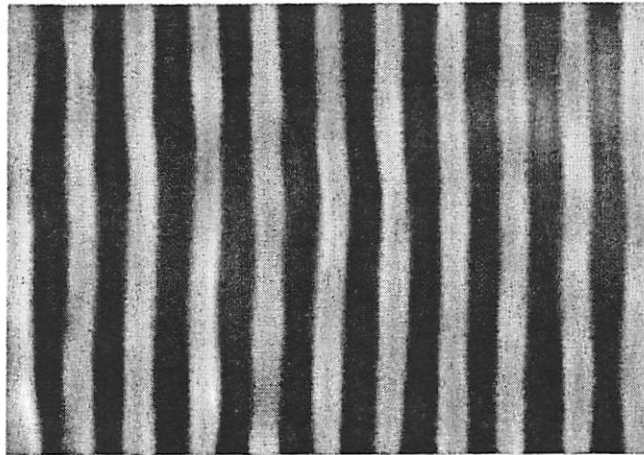
Figure 5-5: 40-nm lines and spaces printed in EUV-2D. Thickness – 100 nm

Significant improvements were not made until shooting with the 10×-Intel optic. See Figure 5-6 for 50 nm dense lines and spaces printed with this newest optic. As can be seen when compared to Figures 5-3 and 5-4, these are much better full-field patterns. There are less nonuniformities over the entire 16 μm^2 resist field. The nonuniformities are still visible but they are not as strong as in the past. A new resist was also used instead of EUV-2D. An experimental Shipley resist called XP9947W (EUV-F2X). Line edge roughness was at 4.7 nm (3 sigma rms) for these lines. EUV-F2X is less sensitive to EUV 2D by a factor of 1.3 (EUV-F2X: 8.84 mJ/cm^2).
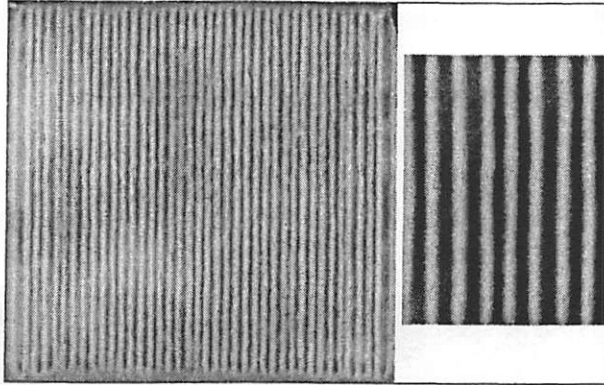
Figure 5-6: Dense 50-nm features in Shipley XP9947W (EUV-F2X).
Thickness - 125 nm.

Figure 5-7 shows the results when slightly overexposing this pattern. The lines shrink to 40 nm and the spaces are now 60 nm. Once again, a more uniform field is seen in the resist.
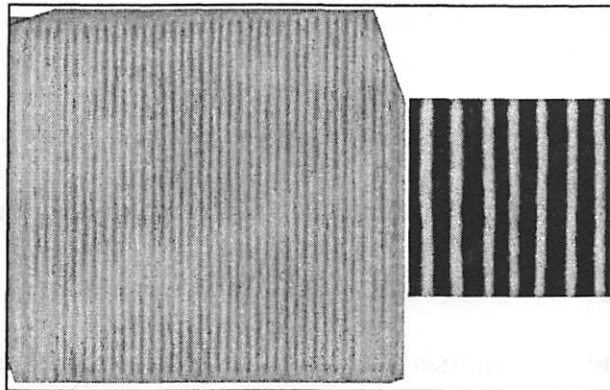
Figure 5-7: Overexposed EUV-F2X resist: 40-nm lines and 60-nm spaces. Thickness - 125 nm.

If the pattern is overexposed a little more then 30 nm loose pitch features are printed. See Figure 5-8 for an example of this in EUV-F2X.
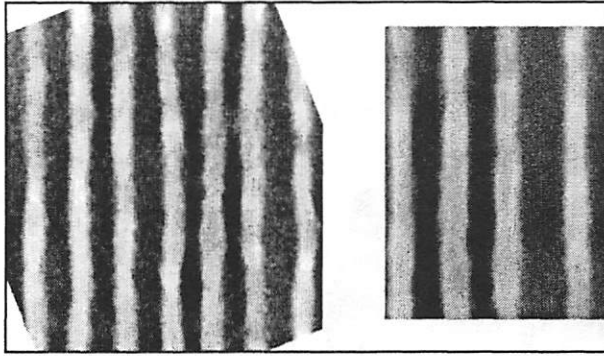
Figure 5-8: Overexposed EUV-F2X: 30-nm lines and 70-nm spaces. Thickness - 125 nm

5.3 Multiple-pitch Exposures

It is also possible to print several pitches in a single exposure using the F2X system. The imaging configuration combines the spatial frequency doubling technique with a multiple-pitch mask described in Section 4.3. By carefully aligning the object grating to a wider spatial filter, multiple linewidths can be printed at the same time. An advantage to this technique is that it removes dose and processing variations that appear across different wafers.

The multi-pitch configuration chosen was able to print several fine pitches (70, 60, 50, and 40 nm) during the same exposure. In early exposures, using EUV-F2X, dense 70, 60 and 50-nm features would print but the 40-nm results were not well defined. Figure 5-9 shows EUV-F2X results at two different focus points. Since this technique is based on interferometric methods linewidths will still print in both of these focus positions. Focus 1 is more out of focus when compared to Focus 2. This can be seen by the size and square-ness of the four pitch fields. Also noticeable in these images is that the process

87

window noticeably decreases as the features get smaller (70 nm vs. 40 nm). There are also some nonuniformities in the images.
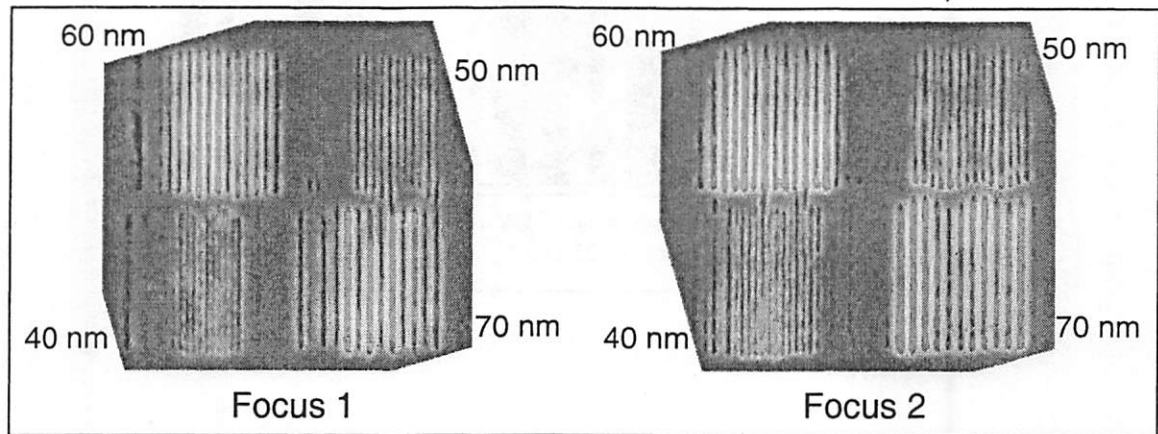
Figure 5-9: Muli-pitch image using EUV-F2X for two different focus points. Thickness - 125 nm

Figure 5-10 shows a zoomed in SEM image of the 40-nm features from the better focus (Focus 2) of Figure 5-9. This larger image shows 35-40-nm lines are visible although not printing sharply.
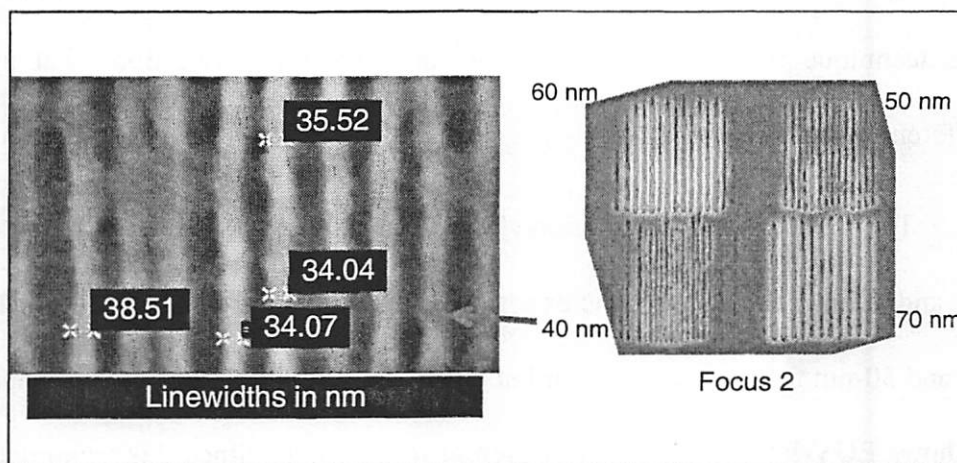
Figure 5-10: Left side shows a higher magnification picture of Focus 2 from Figure 5-9.

When these multi-pitch patterns are overexposed small features can be printed in EUV-F2X. This is shown in Figure 5-11 where dense 70 nm lines are overexposed to show sub-30-nm loose-pitch lines. This image has been gold coated.
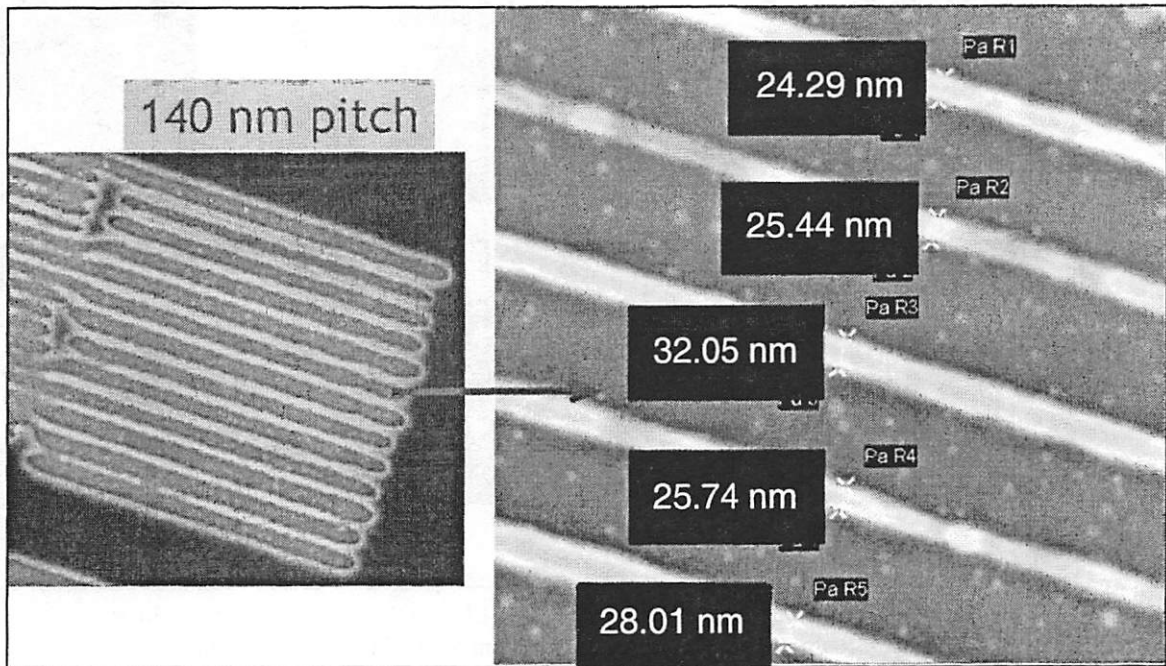
Figure 5-11: Left: Overexposed 70-nm features in Shipley EUV-F2X. Right: Sub-30 nm features. Thickness - 125 nm. Gold coated images

By changing the dose on dense 140-nm lines, linewidths ranging from overexposed 50-nm to underexposed-180-nm were printed in this resist. Figure 5-12 shows this large range of linewidths. These images demonstrate the sinusoidal nature of the aerial image intensity from the F2X system.

Sinusoidal Contrast

Highest dose

Linewidths in nm

50 nm | 79 nm | 95 nm | 105 nm

122 nm | 130 nm | 149 nm | 180 nm

Lowest dose
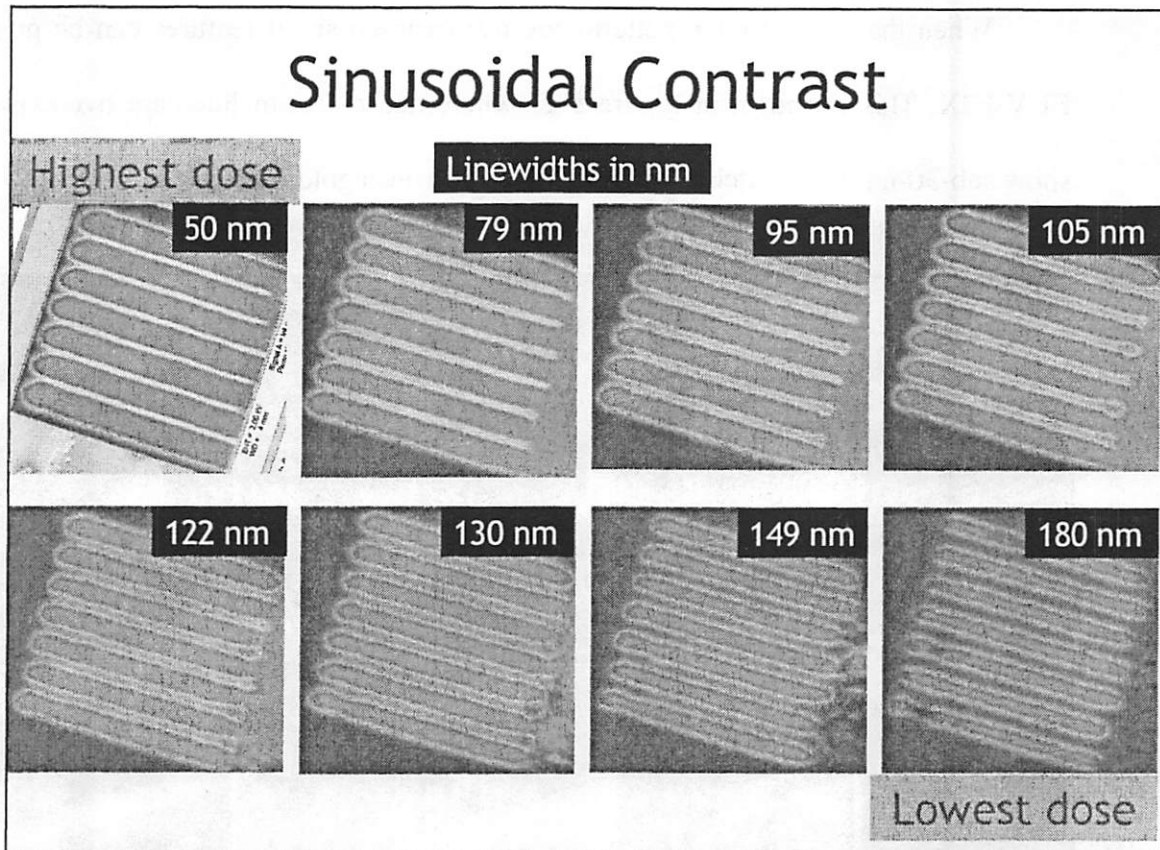
Figure 5-12: Sinusoidal contrast demonstrated in EUV-F2X with 140-nm dense lines. Overexposed 50-nm lines to underexposed 180-nm lines. Thickness – 125 nm.

Another chemically-amplified, EUV resist from Shipley (1K) has recently outperformed the other test resists described above in terms of resolution. As shown above, the other resists were only partially clearing the 40-nm dense patterns. Figure 5-13 shows Shipley 1K clearing the 40-nm lines and is the best performing chemically amplified resist tested in the F2X system. As far as sensitivity is concerned, Shipley 1K is approximately four times slower than EUV 2D (Shipley 1K sensitivity – 27 mJ/cm^2).
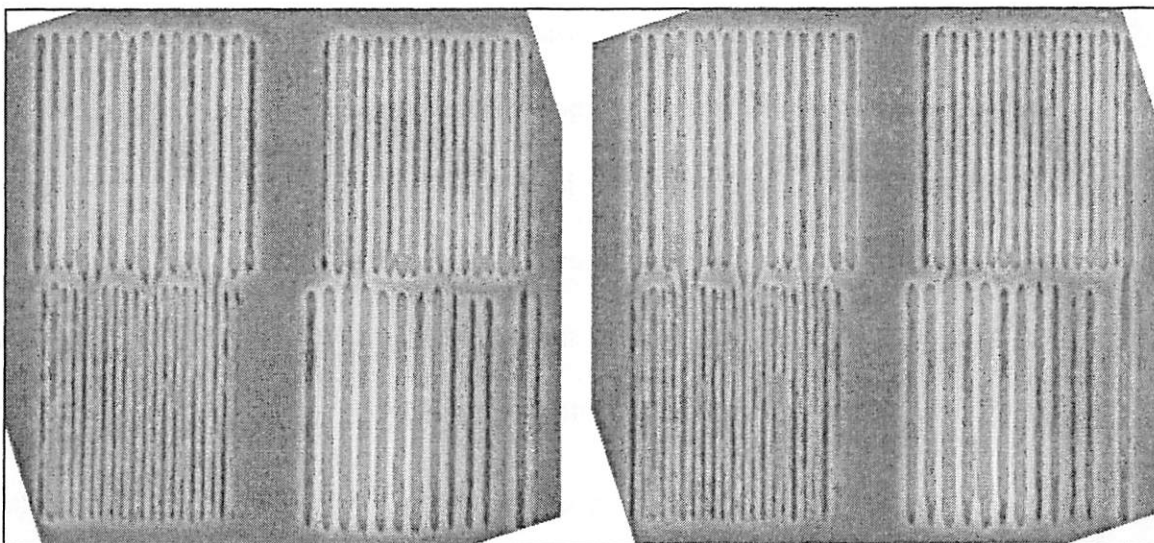
Figure 5-13: Multi-pitch images using Shipley 1K resist. All feature sizes are resolved. The image on the left is a slightly higher dose than the image on the right. Thickness – 125 nm. Clockwise from upper left for each image – 60, 50, 70, 40 nm lines and spaces.

Based on the performance of Shipley 1K, it was the resist used in the aerial image contrast experiments (Chapter 6).

5.4 Extension Exposures

This section details examples of two other explorations attempted with the 10×imaging station. The first, done with 10×-Intel, is an attempt to expose a monolayer at EUV in order to promote directed assembly. The second, using 10×-Berkeley, focused on printing a phase shift mask designed for EUV wavelengths.

5.4.1 Monolayer Exposures

A collaboration with Itai Suez, a graduate student in Professor Frechet's group (UC Berkeley, Dept. of Chemistry) was formed to investigate using EUV lithography with their chemistry-based directed assembly techniques [4]. In particular, we looked at using EUV radiation to selectively deprotect regions of a monolayer bound to a silicon

substrate. After exposure, when the wafer was placed in a dendrimer solution, the goal was to have the dendrimers only attach to the sites deprotected by the EUV radiation. Their bottom-up surface activation idea previously used an atomic force microscope (AFM) tip to deprotect the monolayer. Using an AFM as an imager is time consuming and only allows the creation of very small fields. To speed up this writing process, EUV photons were used to print patterns into the monolayer.

Since the attached dendrimers sit only a few nanometers from the monolayer, the features cannot be seen optically and so an AFM must be used to measure dendrimer attachment. To print larger fields and to help in finding the features in the AFM, we moved to printing in the 10× system without an object grating. This way the imaging system essentially re-imaged the out-of-focus 0.5-μm coherence pinhole. The aperture stop was rotated to the 4mm opening and EUV resist exposures were tested. Figure 5-14 shows both the aperture and its diffracted image in exposed photoresist. This image contains many shapes and sizes which would be fine for testing the dendrimer lithography. Plus the fields are large enough that they should be found using an AFM.
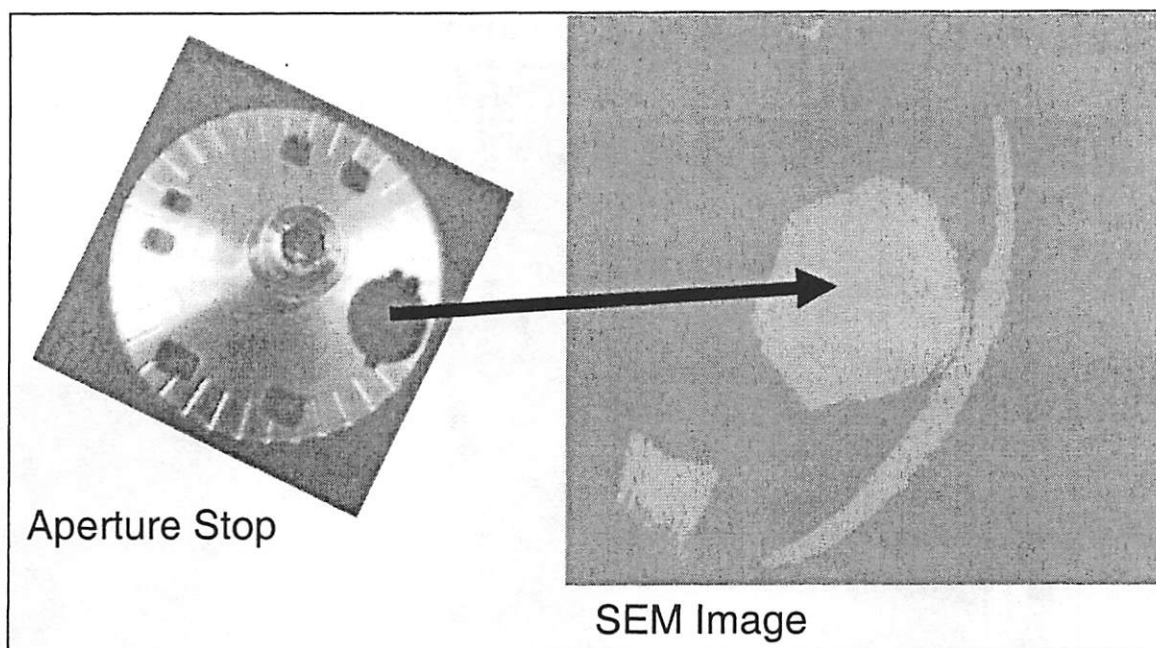
Figure 5-14: Illumination through the aperture prints a diffracted image of the aperture into resist. The rectangle in the bottom left is 8-μm wide. Resist – EUV-F2X, 100-nm thick.

Next, a monolayer coated on a 4-inch silicon wafer was put in the 10× system for exposure. EUV radiation did react with the monolayer and patterns were created. However, the dendrimer did not appear to stick in the exposed regions. The AFM image in Figure 5-15 shows clearly the correct exposure shape in the monolayer when compared to the EUV resist sample. Height measurements with the AFM show a hole in the exposed region rather than a nanometer-sized dendrimer sitting above the monolayer. It appears that the EUV photons were too energetic and blasted the monolayer off of the wafer surface rather than simply deprotecting it.

AFM Phase Image of Monolayer

SEM Image of EUV Resist
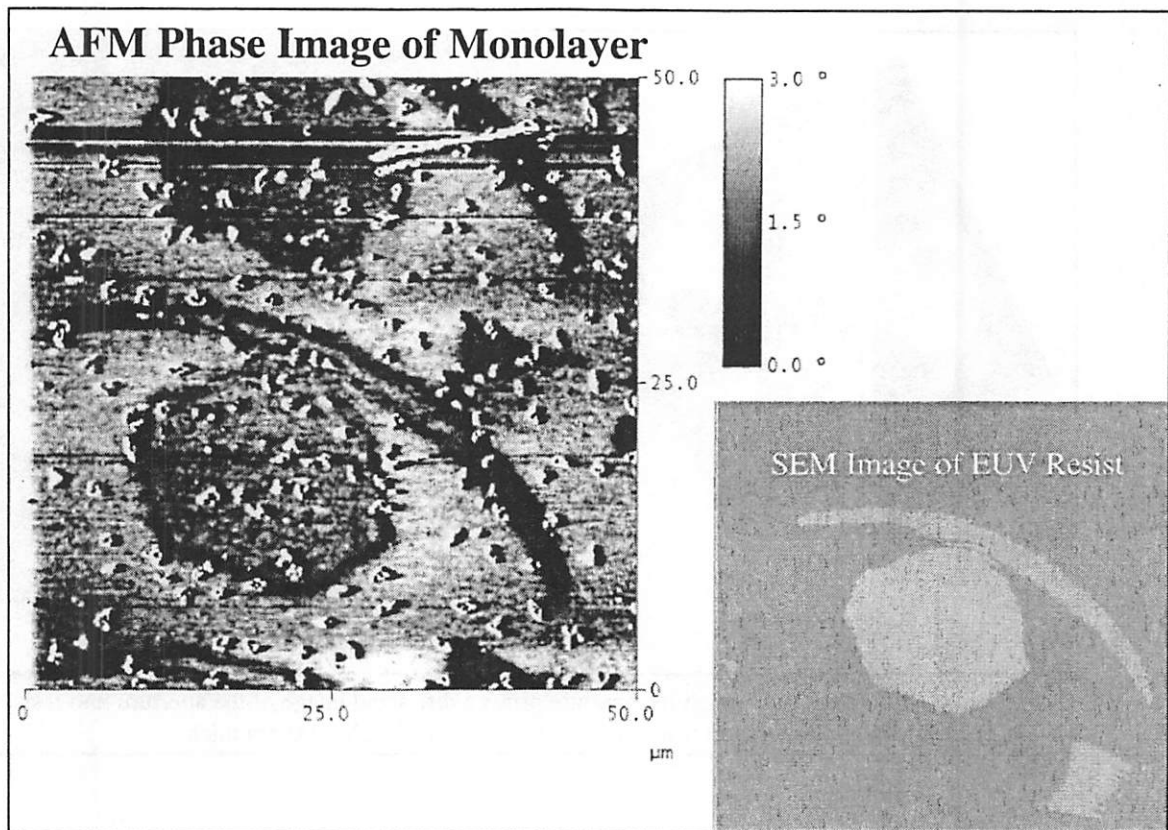
Figure 5-15: Images of the EUV-exposed monolayer and in EUV resist of the aperture stop field.

5.4.2 Phase Shift Mask Exposures

The 10×-Berkeley system was used to print a transmission-type attenuated phase shift mask (APSM) at EUV wavelengths. Using an APSM is essentially a different way to do spatial frequency doubling without the need for an aperture filter for the zeroth order. Chang Cho, Sang Hun Lee, and I (all at UC Berkeley at the time) collaborated on exposing wafers using this APSM technology in a proof-of-principal experiment. A molybdenum (Mo) phase shifter was used due to its relatively low absorption and high

refractive index at 13.4-nm radiation. Previously, others had used a polymethyl methacrylate (PMMA) phase shifter and germanium absorber [5].

The final structure for the EUV APSM was an 86-nm thick (π phase shift) patterned Mo layer on a 100-nm thick Si_3N_4 membrane. Actual phase-shift was measured to be 120°-140° (about 80 nm) for 5-μm equal lines and space features, with 43% EUV transmission through the Mo phase-shifter.

Images of developed photoresist are shown in Figure 5-16. EUV-2D was used with a thickness of 110 nm. The left shows conventional imaging of an 8 micron pitch grating which created an 800 nm pitch in the photoresist. The right side shows resist images using the APSM. Doubled lines are observed indicating that the phase shifting was successful. The LER that is evident is caused by particles and dirt on the APSM. The defects on the 10× Berkeley optic would have also contributed to this imaging performance.

Image created with binary mask   Image created with APSM

Figure 5-16: Demonstration of APSM mask in EUV-2D resist. Thickness – 110 nm. Left – 800 nm lines printed with a binary mask. Right – 400-nm lines created by using an APSM.
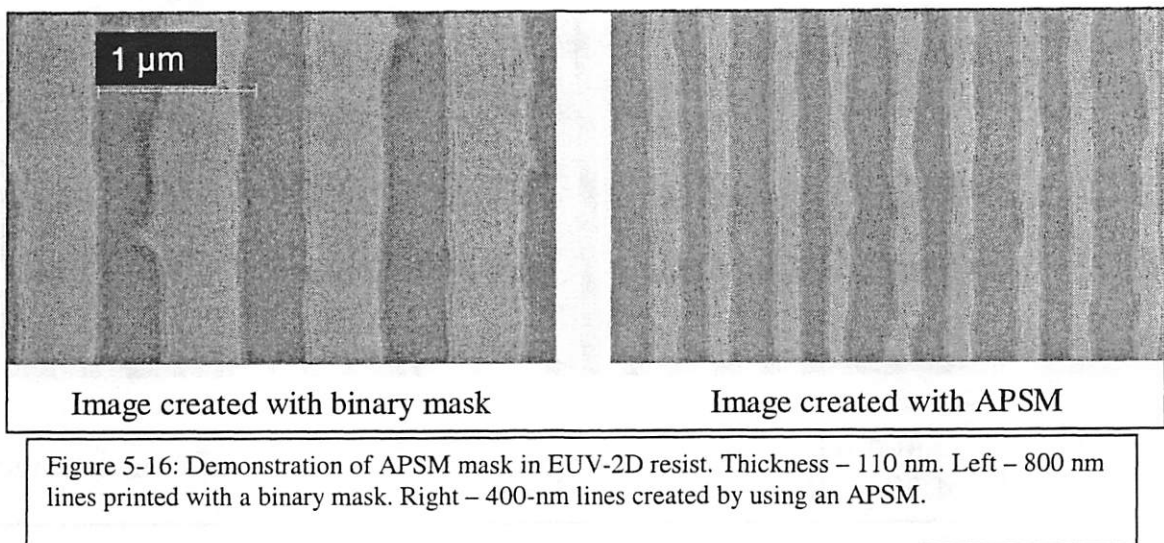
5.5 Line Edge Roughness (LER)

One of the important properties for resists is their line edge roughness (LER). As discussed in Chapter 1, large LER can degrade the performance of transistors. Several of the line and space patterns shown in Section 5.2 were measured for LER in order to check how the EUV resists were performing. Note: line roughness will also be discussed in Section 6.3.2 when discussing aerial image contrast.

In particular, line edge roughness (LER) measurements were taken on the dense 50-nm line and space pattern printed in Shipley EUV-2D resist (Figure 5-2). Figure 5-17 shows two measurements taken on the same wafer. The 3 sigma rms roughness was shown to be around 4 nm. This can be compared directly to Sandia's 100nm dense patterns (with a LER of 6 nm) since the same measuring equipment was used on the same resist [6]. This comparison is important because it indicates higher contrast is achieved in

Figure 5-17: LER values for 50-nm lines and spaces printed in Shipley EUV-2D. Image is gold coated. Thickness – 100 nm.
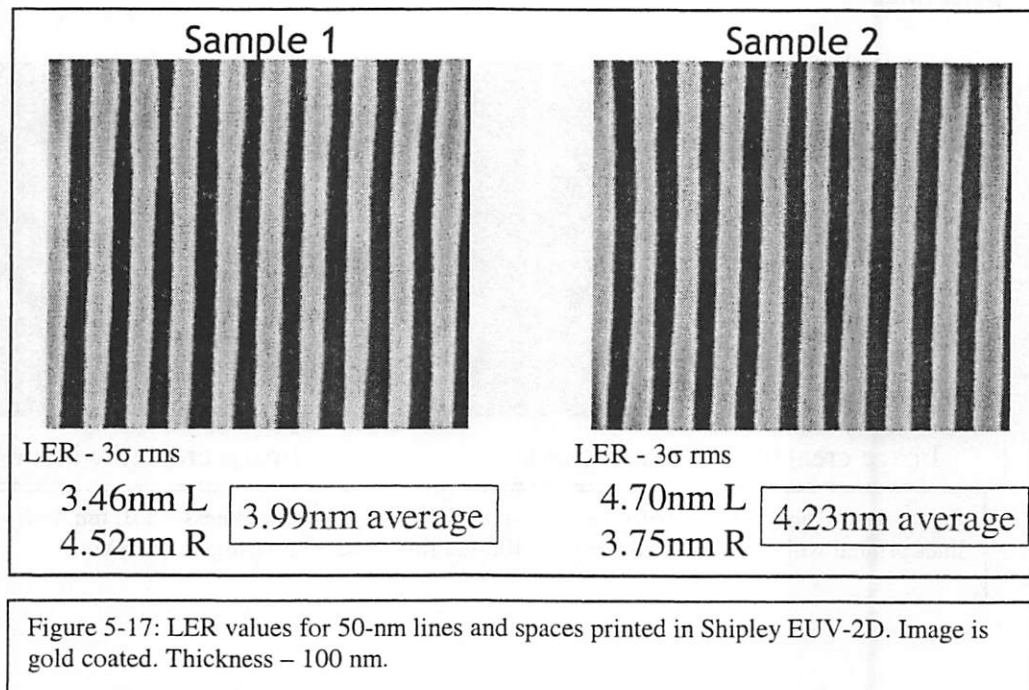
the F2X system. The LER that Sandia saw was larger for larger linewidths. If they had comparable contrast to the F2X system then they should be getting a lower LER than 6 nm.

LER measurements were also taken on EUV-F2X resist (Figures 5-6 and 5-7). These were done at Intel with their in-house tools. The gold-coated images and LER measurements are shown in Figure 5-18. Three-sigma LER values are below 5 nm rms. As is typically seen, an overdosed line has a slightly better LER measurement. These numbers are directly comparable to Intel's resist data since the same tools were used.

47.4 nm lines and LER = 4.8 nm rms   37.5 nm lines and LER = 4.3 nm rms

Figure 5-18: LER measurements for EUV-F2X (3 sigma values). Gold coated images.
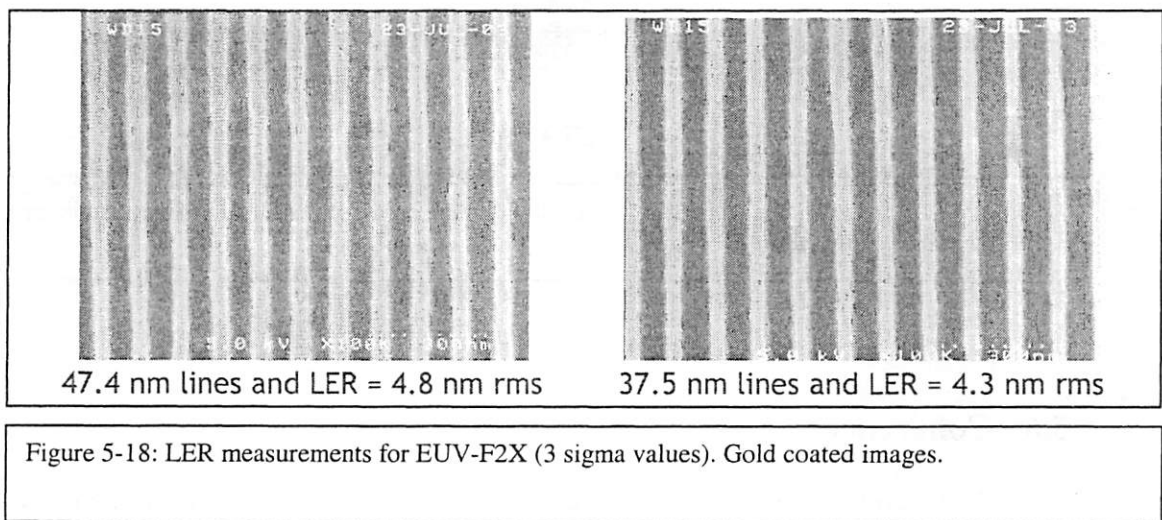
Figure 5-19 shows Intel data for a wide selection of EUV resists tested at 100 nm lines and spaces. Also noted is Intel's target range for resists by 2007. The results in Figure 5-18 would be on the leading edge of this plot and closest to the target (sensitivity: 8.84 mJ/cm^2; LER: 4.8 nm). This is also for 50 nm linewidths - half as big as those tested

in Figure 5-19. The F2X system is printing at comparable or better LER for half the feature size. Even better LER numbers will be shown in Section 6.3.2.

Sensitivity vs. LER
Intel Data

Resist Vendors

■ A
▲ B
◆ C
◉ D

Target for 2007

Figure 5-19: Intel data showing LER vs. sensitivity done on the 10× microstepper at Sandia printing 100-nm lines and spaces. [7]
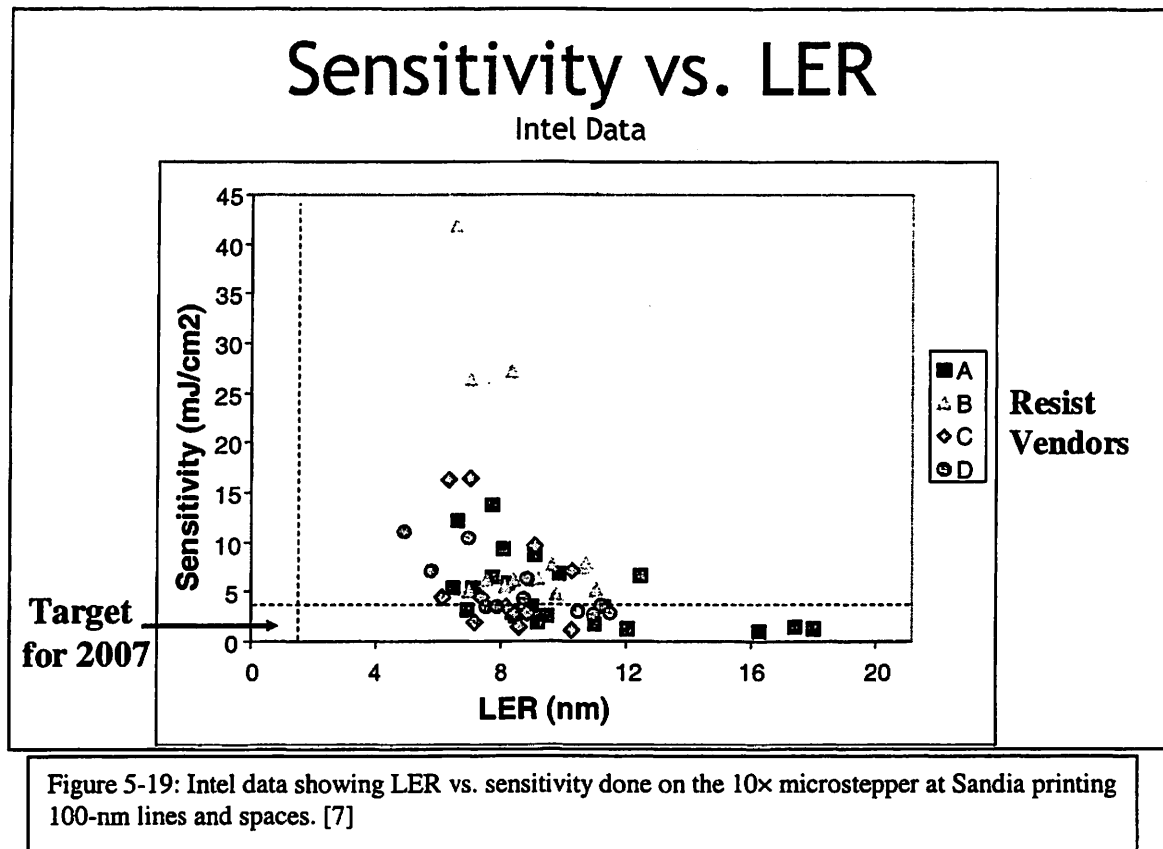
5.6 Coherence

A coherent illumination source is what makes the spatial frequency doubling technique possible. It allows for extending the useful NA of the 10× system to print the small features shown earlier in this chapter. There are, however, adverse coherence effects which must be battled. This, of course, includes the edge-ringing effects like the ones from the aperture stop (see Section 2.3.2). Furthermore, any defect in the multilayer mirrors or mask becomes amplified due to the high coherence from the undulator beamline ($\sigma < 0.1$) [8]. .Figure 5-20 shows an example of a peculiar field nonuniformity

that was observed when trying to image 50-nm lines and spaces using EUV-2D. In Figure 5-20(a), a CCD image of the pupil fill shows a dark spot present in the upper diffracted order. Figure 5-20(b) is a SEM of the resist-coated wafer after exposure through the system as recorded in Figure 5-20(a). It appears that coherence ringing is amplifying this defect on the multilayer. In a partially coherent system the contribution from this spot would be somewhat reduced, but here we see its full effect.

Figure 5-20: a) Diffracted orders in the pupil for 50-nm lines and spaces. B) SEM image of field nonuniformity
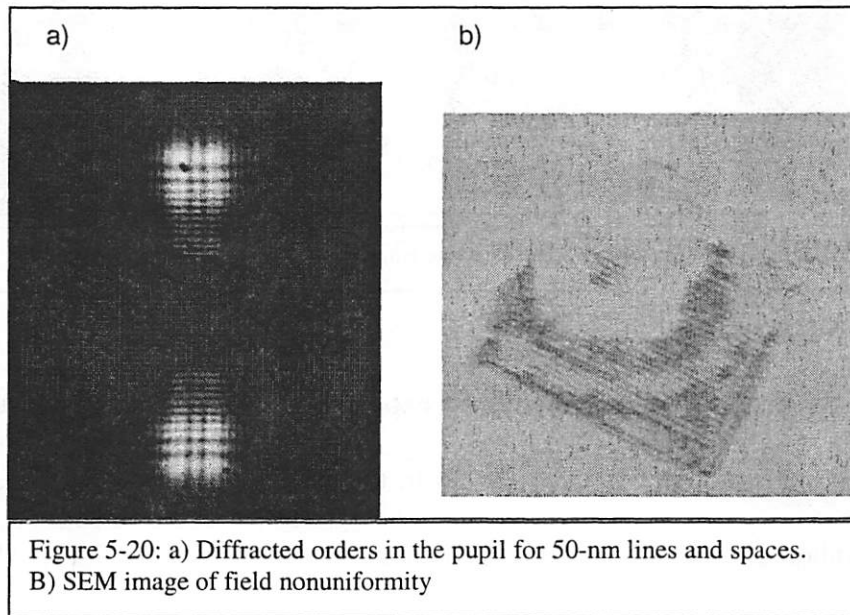
Simulations were done to prove this was a real coherence effect. Figure 5-21 shows results modeling this experiment. A circular spot was placed on one diffraction order at the pupil plane as seen in Figure 5-21(a). The defect placed in the aperture stop plane was programmed as a 70% absorber. The 70% value for the defect was obtained from the experimental CCD image in Figure 5-20(a). No phase adjustment was added for the defect. Figure 5-21(b) shows a ringing pattern in the image plane similar to what was witnessed in the actual experiment (Figure 5-20(b)). This simulation demonstrates the

detrimental effects of contamination on the optic's mirror surfaces as well as the success

of the computer model.
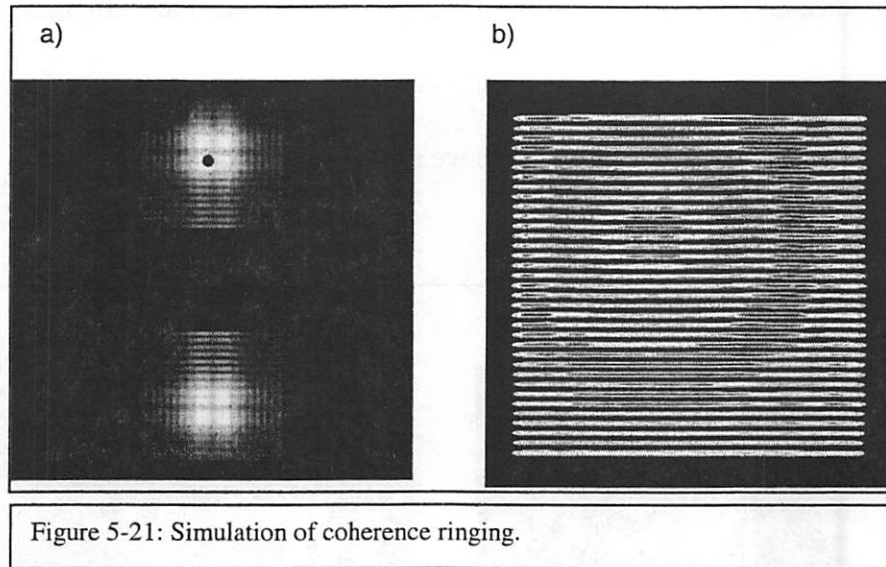
Figure 5-21: Simulation of coherence ringing.

When working on the monolayer exposures (Section 5.4.1) exposures were done

that also highlight the coherence effects in the system. The exposures were made using

simple pinhole illumination and an open aperture window (Figure 5-14). This was done in

EUV-F2X and the exposures clearly show coherence ringing of the aperture window

edge. Figures 5-22 contains four dose steps and shows concentric rings appearing. These

are caused by the coherent illumination being used.
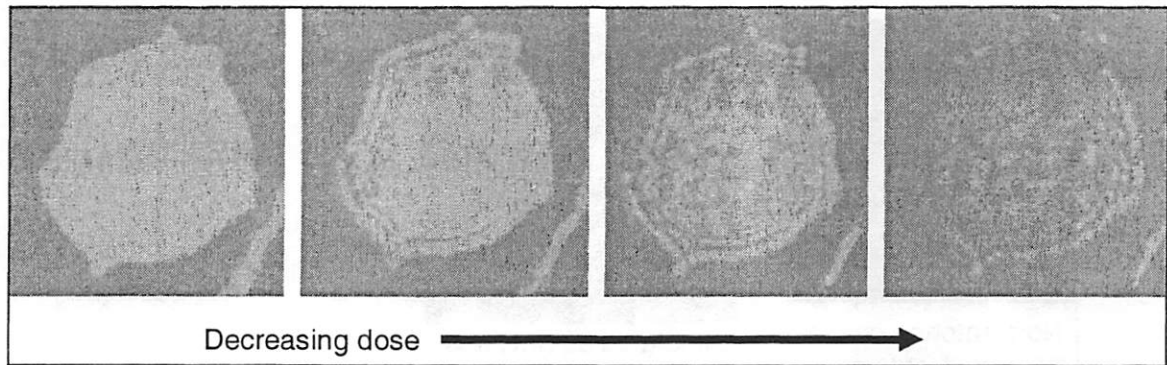
Decreasing dose ➡️

Figure 5-22: Coherence ringing from the aperture edge printed into EUV-F2X. Dose is decreasing from left to right and concentric rings become visible in the resist.

Section 3.2.4 showed pupil images of several different 10× systems (Berkeley, A, B2, and Intel). As mentioned there, 10×-Intel showed a new polishing scratch that had not been seen previously in the optic series. While this optic was delivered to the requested specifications, this roughness pattern was disturbing to see. A simulation was run in MATLAB where scratches were added to the imaging system to look at performance. Marks of similar size and attenuation were place onto the diffracted orders in the pupil plane. Figure 5-23 shows the simulation results and how polishing marks affect the imaging performance. Both cases in the figure show high contrast, but there is more variation across the field when the polishing marks are present. This result helps understand the field nonuniformities seen when exposing with 10×-Intel.

No scratches on the +1 and -1 orders

Simulated 50 nm lines with no scratches

cutlines

Scratches simulated on optic (50% absorbing)

Simulated 50 nm lines with scratches

Figure 5-23: Simulation of 10×-Intel polishing marks. Top line shows no roughness added for imaging 50-nm lines and spaces. Bottom line show simulated scratches and the associated imaging performance.
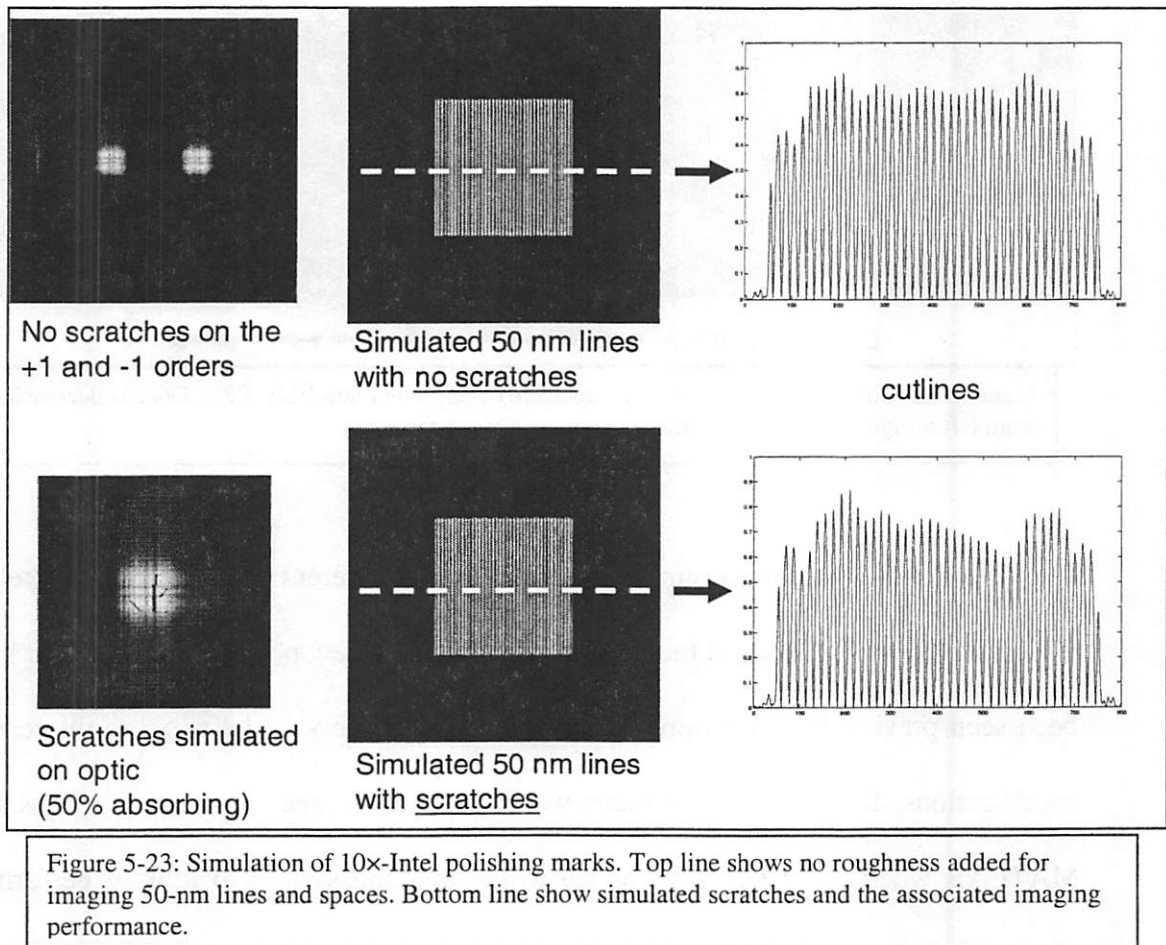
5.7 Non-Chemically Amplified Resists

Two different non-chemically amplified (non-CA) resists were tested using the F2X system. The first was polymethyl methacrylate (PMMA) which is a workhorse polymer with many semiconductor processing uses [9,10,11]. The second is hydrogen silsesquioxane (HSQ) which is a negative tone resist [12]. Even though HSQ is known for some processing instability, it is used as an e-beam resist due to its high resolution capabilities around 20 nm.

PMMA was tested in several different exposure configurations. First, single pitches were exposed with a very thick (250 nm) PMMA resist that was formulated in

102

chlorobenzene. These were done with the 10×-Berkeley optic. Figure 5-24 shows these 50-nm features. The PMMA images have about a 5-nm gold coating to help minimize resist charging. PMMA is 3.4 times slower than EUV-2D (PMMA sensitivity – 23.1mJ/cm^2).
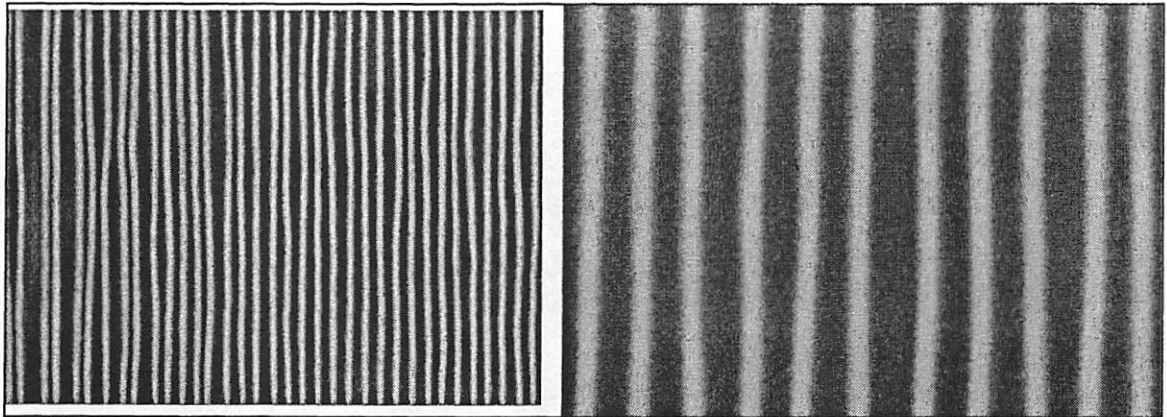
Figure 5-24: 50-nm lines and spaces in PMMA. Thickness – 250 nm. Gold coated.

Figure 5-25 shows SEM images of PMMA resolving 40-nm dense lines and spaces. Once again, these images are gold coated and the resist was 250 nm thick.
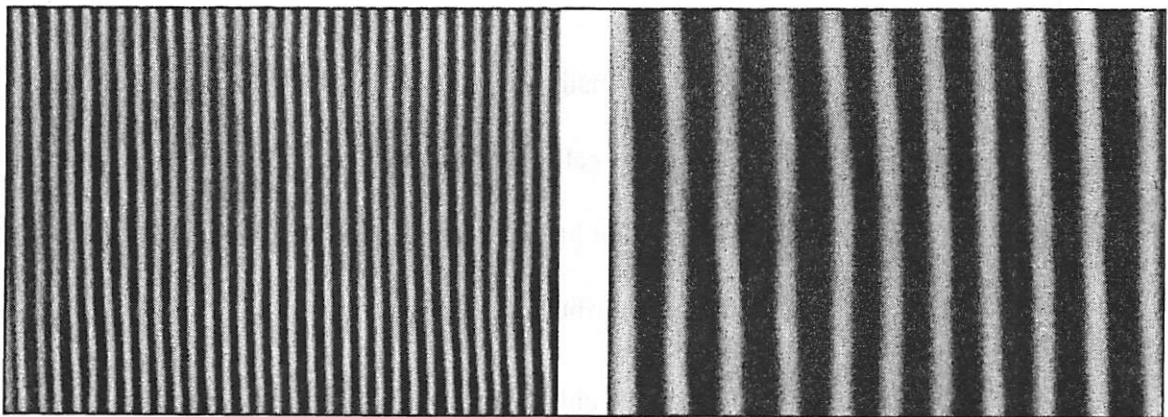
Figure 5-25: 40-nm lines and spaces in PMMA. Thickness – 250 nm. Gold coated.

Finally, Figure 5-26 shows 30-nm features in PMMA with chlorobenzene. This resist was also 250 nm thick and was gold coated after the exposure. The resist thickness is important especially when looking at these 30-nm lines. With this PMMA thickness, the aspect ratio is 8.3:1 which can partially explain both the waviness in the lines and the way they appear to be falling in on one another.
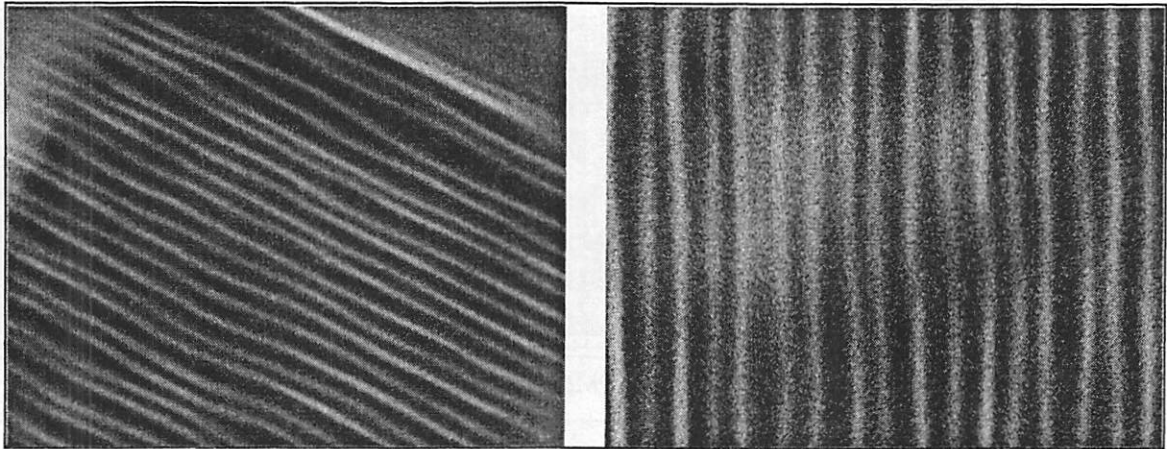
Figure 5-26: 30-nm lines and spaces in PMMA. Thickness – 250 nm. Gold coated.

Attempts were made to print these same features use a thinner PMMA solution at a 100-nm resist thickness. This PMMA resist was formulated in the less hazardous chemical, Anisole. Attempts were made to print both 40- and 30-nm lines and spaces. Resist charging during SEM investigation, however, was too great to see any features. Gold coating of the samples provided little benefit. Both the different formulation and the thinness of the resist could have contributed to the high charging.

Finally, thinner PMMA with chlorobenzene was tested using the multiple-pitch system with the 10×-Intel optic. The resist was spun on 100 nm thick in this case. The imaging capabilities of the multi-pitch system are demonstrated nicely in Figure 5-27.

Comparing this image with the best CA resist example (Figure 5-13), the PMMA image shows less field nonuniformity.
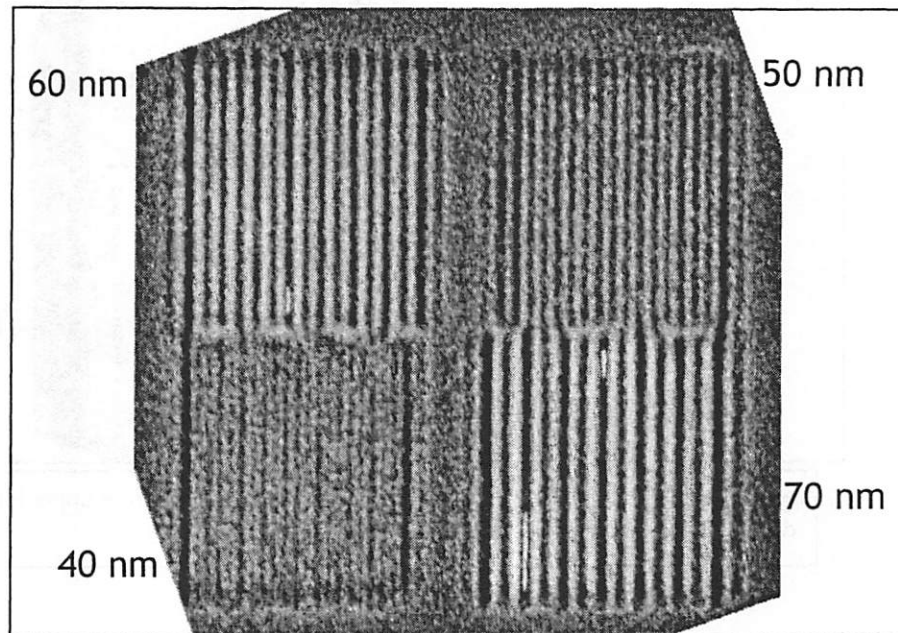
Figure 5-27: Multiple-pitch image in PMMA resist (clockwise from upper left: dense 50, 70, 40, 60 nm lines). 100-nm thick. Gold coated image.

HSQ was also tested in this multi-pitch setup using the 10x-Intel optic. Figure 5-28 shows (without gold coating) very clear linewidths for all feature sizes. This negative tone resist performed well at dense 70-, 60-, 50- and 40-nm features. The image is shown slightly out of focus, but once again, due to the interferometric nature of the system, well-defined features are still printed. HSQ is close to 11 times slower than EUV-2D (HSQ sensitivity – 73mJ/cm').
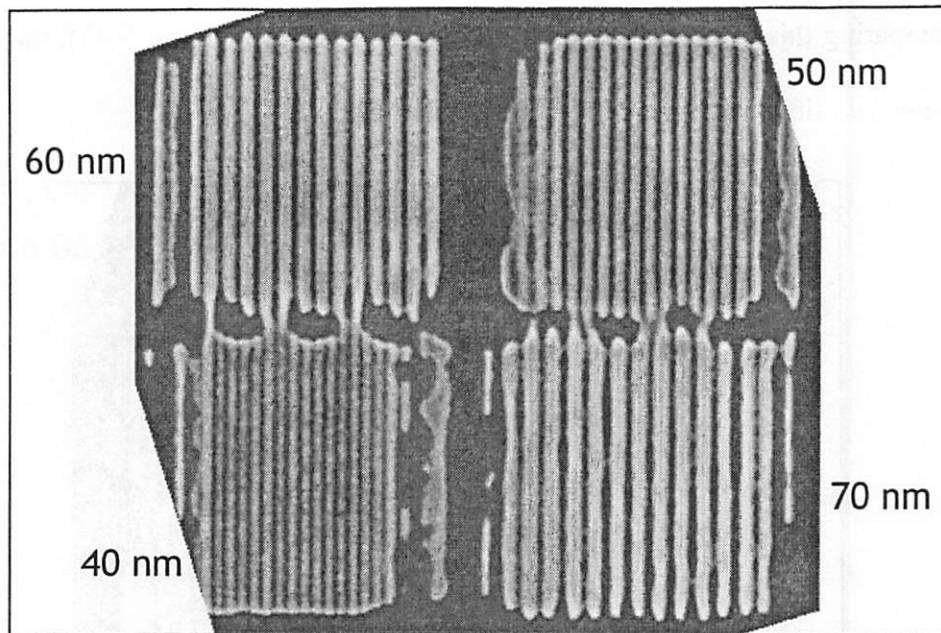
Figure 5-28: Multiple-pitch image in HSQ resist (clockwise from upper left: dense 50, 70, 40, 60 nm lines). 62-nm thick. No gold coating.

When overexposing the HSQ resist loose 28-32 nm linewidths were printed. An SEM of these features is shown in Figure 5-29.
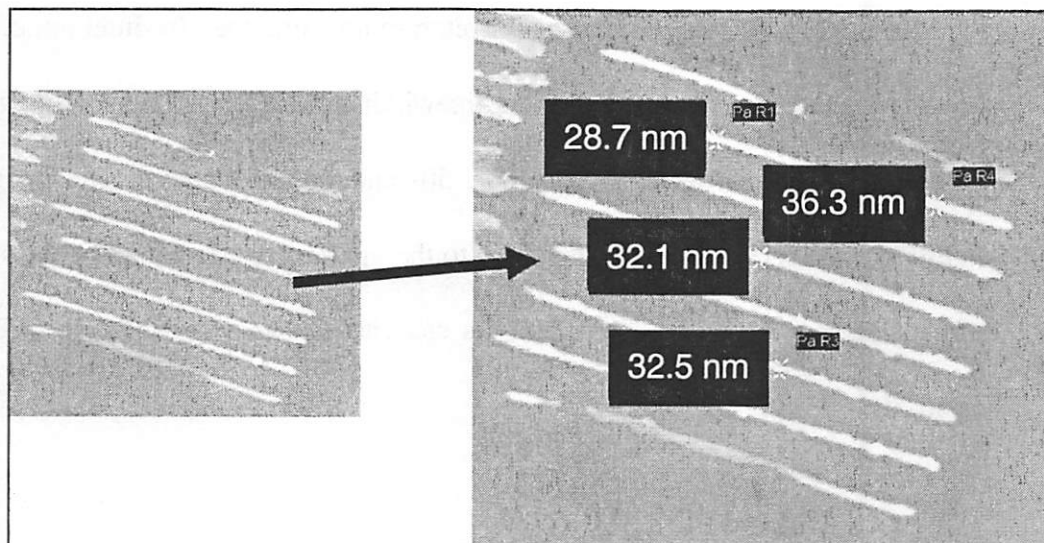
Figure 5-29: Overexposed 70-nm lines in HSQ. 62-nm thick. No gold coating.

Both PMMA and HSQ have shown good resolution for EUV testing. Unfortunately when compared to EUV-2D, PMMA is approximately 4 times slower and the HSQ requires close to 11 times more dose. Even though they perform well at EUV they are too slow for commercial purposes. There is an additional resist outgassing concern with PMMA and it is not even allowed in tools like the Micro Exposure Tool (MET) or the Engineering Test Stand (ETS).

5.8 Environment

The purpose of this section is to describe several environmental factors surrounding the F2X system. For example, chamber temperature was not controlled beyond the ambient temperature of the ALS facility. Temperature impact on the experiments was mitigated by the simplicity of the imaging system including the large depth of focus in its design. Temperature variation surely cause alignment and focus drift in the system but they were small enough effects that imaging could proceed. It is, however, a far step from the MET climate control chamber which holds that system to a 0.001°C resolution. The F2X system is helped by the facts that the field being printed is small (16 μm^2) and the interferometric nature of the imaging creates a large depth of focus. Absolute focus most likely drifts during a wafer run but it is a small enough change that images will still print.

Before the last system upgrades, each wafer was exposed to ALS building lighting before going into the chamber. This did not hurt the EUV-2D wafers but other, more sensitive resists, could not handle that additional exposure.

One more effect seen was in regards to oxygen flow when exposing resists. General practice was to flow oxygen through the system during all stages of alignment and

exposure. This was to keep the coherence pinhole from clogging up from carbon deposition. While oxygen mitigates that issue it was discovered at one point that there was degradation in the resist image quality (t-topping and added roughness) when oxygen was flowing.

It was suggested that the EUV radiation was creating oxygen radicals that were in turn attacking the photoresist. To test this, I exposed without any oxygen. Oxygen, however, was used to clean out the pinhole between wafer runs. This seemed to solve the problem. Figure 5-30 shows imaging results with and without oxygen flow.

With Oxygen Flow   **Without Oxygen Flow**
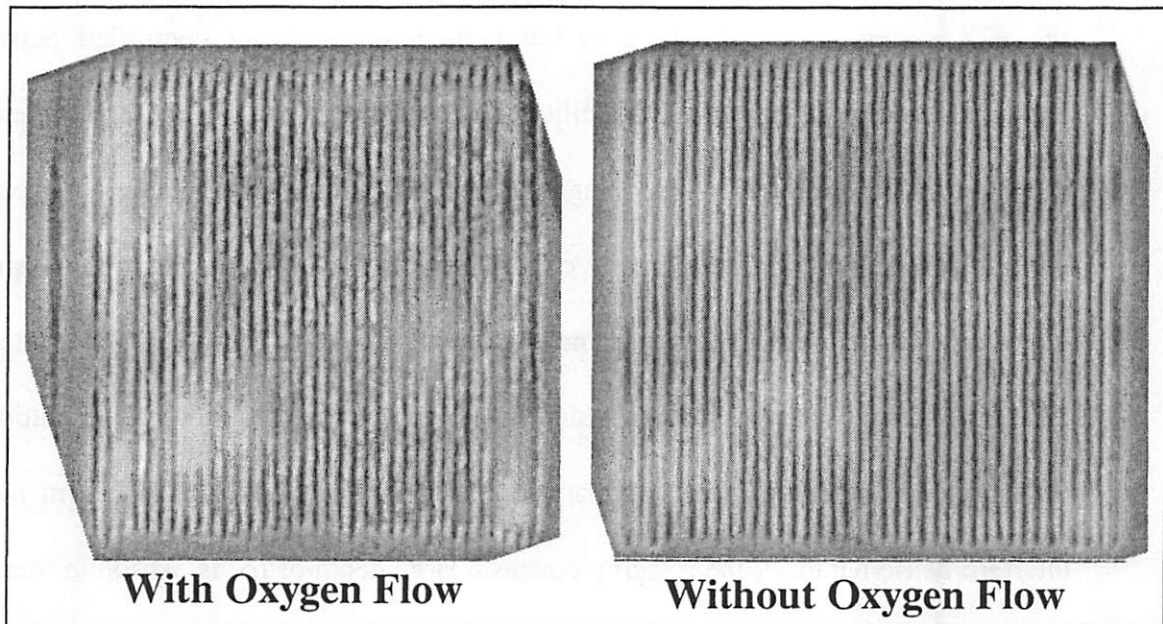
Figure 5-30: 50-nm lines and spaces printed into EUV-F2X with and without oxygen flow. This degradation was traced to contamination in the oxygen source.

In the end, a series of Residual Gas Analyzer (RGA) scans showed contamination in our oxygen source. Once a research-grade oxygen source was installed, the quality improved even when oxygen was flowing during exposures which became standard practice.

Amines have been shown to be a problem in resist imaging [13]. This could also help explain some of the resist profile variation seen in these experiments. To reduce amine effects in resist processing, a new station directly adjacent to the beamline was installed that included filters to control amine levels during the spinning, baking, and developing of the resists. The exposure station, however, remained in the open air of the ALS experiment floor.

5.9 Conclusion

This chapter covered the EUV exposures done with the 10× tools. Topics included resolution, performance of CA versus non-CA resists, single-pitch and multi-pitch imaging, and line edge roughness. Discussions on coherence effects and environmental contributions were also included.

Many test resists did not perform well in this system. This is to be expected since resist manufacturers are trying new things to meet the performance requirements. When this research started, Shipley's EUV-2D was the baseline resist. Although it still is the baseline for the MET experiments, several resists have been shown to have better resolution, but not necessarily better sensitivities. For example, Shipley's 1K has better resolution performance than EUV-2D but it is four time slower. In this research, EUV-2D feature sizes ranged from dense 140 nm features down to dense 40-nm features. Attempts were made to print at 30 nm without success. Corroborated by other research, it appears that this is in fact the resolution limit of EUV-2D.

Non-chemically amplified resists (PMMA and HSQ) imaged quite well in this system. Unfortunately, they are not practical in a commercial setting due to high dose

requirements and, for PMMA, outgassing concerns. However, using them in conjunction with the bright undulator source is not a problem.

Line edge roughness measurements were also shown. It is important to be aware of reporting differences when comparing LER numbers. Different SEM tools, software programs, gold coating amount, and software threshold levels all impact the measurements. The results shown in this chapter were measured with the same SEM's and software as the comparison data from Sandia and Intel respectively. LER for EUV-2D was shown to be 4 nm rms (3 sigma) for dense 50-nm lines. LER for EUV-F2X was 4.8 nm rms (3 sigma). By current EUV imaging standards, these are some of the lowest LER values for dense features. This helps emphasizes the high contrast that is possible with this printing technique. LER data for Shipley's SK1 will be shown in Chapter 6.

Multiple pitch images were also made on the 10x-Intel optic by extending the F2X spatial-frequency doubling technique and incorporating four feature sizes in a single exposure. Shipley's EUV-F2X and 1K resists both performed well in this configuration, as did the non-CA resists.

One of the hopes for the multi-pitch data was to compute linewidth versus dose plots for various resists. In general, having this linewidth vs. dose data would allow for the ultimate resolution of a resist to be calculated. By assuming a Lorentzian shape for the resist line spread function (LSF) one can determine the resolution (the full width at half maximum of the LSF). This has previously been demonstrated in the deep-UV [14]. In addition, one would want to print the multiple feature sizes on the same wafer, which would remove processing errors. Even better would be to print the multiple pitches during

the same exposure so both processing and dose variations are removed. Unfortunately, the F2X system created fields with too many nonuniformities to make these linewidth calculations. The variations originated from coherence effects, optic quality, and resist contrast. These measurements are being made in MET experiments.

Several different 10× optics have been used in this experiment with varying degrees of success. Because of the unusual pupil fill, figure aberrations do not significantly degrade the double-frequency imaging. However, localized, opaque multilayer coating defects present in some of the optics can modify one or both of the first order beams and significantly compromise the imaging. Experimental and simulated results in this chapter showed how coherent illumination exacerbates this problem. That being said, the 10×-Intel did perform well enough to allow Intel to do resist screening with this tool. During the peak of the resist screening period, 50-nm dense line and space patterns were printed with good reliability. Dose and focus repeatability was shown across many wafers in the numerous resists.

5.10 References

[1]   M. Shumway, S. Lee, C. Cho, P. Naulleau, K. Goldberg, and J. Bokor, "Extremely fine-pitch printing with a 10× Schwarzschild optic at extreme ultraviolet wavelengths," Proc. SPIE, Vol. 4343, 357-362 (2001).

[2]   P. Naulleau, "Aerial-image contrast measurement for the ETS Set-2 optic in the SES using the resist-clearing method," Berkeley Lab Materials Sciences Division Center for X-Ray Optics: Memo to File, January 30, 2002.

[3]   S. Lee and D. Tichenor, "Impact of finite resist resolution on aerial image contrast measurements," Intel Lithography Capital Equipment Development (LCED) Technical: Memo to Distribution, December 5, 2001.

[4]   Z. Fresco, I. Suez, S. Backer, and J. Fréchet, "AFM Induced Amine Deprotection: Triggering Localized Bond Cleavage by Application of Tip/Substrate Voltage Bias for the Surface Self-Assembly of Nanosized Dendritic Objects," J. Am. Chem. Soc., Vol. 126, 8374-5 (2004).

[5]   O. Wood, D. White et al., "Use of attenuated phase masks in extreme ultraviolet lithography", J. Vac. Sci. Technol. B, Vol. 15, No. 6, 2448 (1997).

[6]   J. Goldsmith, K. Berger, D. Bozman, G. Cardinale, D. Folk, C. Henderson, D. O'Connell, A. Ray-Chaudhuri, K. Stewart, D. Tichenor, H. Chapman, R. Gaughan, R. Hudyma, C. Montcalm, E. Spiller, J. Taylor, J. Williams, K. Goldberg, E. Gullikson, P. Naulleau, and J. Cobb, "Sub-100-nm lithographic imaging with an EUV 10X microstepper," Proc. SPIE, Vol. 3676, 264-271 (1999).

[7]   Data from Heidi Cao, Intel Corporation

[8]   Discussion with Patrick Naulleau, Lawrence Berkeley National Laboratory

[9]   S. Yasin, D. Hasko, and H. Ahmed, "Comparison of MIBK/IPA and water/IPA as PMMA developers for electron beam nanolithography," Microelectronic Engineering, Vol. 61-62, 745-753 (2002).

[10]   M. Khoury and D. Ferry, "Effect of molecular weight on poly(methyl methacrylate) resolution," J. Vac. Sci. Technol. B, Vol. 14, No. 1, 75-79 (Jan/Feb 1996).

[11]   E. Dobisz, S. Brandow, R. Bass, and J. Mitterender, "Effects of molecular properties on nanolithography in polymethyl methacrylate," J. Vac. Sci. Technol. B, Vol. 18, No. 1, 107-111 (Jan/Feb 2000).

[12]   M. Peuker, M. Lim, H. Smith, R. Morton, A. van Langen-Suurling, J. Romijn, E. van der Drift, and F. van Delft, "Hydrogen SilsesQuioxane, a high-resolution negative tone e-beam resist, investigated for its applicability in photon-based lithographies," Microelectronic Engineering, Vol. 61-62, 803-809 (2002).

[13]   O. Kishkovich and C. Larson, "Amine control for DUV lithography: identifying hidden sources," Proc. SPIE, Vol. 3999, 699-705 (2000.

[14]   J. Hoffnagle, W. Hinsberg, M. Sanchez, and F. Houle, "Method of measuring the spatial resolution of a photoresist," Optics Letters, Vol. 27, No.20, 1776-1778 (2002).

6   Aerial Image Contrast

6.1   Introduction

Line-edge roughness (LER) properties of a photoresist can be investigated by varying the aerial image contrast of exposure patterns. In a typical experiment, the aerial image contrast is varied in a known way, and then the resulting effects on LER are measured. This is commonly done through a two-exposure process (pattern exposure and background flood exposure) [1]. However, by using the aperture-plane filtering method developed in this chapter, it is possible to print multiple contrasts in single exposures. This is achieved by varying the duty cycle and line and space transmission levels of an object grating. Since this is a single exposure technique and no flood is needed, it can allow for more controlled contrast tests to help in the evaluation of resists.

6.2   Theory

This contrast variation method is essentially a two-beam interference technique. By tuning the relative strength of one of the beams against the other, it is possible to vary the contrast of the resulting image. Since line and space patterns in resists are the features of interest, it becomes advantageous to manipulate a simple object grating. By changing the duty cycle of a grating, the strength of the diffracted orders will vary. Printing this grating would also lead to the unwanted effect of producing different linewidths at different contrast levels. If, however, only the zero and one of the first orders are used to create the

114

field mismatch at the wafer, the linewidth variation will not appear. By correct filtering in the aperture plane (removing all but the 0 and +1 orders), the resists will only see variations in contrast and will not print the encoded duty cycles. The high-frequency duty cycle information becomes lost in the low-pass filter process.

6.2.1 Description

Three methods for varying aerial image contrast were studied that would help in the understanding of LER using the 10× system. The first was based on the conventional flood exposure technique where a flood field is added to the resist on which a pattern has already been exposed. The 10× system is not equipped to switch object masks during a wafer exposure and so a flood window can not be used.

One other possibility was to print the object mask so far out of focus that it was a blur on the wafer plane. If the blur was uniform enough it could act as a flood exposure. Figure 6-1 shows simulations where 50-nm patterns were printed out of focus near the image plane. As can be seen, the fields do not blur enough. This technique would have potential only if the illuminator was somehow made incoherent when doing an out-of-focus exposure. The 10× system is designed to only do coherent imaging experiments. As such, the out of focus image patterns contain coherent ringing and cannot act as a background flood. These simulations also show how lines and spaces are still printed even when out of focus. Each image in the figure is at the same scale as the others.
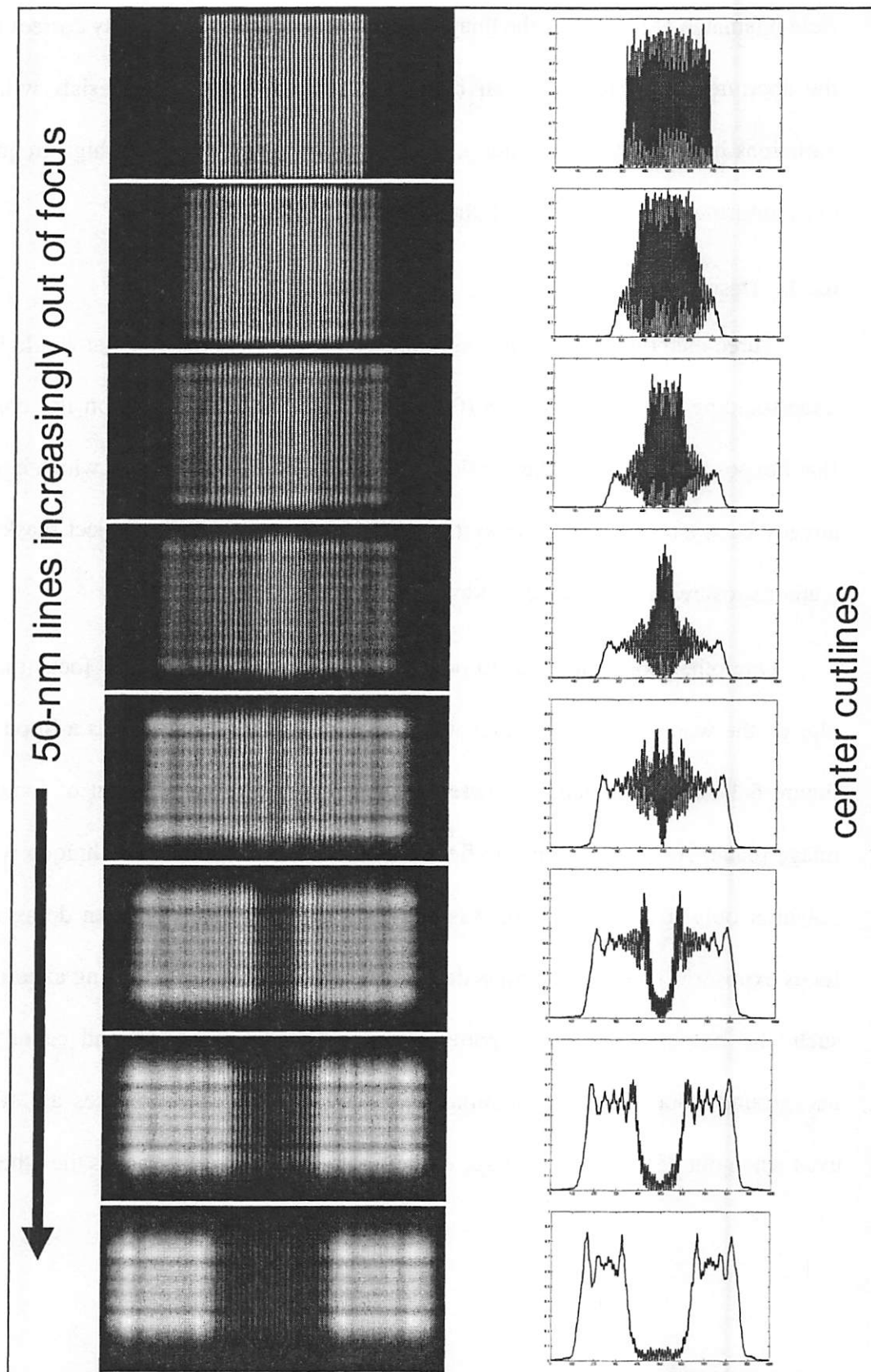
Figure 6-1: Focus run for 50-nm dense lines and spaces with center cutlines.

As mentioned in the introduction, another method to do aerial image contrast variation is through changing the duty cycle of a grating. In this process, only the zero and one of the first orders are used to create the necessary field mismatch. By filtering these gratings, the resists will only see variations in contrast and will not print the changing duty cycle. This idea has been taken a step further to the point where a grating has been designed that allows multiple contrasts to be printed during a single exposure. In brief, after choosing a dose level, one can vary the duty cycle and transmission of the grating in order to reach desired contrast levels.

It is important to note that this technique is different from the spatial-frequency doubling method (F2X) that has been used in the other chapters. In the F2X case, the zeroth order is blocked and the +1 and −1 orders are used to expose the resist creating an extra 2× demagnification of the object grating. Since the +1 and −1 orders are of equal strength the result is a high-contrast image. On the other hand, the contrast variation method uses the intentionally unbalanced field strengths of the 0 and +1 orders without any doubling.

6.2.2 Modeling

The duty cycle modulation for a transmission grating is illustrated in Figure 6-2.

t_A

d

1

0

$0 \leq d/P \leq 1$

$\cdots$

$\cdots$

P

ξ
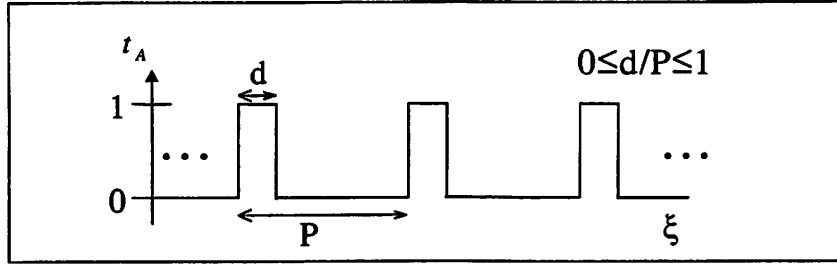
Figure 6-2: A simple amplitude transmission grating

Using Goodman's notation [3], the transmission function can be written as

$$t_A(\xi) = rect(\frac{\xi}{d}),$$

(Eq. 6-1)

and the diffraction coefficient for the Kth order is given as

$$c_K = \frac{1}{P} \cdot FT\{t_A(\xi)\} \rightarrow f_x = \frac{K}{P}.$$

(Eq. 6-2)

This leads to the result that

$$c_K = \frac{d}{P} \cdot sinc(\frac{d}{P}K).$$

(Eq. 6-3)

Where

$$sinc(x) = \frac{\sin(\pi x)}{\pi x}.$$

(Eq. 6-4)

For a 50-50 duty cycle grating, $\frac{d}{P} = \frac{1}{2}$ which leads to the common intensity diffraction

efficiencies $(|c_K|^2)$: $|c_0|^2 = 25\%$, and $|c_1|^2 = \frac{1}{\pi^2} \approx 10\%$.

By varying the duty cycle, the strength in the zero and first orders will be modified

to create a change in contrast. If one also wants to tune the dose required to print these

contrasts then another variable is needed.

To print features at the same dose, the somewhat more generalized transmission

grating is introduced as shown in Figure 6-3.
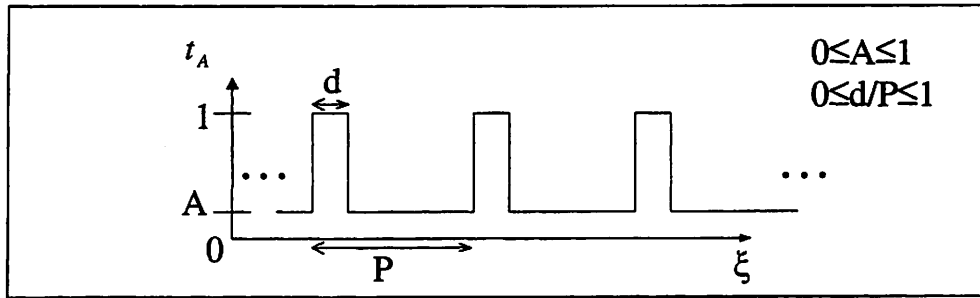
Figure 6-3: A more general amplitude transmission grating

The transmission function follows as

$$t_A(\xi) = A \cdot rect(\frac{\xi}{P}) + (1-A) \cdot rect(\frac{\xi}{d}).$$

(Eq. 6-5)

Which will yield diffraction coefficients of the form

$$c_K = A \cdot sinc(K) + (1-A) \cdot \frac{d}{P} \cdot sinc(K\frac{d}{P}).$$

(Eq. 6-6)

Therefore, the field strengths for the zero and first orders are

$$c_0 = A + (1-A) \cdot \frac{d}{P}$$

(Eq. 6-7)

and

$$c_1 = (1 - A) \cdot \frac{d}{P} \cdot sinc(\frac{d}{P}) .$$

(Eq. 6-8)

One can then define the intensity maximum and minimum based on the field strengths:

$$I_{max} = |c_0 + c_1|^2$$

(Eq. 6-9)

$$I_{min} = |c_0 - c_1|^2 .$$

(Eq. 6-10)

The contrast, C, can then be calculated using the equation

$$C = \frac{I_{max} - I_{min}}{I_{max} + I_{min}} .$$

(Eq. 6-11)

The relative dose, D, defines the midpoint of the intensity variation:

$$D = \frac{1}{2}(I_{max} + I_{min}).$$

(Eq. 6-12)

In summary, this provides contrast, C, and dose, D, as functions of A and the ratio d/P. With these equations one can calculate the contrast and dose values achieved from a specific duty cycle (d/P) and dark area transmission percentage (A). Alternatively, after choosing desired dose and contrast levels, suitable grating parameters (d/P and A) can be calculated.

The graphs in Figures 6-4 and 6-5 show some of the results from these duty cycle calculations. The x-axis represents the amount of 100% transmission (open area) that is contained in a single pitch of the grating (ratio d/P from Figure 6-3). The three separate

curves represent values for the amount of light that is transmitted in the "dark" region of the grating (variable A). It is evident from Figures 6-4 and 6-5 that as more light is allowed through the "dark" region, the zeroth order field strength increases since more light simply passes through the mask. The most diffraction into the first order occurs at d/P=0.5 (a 1:1 grating). As d/P varies from this value the field strength decreases. The grating becomes less efficient for diffracting light into the first order.

Zeroth Order Field Strength

Figure 6-4: Zeroth order field strength as a function of d/P

First Order Field Strength
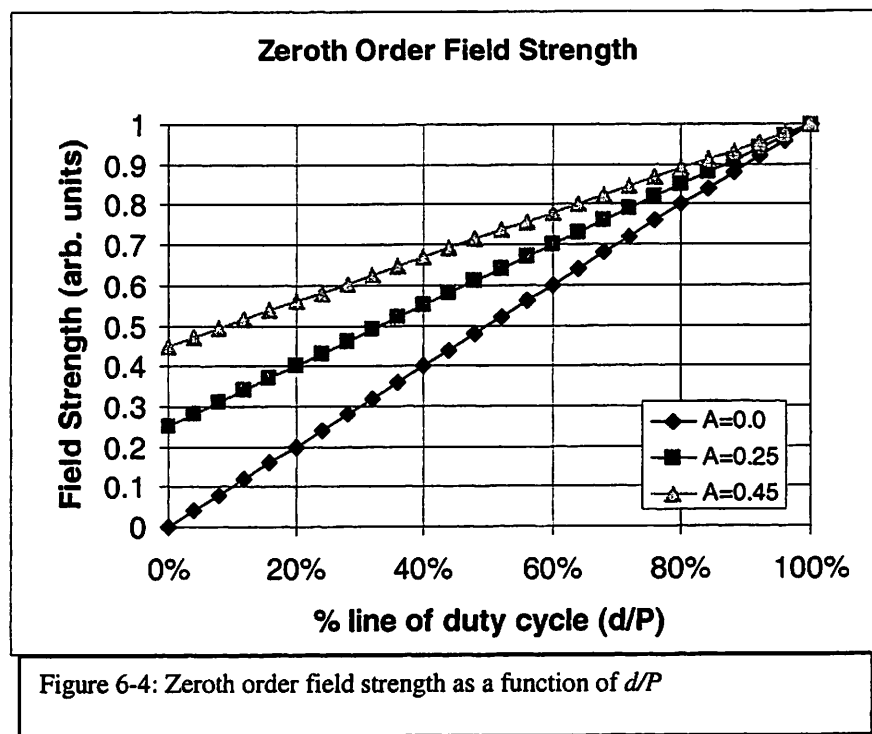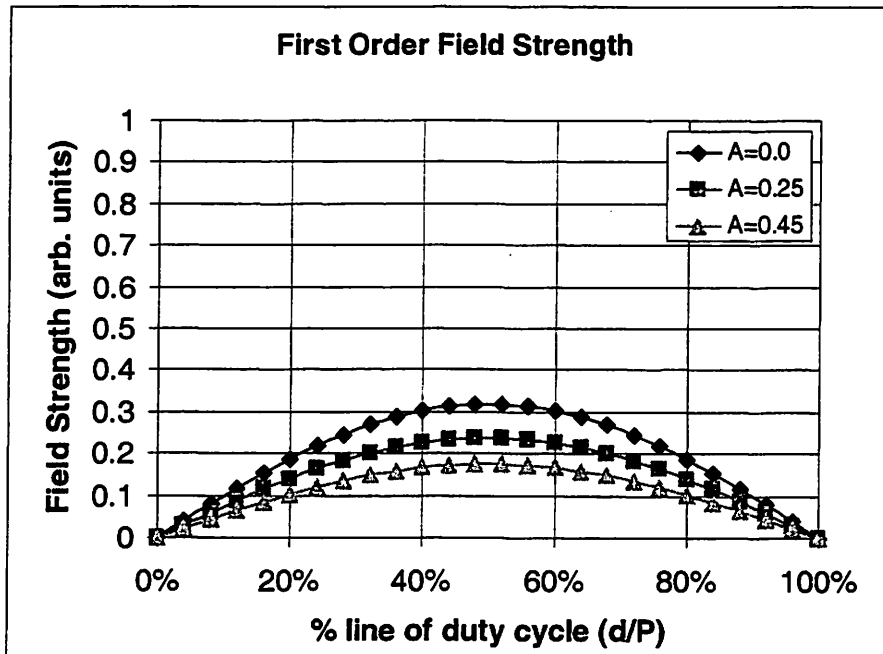
Figure 6-5: First order field strength as a function of d/P

Contrast and dose plots are shown in Figures 6-6 and 6-7 respectively. These two plots also show data as d/P is varied. For most choices of A, it is possible to achieve a certain contrast level at two values of d/P. Dose is always increasing with increasing d/P since less light is being attenuated by the grating. It is a simple extension in Figure 6-8 to plot contrast and dose against each other for every value of d/P.
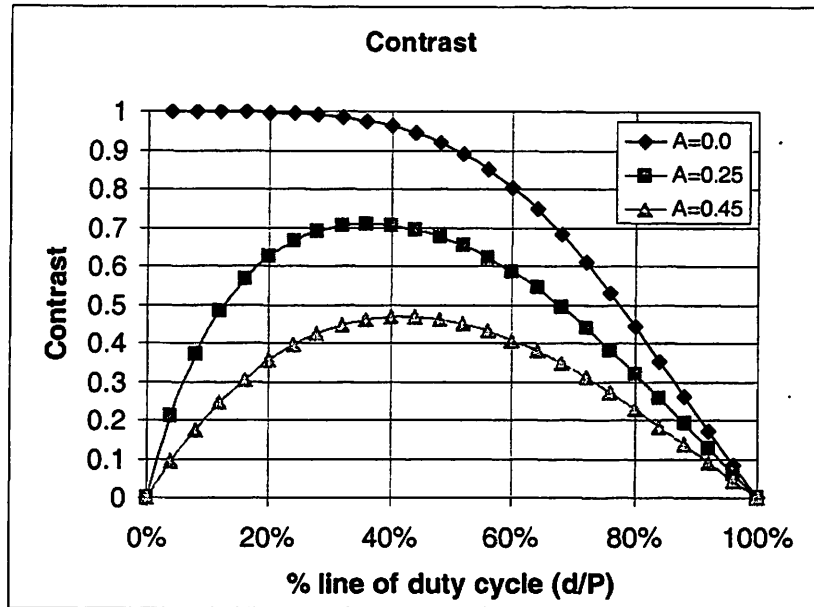
Figure 6-6: Contrast as a function of *d/P*
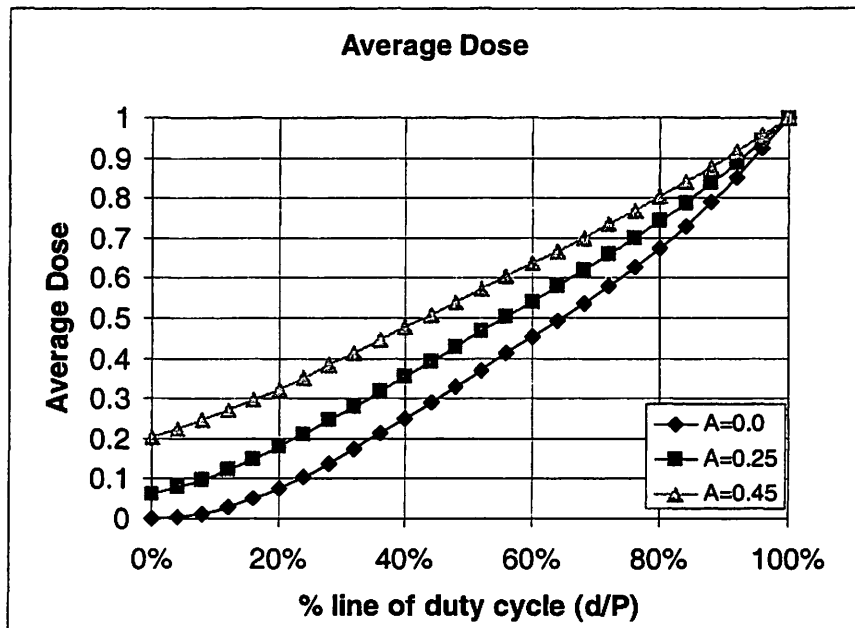
Figure 6-7: Average dose as a function of *d/P*

Dose-Contrast relationship for each d/P ratio

Legend:
- A=0.0
- A=0.25
- A=0.45

Y-axis: Contrast
X-axis: Average Dose

Figure 6-8: Dose vs. contrast for each *d/P* value
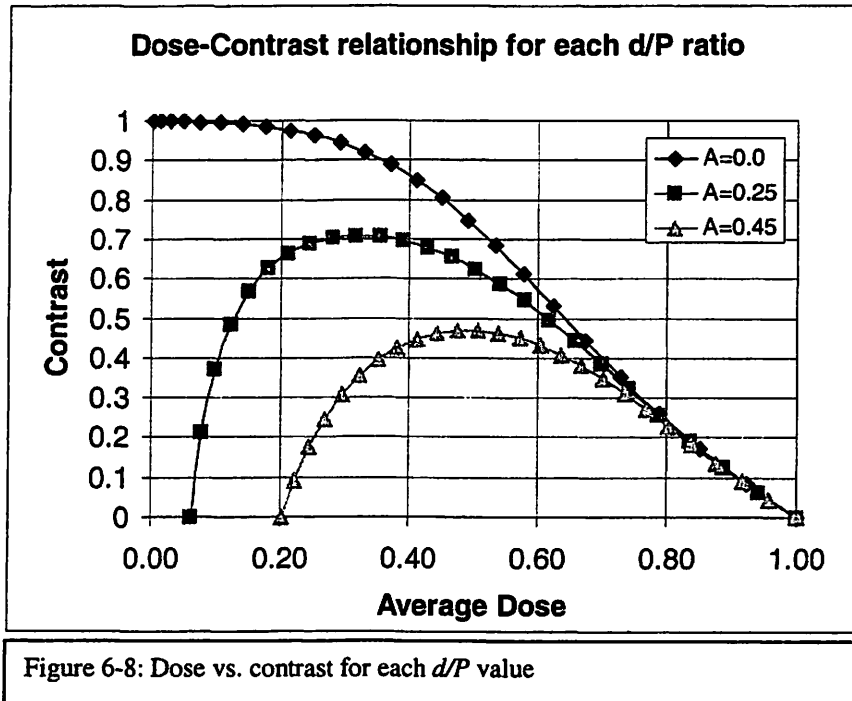
When creating an object grating, things can be kept simple by keeping *A* fixed. Then through Figure 6-6, one can pick contrast levels by careful choice of the grating's duty cycle. By simply having different duty cycles on an object various contrasts can be printed. It will, however, take separate exposures to print at each correct dose. What has been shown here is that by taking the duty-cycle-variation process a step further, multiple contrasts can be printed during a single exposure.

In summary, after choosing a dose level, one can vary the duty cycle and transmission of the grating to reach desired contrast levels. See Figure 6-9 for a simulated grating that would produce contrast levels of 20, 30, 40 and 50% in a single exposure.
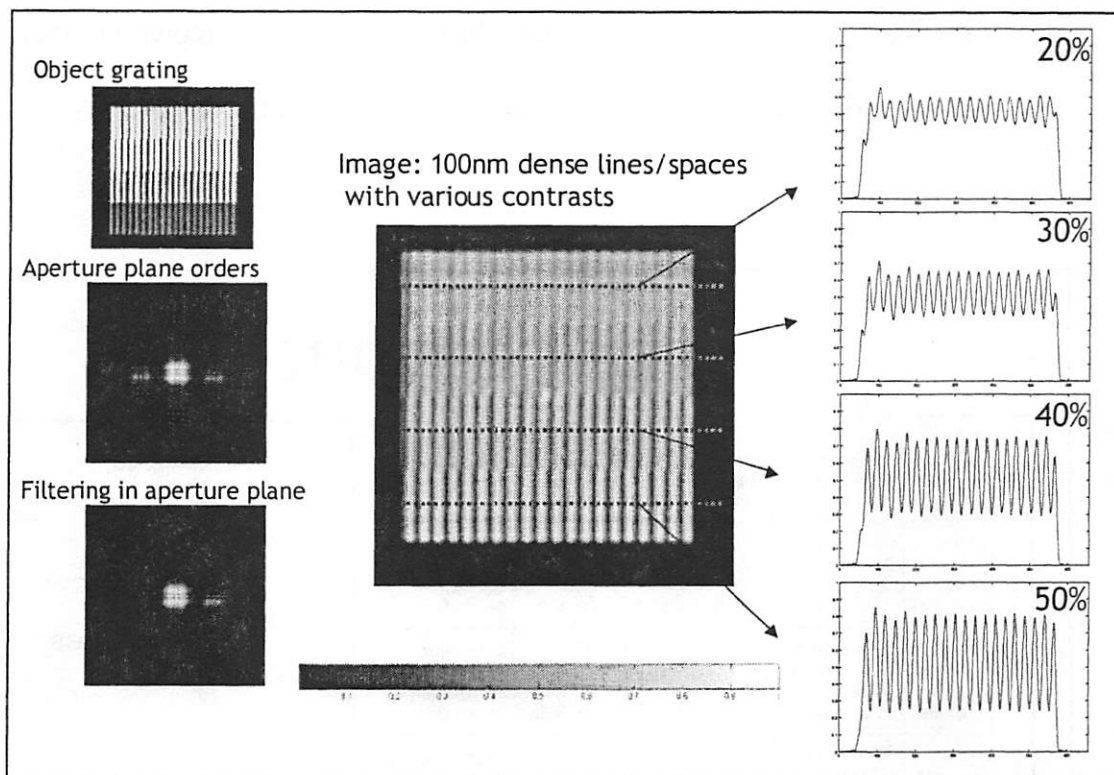
Figure 6-9: Example of using duty cycle tuning to print four contrast levels in a single exposure

6.3 Contrast Experiments

Contrast-variation imaging experiments used the Micro Exposure Tool (MET) at the Advanced Light Source (see Section3.3). Built-up from the theory and simulations in Section 6.2, these experiments used the two-order contrast variation method. They incorporated duty-cycle modulations on the object mask and used the MET's NA limits to filter out unwanted orders.

6.3.1 Micro Exposure Tool (MET) Setup

The reflection mask for the MET was designed to print both 50- and 30-nm dense line and space patterns. It was written with the Nanowriter at Lawrence Berkeley National Laboratory. Contrast levels ranged from 90% to 30% for each of the two pitches. Figure

6-10 shows the layout for the experiment. In the Figure, open represents transmission width (d) and closed represents the absorbed width on the multilayer (P-d).

Mask Layout

50-nm lines 91% contrast .25µm open .25µm closed	50-nm lines 80% contrast .3µm open .2µm closed	50-nm lines 70% contrast .335µm open .165µm closed	50-nm lines 51% contrast .385µm open .115µm closed	50-nm lines 31% contrast .43µm open .07µm closed	
50-nm lines 65% contrast .35µm open .15µm closed	50-nm lines 60% contrast .365µm open .135µm closed	50-nm lines 55% contrast .375µm open .125µm closed	50-nm lines 45% contrast .4µm open .1µm closed	50-nm lines 40% contrast .41µm open .09µm closed	
30-nm lines 91% contrast .15µm open .15µm closed	30-nm lines 80% contrast .18µm open .12µm closed	30-nm lines 70% contrast .201µm open .099µm closed	30-nm lines 51% contrast .231µm open .069µm closed	30-nm lines 31% contrast .258µm open .042µm closed	Zone Plates
30-nm lines 65% contrast .21µm open .09µm closed	30-nm lines 60% contrast .219µm open .081µm closed	30-nm lines 55% contrast .225µm open .075µm closed	30-nm lines 45% contrast .24µm open .06µm closed	30-nm lines 40% contrast .246µm open .054µm closed	

100µm x 100 µm fields in each square above

Figure 6-10: Mask layout for contrast variation experiments with the MET (a 5× demagnification tool). A zone plate array shared this area on the mask. 100-µm square fields were in each window.

Coherence was set at 0.1 using the MET's rotational illumination mirrors. Shipley 1K was the chosen resist based on its superior performance in the 10×-Intel system (Section 5.3). Etch bias during mask fabrication created the actual contrasts as shown in Figure 6-11. The actual contrasts differed by 7% at most still giving a good range of image contrasts to print.

Programmed Contrast (%)	Actual Contrast (%)
91	86.4
80	75.0
70	65.5
65	60.3
60	56.6
55	52.6
51	50.4
45	46.8
40	43.3
31	37.8

Figure 6-11: Etch bias during mask fabrication produced linewidths that adjusted the final contrast levels. The left shows the layout values and the right are based on SEM images of the real mask.

6.3.2 Line Edge Roughness (LER) Results

A field from the contrast exposures is shown in Figure 6-12. The twenty contrast fields defined in Figure 6-10 are on the left of the image. There are two zone plates on the right side. Each of the contrast fields is 20 μm square. The shading of the different square fields is due to the fact that only certain contrasts are at the correct dose for printing in this example image.
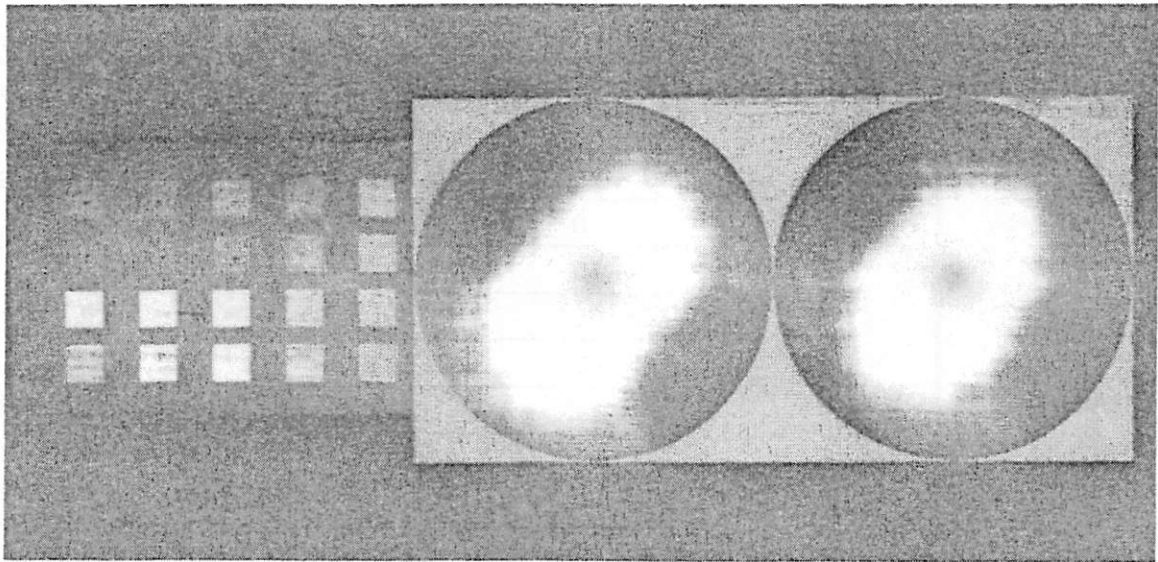
Figure 6-12: Contrast exposure in Shipley 1K resist. The contrast fields are on the left and the zone plates are on the right. Each contrast field is 20 µm × 20 µm.

Figure 6-13 shows the highest contrast (86.4% actual mask contrast) results for the 50-nm lines and spaces. The software program used to do the roughness analysis was SuMMIT [3]. The lowest two contrast levels (43.3% and 37.8%) did not print linewidths close enough to the optimum 50 nm. Contrast exposures from the 37.8% field only printed down to 80-nm features. Similarly, the 43.3% contrast field printed lines to 70 nm. Both line-edge roughness (LER) and line-width roughness (LWR) measurements were taken for the remaining eight contrast points. All linewidths fell between 45- and 55-nm. Line-width roughness is similar to LER except that it looks at variation with respect to the width of the line rather than the sides. It is believed to be a better metric when determining transistor performance and current leakage [4].
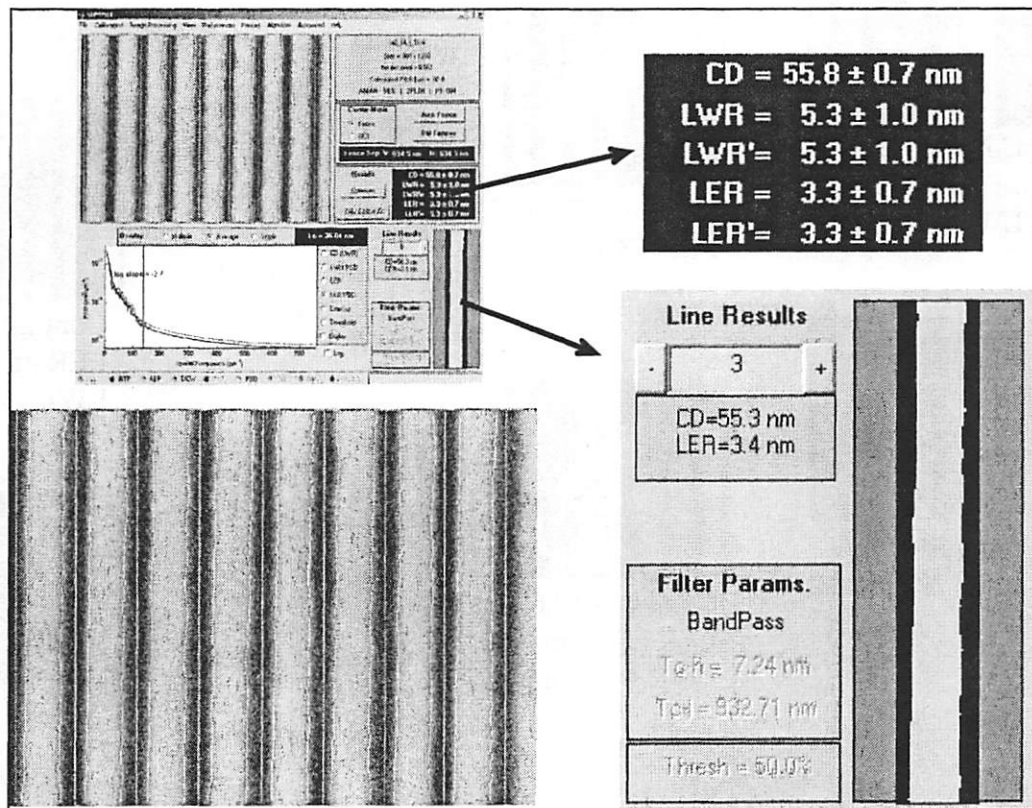
Figure 6-13: SuMMIT screen captures for the 50-nm highest contrast case (86.4%). These lines are slightly underdosed at 55.8 nm. LER = 3.3 nm; LWR = 5.3 nm.

Figure 6-14 shows the eight contrast steps with their corresponding SuMMIT data values. Analysis of this 50-nm data shows a definite trend - a decrease in contrast will contribute to an increase in line edge roughness and a measurable increase in line width roughness.

Contrast - 86.4%
LER - 3.3 nm
LWR - 5.3 nm

Contrast - 75%
LER - 3.7 nm
LWR - 5.7 nm

Contrast - 65.5%
LER - 5.1 nm
LWR - 8.1 nm

Contrast - 60.3%
LER - 5.7 nm
LWR - 7.5 nm

Contrast - 56.6%
LER - 6.4 nm
LWR - 10.4 nm

Contrast - 52.6%
LER - 6.3 nm
LWR - 10.0 nm

Contrast - 50.4%
LER - 6.8 nm
LWR - 10.27 nm

Contrast - 46.8%
LER - 8.0 nm
LWR - 12.84 nm
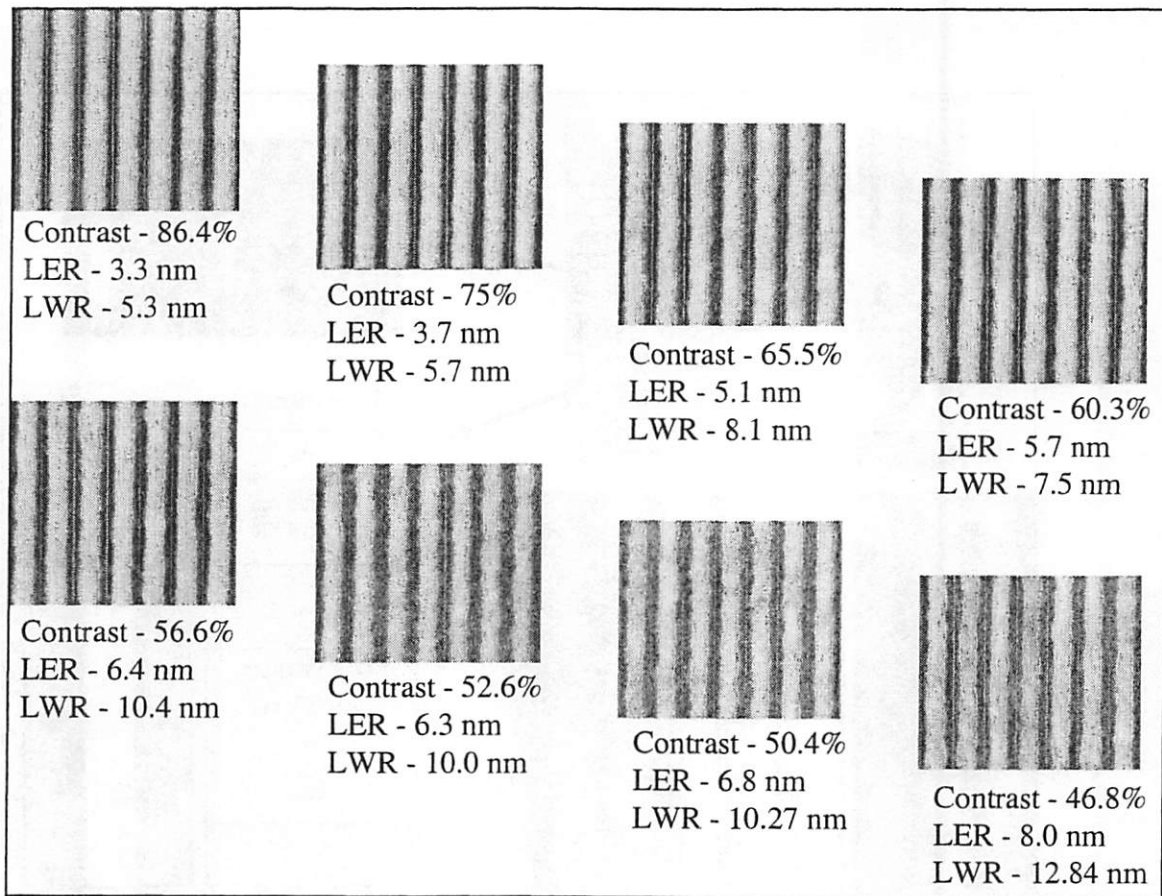
Figure 6-14: Contrast variation for dense 50-nm lines and spaces in Shipley 1K.

This LER and LWR data is also plotted in Figure 6-15. Both LER and LWR follow similar upward trends toward more roughness as contrast is decreased. Figure 6-16 plots LER against LWR. A linear fit is shown for this data. In these experiments, Shipley 1K shows LWR to be, on average, 1.6 times larger than LER. If line edge roughness of the left and right sides were to vary randomly and independently of each other, then LWR = $\sqrt{2} \times$ LER [4]. The results for the MET contrast exposures come close to this relationship.

130
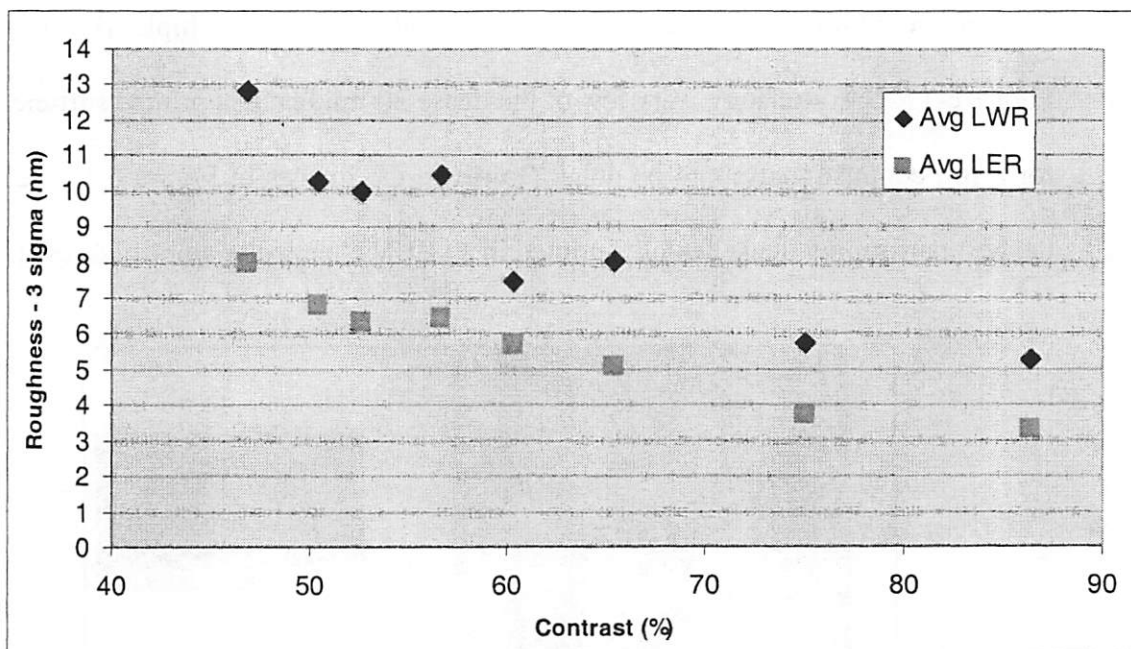
Figure 6-15: Roughness seen in Shipley 1K resist for dense 50-nm lines as a function of contrast.
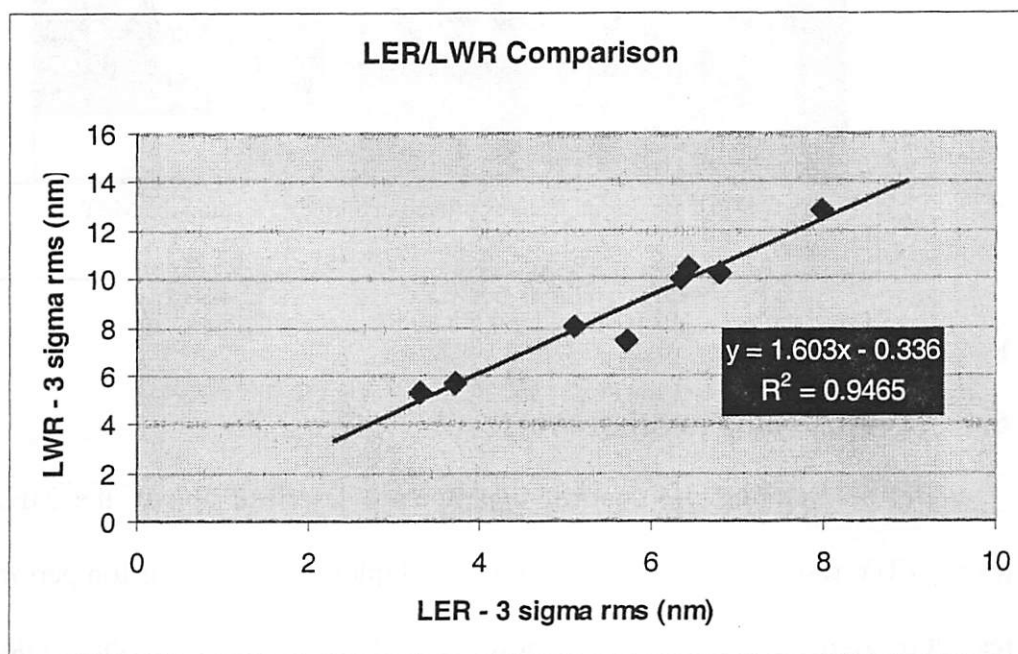
Figure 6-16: LER/LWR comparison using data from Figure-6-15. The equation for the linear best-fit is shown in the black square.

Some 30-nm dense lines and spaces were also printed in Shipley 1K as shown in Figure 6-17. Unfortunately, very few of the dense 30-nm features printed sufficiently well for a full contrast analysis to be done. However, the images in Figure 6-17 are some of the best performing dense features printed in an EUV chemically amplified resist.

CD = 30.3 ± 1.6 nm
LWR = 11.3 ± 2.8 nm
LWR'= 11.3 ± 2.8 nm
LER = 5.6 ± 1.2 nm
LER'= 5.6 ± 1.2 nm

CD = 32.5 ± 1.2 nm
LWR = 10.9 ± 2.8 nm
LWR'= 10.9 ± 2.8 nm
LER = 6.4 ± 1.5 nm
LER'= 6.3 ± 1.5 nm

Figure 6-17: Dense 30-nm features printed in Shipley 1K using the MET.
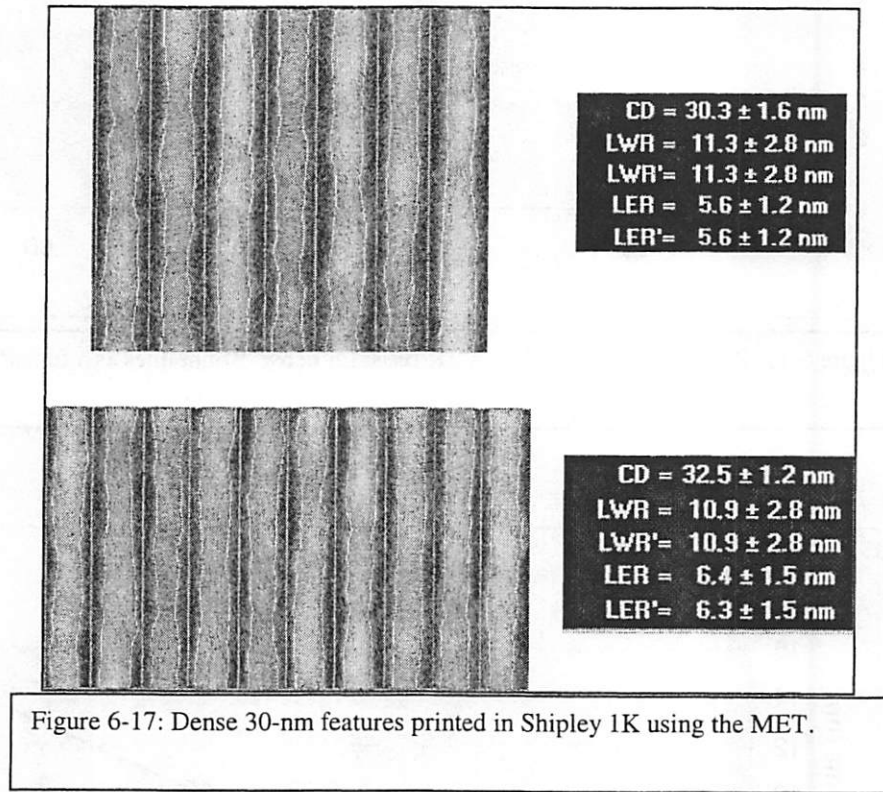
6.4 Comparisons to other work

Besides running the contrast experiments described above, the MET has been testing EUV resists. The tool has also found Shipley 1K to be their top performer from a resolution standpoint. Figure 6-18 shows what the MET has been able to do in Shipley 1K [5]. As can be seen in the lower right, 25-nm dense features are not fully resolving.

The 30-nm lines in the bottom center look similar to the ones from the contrast variation experiments above (Figure 6-17).
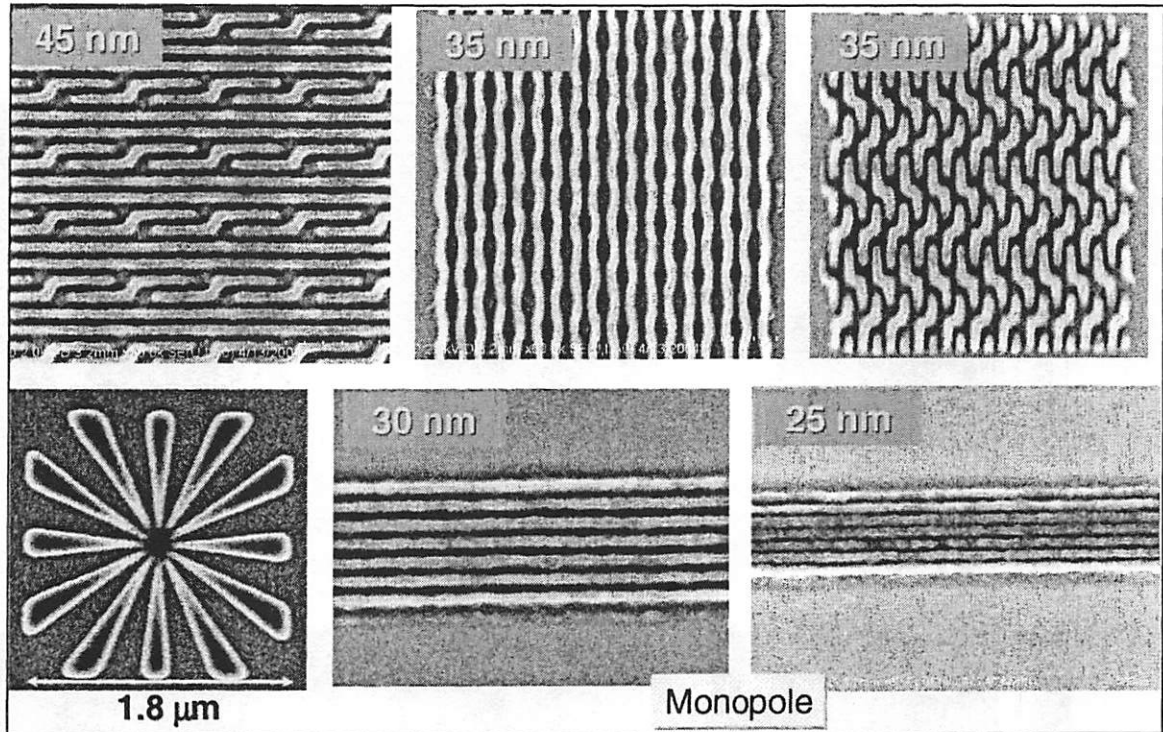
Figure 6-18: Shipley 1K resist images printed with the MET. [5]

Another important comparison to be made is the LER values for Shipley 1K in both the 10×-Intel and the MET systems. The 10×-Intel imaged Shipley 1K using the high-contrast F2X experiment (Section 5.3). The LER seen for those features should be similar to the LER measurements made at high contrast (86%) using the MET. Figure 6-19 shows SEM pictures of Shipley 1K from 10×-Intel exposures. Below the images are the SuMMIT data. These linewidths are all around 50 nm so are directly comparable to what was shown in Figure 6-13. With the 10×-Intel, 50-nm lines and spaces produce LER values between 3.3 and 4 nm. This agrees well with the 3.3 nm LER value for the high-

contrast (86.4%) MET exposures. It is important to note that all these measurements were

made using the same software and the same scanning electron microscope.

CD – 47 nm
LER – 3.3 nm
LWR – 5.9 nm

CD – 49.2 nm
LER – 3.3 nm
LWR – 3.9 nm

CD – 45.8 nm
LER – 3.5 nm
LWR – 5.8 nm

CD – 42.7 nm
LER – 3.7 nm
LWR – 6.9 nm

CD – 49.3 nm
LER – 4.0 nm
LWR – 6.2 nm
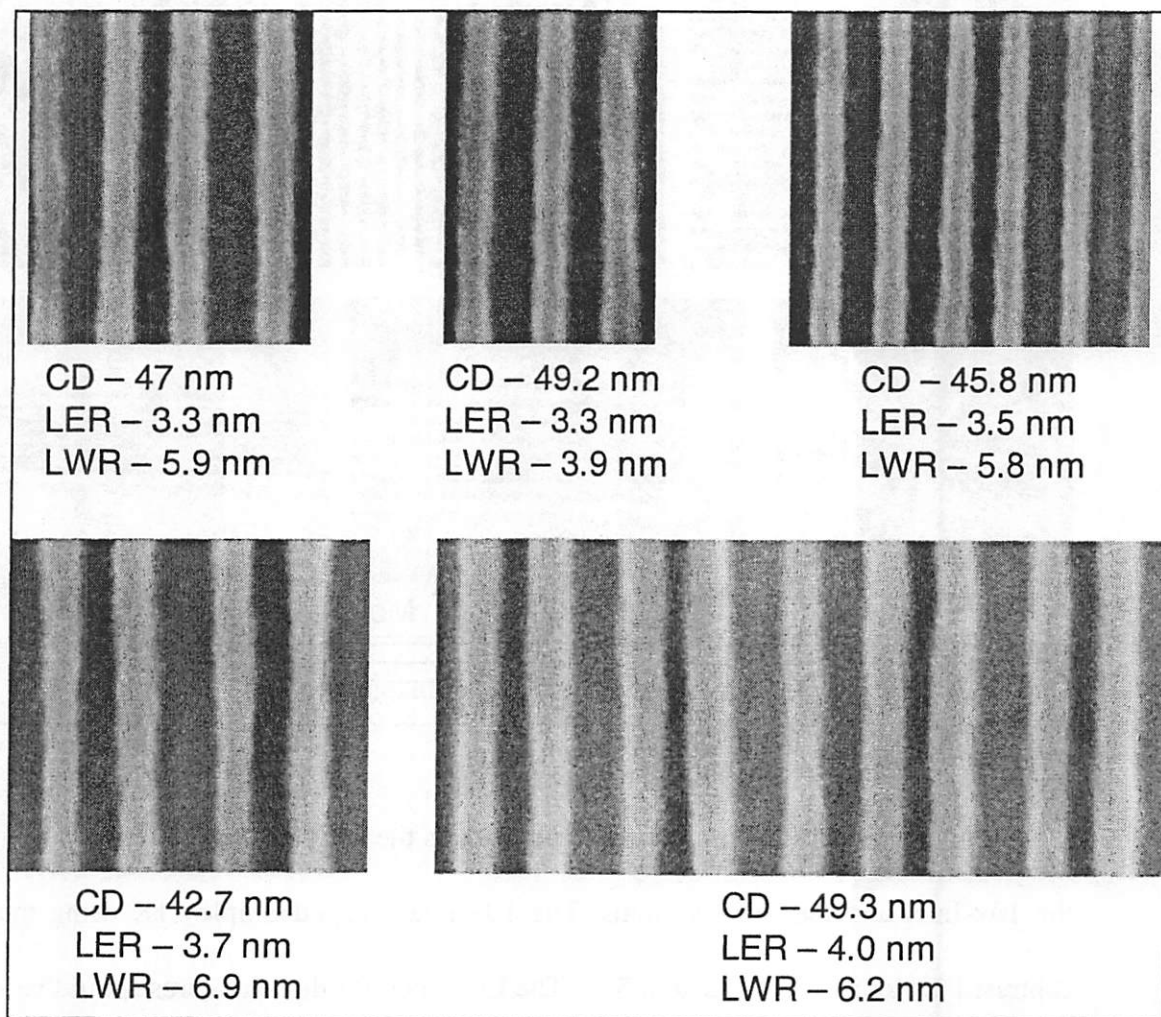
Figure 6-19: 50-nm dense features printed in Shipley 1K with 10×-Intel. The high-contrast F2X technique was used.

The data in Figure 6-19 can be added to the LER/LWR comparison plot (Figure 6-16). This new analysis is shown in Figure 6-20.
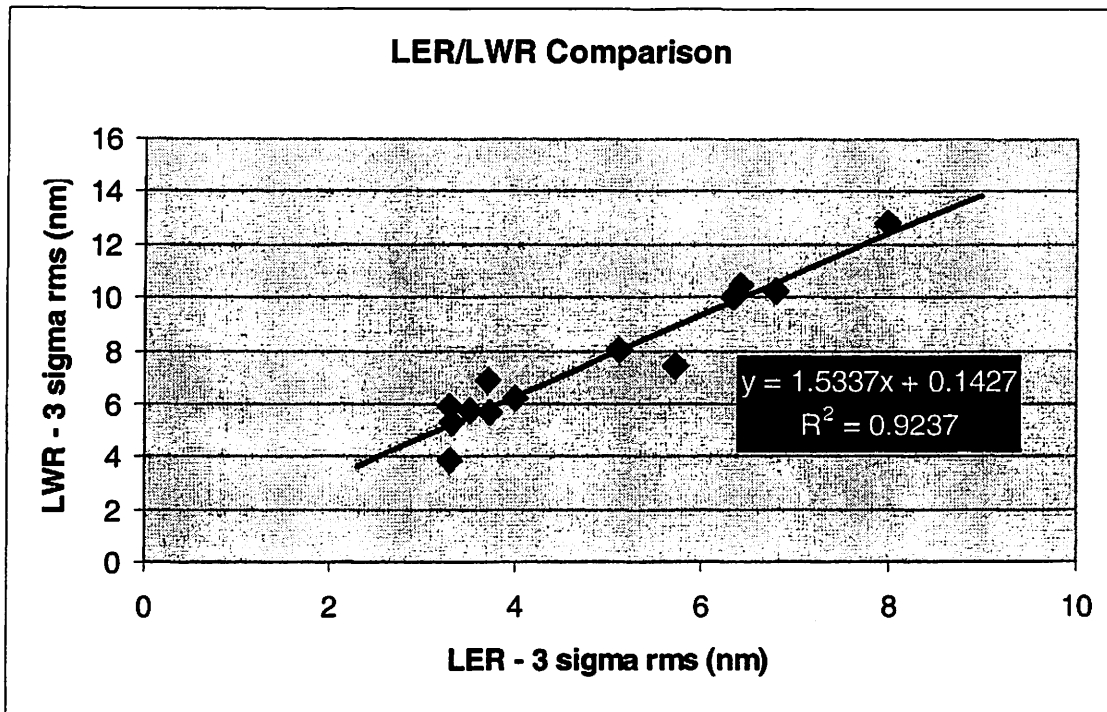
Figure 6-20: LER and LWR values for Shipley 1K using both the 10x-Intel and MET exposures (from Figures 6-14 and 6-19).

Other research groups have shown similar trends in regards to LER (higher contrast images produces lower LER). IBM has done work at 250 nm lines and spaces [1]. Mike Williamson did work at UC Berkeley also with 250 nm features [6]. A detailed look at features around 100 nm was done by AMD [7]. This work showed better agreement between LER and image-log-slope (ILS) than between LER and contrast. It was shown that variations in feature type and illumination would make contrast a weaker predictor of LER than using ILS. Since the MET contrast exposures in this thesis were done at 50 nm, the ILS values are larger than those for AMD's data. For completeness, Figure 6-21 shows the MET roughness data plotted for their ILS values.
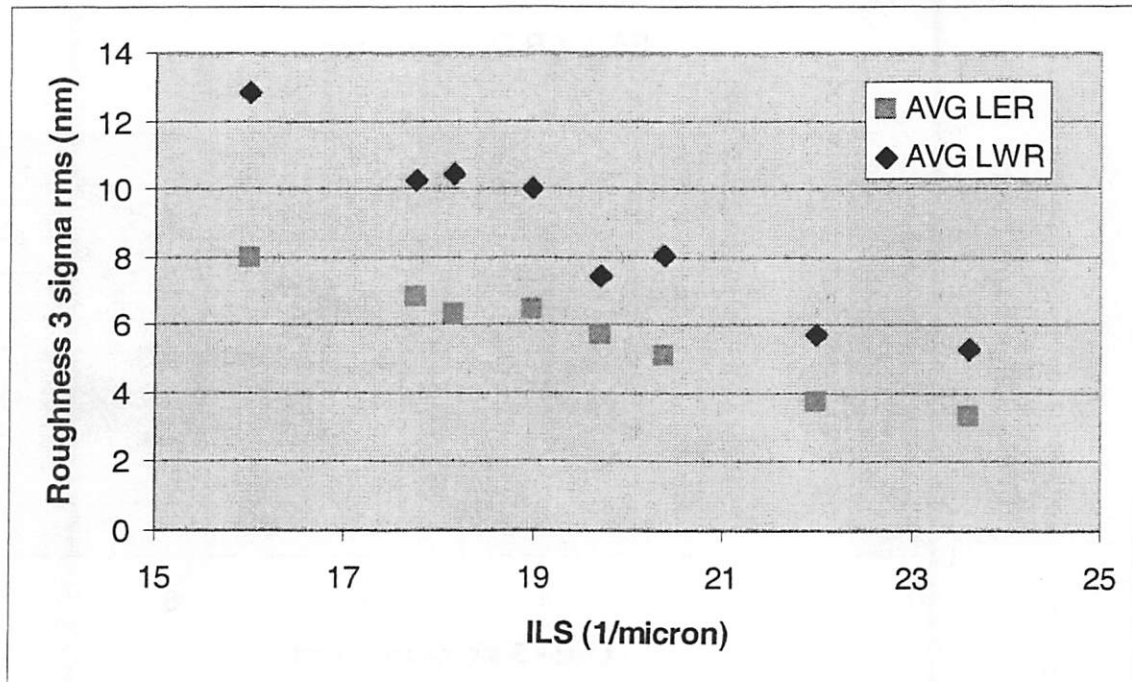
Figure 6-21: Image-log-slope (ILS) data in Shipley 1K resist using the MET. (roughness values from Figure 6-14).

6.5 Extension: Directional Contrast

An interesting extension to this aerial image contrast work is to look at using a phase mask. Previously in Section 6.2, the duty cycle and absorption strength were the only allowed variables. However, if phase is added as a mask fabrication possibility, new contrast designs can be created. In fact, if a multiple-phase mask was used then the contrast technique could work in a conventional stepper where spatial filtering in the aperture plane is not usually feasible.

The main concept is to fuse the single-exposure contrast technique described in Section 6.2 with a modified linear phase grating (LPG). This idea originated from a

136

conversation with Greg McIntyre of UC Berkeley. He was starting to use phase masks as illumination detectors [8]. Figure 6-22 shows an example of a linear phase grating. The incident light entering the grating from the top is redirected into the +1 order. No light is directed in the 0 or -1 orders.

Incident light

4 Phase grating

Illumination directed off-axis

-1 = 0   +1 = 1
0 = 0
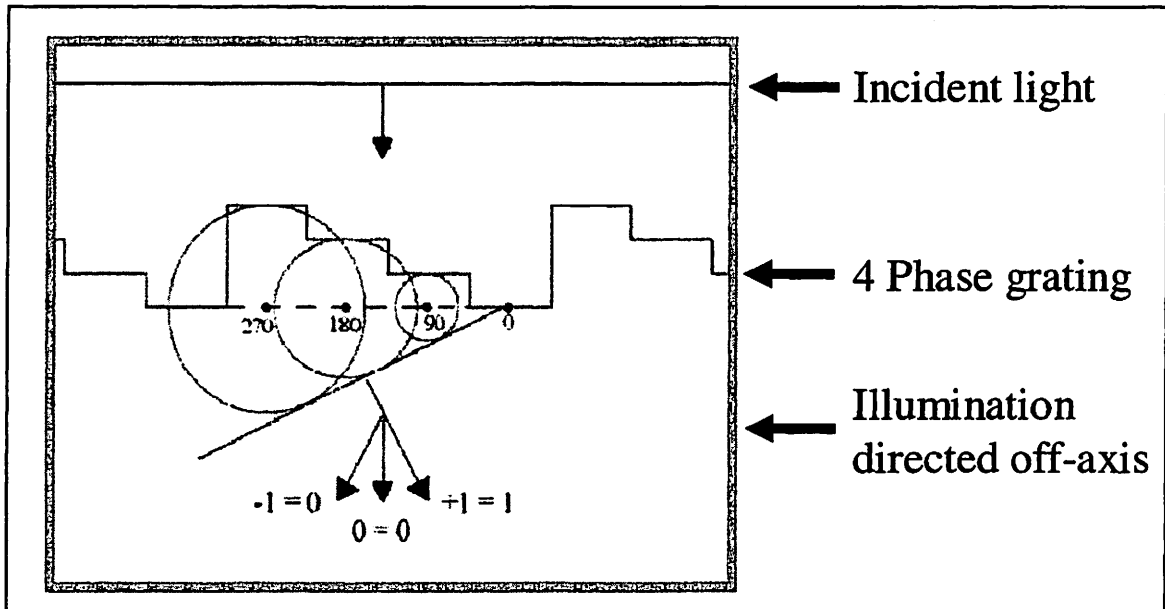
Figure 6-22: Diffracted orders from a linear phase grating. Light is directed into the +1 and higher orders. [modified image from reference 8]

By using phase manipulation to remove these low orders, no aperture filtering is needed. As such, without filtering at all, only select pitches would be available for any individual imaging system. With the 0th order being directed off toward the edge of the pupil, manipulation of the phase mask can vary the contrast. By simply varying the transmission amounts through the four different phase levels (0°, 90°, 180°, and 270°), the diffracted fields will no longer completely cancel out the 0th order. To get strong contrast manipulation it is useful to change the transmission amounts of two adjacent phase levels. For example, reducing the amount of incident light transmitted through the

137

0° and 90° levels by 50% and letting 100% of the 180° and 270° light through the system will reduce the image contrast by 48%. A whole range of such transmission levels are shown in Figure 6-23. These simulations show from left to right:

1) transmission amounts for each phase level in the grating
2) the diffracted orders in the pupil plane
3) line and space fields after re-imaging the absorptive phase grating
4) center cutlines through each of the image fields in 3)

In the first case, all phase levels are completely transmitting and the contrast is essentially zero. This is because the +1 order is being interfered with by no other orders. Once a second order gains some strength (as in any of the other cases) then there will be at least some modulation of the image field. These simulations were done using spherical illumination of the phase mask, but plane wave illumination would work as well.

Transmission Levels		Diffracted Orders	Image Fields	Cutlines
0°	100%			~0%
90°	100%			
180°	100%			
270°	100%			
0°	90%			9%
90°	90%			
180°	100%			
270°	100%			
0°	70%			27%
90°	70%			
180°	100%			
270°	100%			
0°	50%			48%
90°	50%			
180°	100%			
270°	100%			
0°	30%			71%
90°	30%			
180°	100%			
270°	100%			
0°	10%			90%
90°	10%			
180°	100%			
270°	100%			
0°	0%			96%
90°	0%			
180°	100%			
270°	100%			
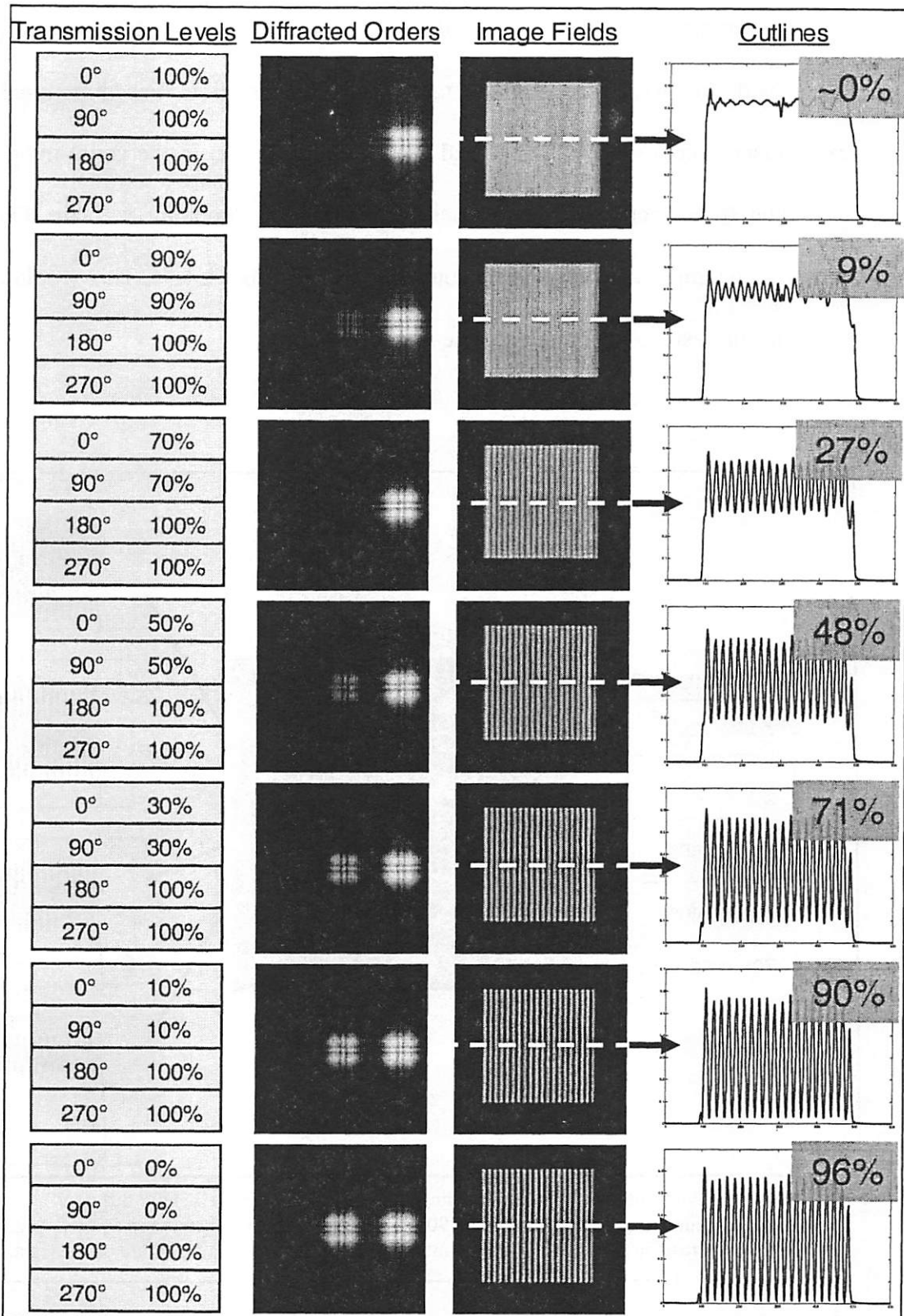
Figure 6-23: Simulations on contrast variation using an absorptive phase mask. As less light is allowed through the 0° and 90° phase levels, the image gains contrast.

In a typical phase mask there already is some attenuation difference in the phase levels and this would need to be taken into consideration. For directional contrast experiments, more emphasis is placed on absorption levels. In the aerial image contrast technique from Section 6.2, duty cycle was the more important variable. Figure 6-24 shows an example of a mask with four different absorber levels. This would allow for multiple contrasts to be printed as dose is varied.
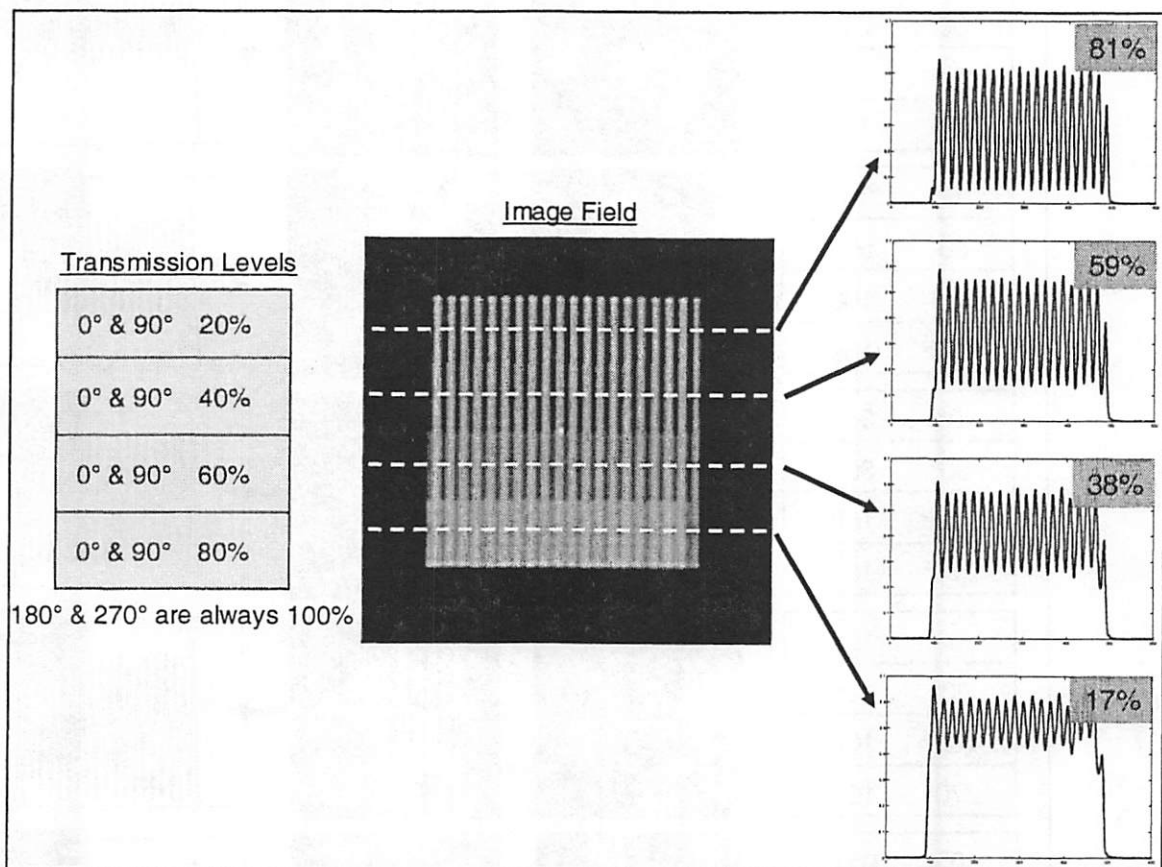

Figure 6-24: Multiple-contrast imaging using an absorptive phase mask. Four different transmission amounts are used for 0° and 90° phase levels. These transmission amounts produce different contrasts in the image field. Cutlines for each transmission amount are on the right.

6.6 Conclusion

In regards to contrast modulation, it is relatively easy to make a mask that prints different contrast levels at different dose levels. We have shown that experimentally in this chapter. It only requires varying the duty cycle and filtering everything but the 0 and +1 orders.

In order to balance the dose levels, however, an additional parameter needs to be added in the mask design where some light is allowed through the "dark" regions of the grating. This essentially creates a background that evens out the various patterns. After fixing the dose level, one can vary the duty cycle and dark area transmission of the grating to reach a desired contrast level.

The fabrication of such a mask, however, would be difficult. Rather than changing absorber thicknesses in the "dark" regions it would be simpler to pattern sub-resolution features with an e-beam writer. These sub-resolution features would act as absorbers depending on their surface densities. A four-contrast mask would require four separate duty cycles and four different absorber levels. Similarly, creation of a four-phase/four-absorber mask to do directional contrast variation would also be a difficult mask to fabricate.

Line-edge roughness properties of Shipley's 1K resist were investigated by varying the aerial image contrast of a dense line and space pattern. This aerial image contrast technique was developed from simple diffraction theory. After the closed-form equations were solved, simulations were done in MATLAB. When the simulations confirmed the contrast variation methodology, a mask was fabricated for experiments using the MET.

Results show that an increase in the aerial image contrast causes a subsequent decrease in the line edge roughness (LER). Similar effects are seen for line width roughness (LWR). Averaged over the data, LWR was 1.5 times larger than LER. The lowest LER seen for dense 50-nm lines and spaces in Shipley 1K was 3.3 nm rms (3 sigma). This was in the highest contrast case (86.4%). As contrast decreased to 46.8%, LER grew to 8.0 nm rms (3 sigma). The highest contrast case, using these MET exposures, produced the same LER in Shipley 1K (3.3 nm rms) as was seen in the high-contrast F2X system.

Other studies have shown similar trends with regards to line roughness for many different resists. Line roughness is certainly not solely caused by low image contrast, but tools like this contrast variation technique can be used to effectively monitor resist performance. The work in this thesis has shown contrast experiments using the smallest linewidths to date.

6.7 References

[1]   M. I. Sanchez, W. D. Hinsberg, F. A. Houle, J. A. Hoffnagle, H. Iyo, and C. Nguyen, "Aerial Image Contrast Using Interferometric Lithography: Effect on Line-Edge Roughness," Proc. SPIE, Vol. 3678, 160-71 (1999).

[2]   J. W. Goodman, Introduction to Fourier Optics, McGraw-Hill, New York, 1996.

[3]   SuMMIT software developed by Patrick Naulleau. http://euvl.com/summit/

[4]   H. Cao, J. Roberts, J. Dalin, M. Chandhok, R. Meagley, E. Panning, M. Shell, and B. Rice, "Intel's EUV resist development," Proc. SPIE, Vol. 5039, 484-491 (2003).

[5]   Patrick Naulleau data slide, Lawrence Berkeley National Laboratory

[6]   M. Williamson and A. Neureuther, "Enhanced quantitative analysis of resist image contrast upon line- edge roughness (LER)," Proc. SPIE, Vol. 5039, 423-432 (2003).

[7]   A. Pawloski, A. Acheta, I. Lalovic, B. La Fontaine, and H. Levinson, "Characterization of line edge roughness in photoresist using an image fading technique," Proc. SPIE, Vol. 5376, 414-425 (2004).

[8]   G. McIntyre and A. Neureuther, "Characterizing Illumination Angular Uniformity with Phase Shifting Masks," Proc. SPIE, Vol. 5040, 162-170 (2003).

7   Conclusions

This research advanced state-of-the-art EUV photoresist imaging, an important piece in commercializing EUV technology for large-scale integrated circuit production. When this research began, the existing limit of dense feature printing was in the 100- to 70-nm range for the 10×-Schwarzschild optical design. Today, with contributions from this research, dense features can now be reliably printed in the 50- to 30- nm range. Line edge roughness (LER) for dense 50-nm lines and spaces has been demonstrated at 3.3 nm rms. Further, loose pitch features have been shown at 25 nm.

This progress was achieved by combining the spatial doubling method described in Chapter 2 and the EUV optics designed for 100-nm resolution into the F2X system. In addition, simulations and techniques were developed that lead to multi-pitch printing in single exposures. Hardware modifications allowed for a six-fold increase in wafer throughput while significantly reducing procedure and processing error.

The F2X system utilized 13.4-nm coherent light from an undulator beamline with the 10× demagnification optic. High-resolution and high-contrast test patterns were exposed into both chemically and non-chemically amplified resists. Combining the demagnification with the spatial-frequency doubling technique, a full 20x reduction of object grating pitch was obtained. For example, 0.8-μm dense lines on the object grating printed 40-nm dense lines onto resist coated wafers. Line-and-space patterns were limited to one orientation and a dense 1:1 spacing.

The F2X system, as shown in Chapter 5, provided improved LER values over Sandia National Laboratory's 10× Microstepper tool using the same resist (EUV2D; measurements were made in the same SEM using the same software). This was also for features half the size. The F2X tool printed 50-nm features whereas the 10× Microstepper printed 100-nm lines.

A number of techniques of merit were developed for more comprehensive evaluation of photoresist performance in the 50-nm range. For example, printing four different pitches in a single exposure removed wafer-based variations when comparing different linewidths. This technique enhanced the original spatial frequency doubling method by changing to a new mask set and a different spatial filter.

The most recent advancements came through the development of aerial image contrast methodology. Previously, in other non-EUV tools, a two-exposure process was used for evaluating contrast: a pattern exposure followed by a background flood exposure. In this research, contrast variation was integrated into the mask design. Through grating duty cycle changes, the relative strengths of the diffracted orders were programmed. Using spatial filtering, only the 0 and +1 orders were used to create the field mismatch. Different imbalances in the orders resulted in different image contrasts at the wafer plane. As constructed, the duty cycles on the mask did not print on the wafer since all orders except 0 and +1 were filtered out, resulting in the printing of constant linewidths.

Coherence played an important role in these experiments. Both the spatial frequency doubling and aerial image contrast methods utilize the coherent addition of

diffracted orders. Unfortunately, coherence also brings edge ringing and amplifies any deviations or defects with the mirrors and masks. These effects were studied and the results are summarized in Chapter 5.

The following table highlights a variety of the smallest features that were produced using the various 10× systems and the Micro Exposure Tool (MET), and are supported in the text and figures of this thesis.

Feature Description	Value	Resist
Smallest CA dense lines in 10×	40 nm	EUV-2D, EUV-F2X, 1K
Smallest CA dense lines in MET	30 nm	1K
Smallest non-CA dense lines in 10×	30 nm	PMMA
Smallest CA loose pitch line in 10×	25 nm	EUV-F2X
Smallest non-CA loose pitch line in 10×	29 nm	HSQ
Smallest LER for dense 50-nm lines in 10×	3.3 nm	1K
Smallest LER for dense 50-nm lines in MET	3.3 nm	1K
Smallest LWR for dense 50-nm lines in 10×	3.9 nm	1K
Smallest LWR for dense 50-nm lines in MET	5.3 nm	1K
Smallest LER for dense 30-nm lines in MET	5.6 nm	1K
Smallest LWR for dense 30-nm lines in MET	11.3 nm	1K

CA – chemically amplified resist
Line edge roughness (LER) and line width roughness (LWR) values are 3 sigma rms
CA resists: EUV-2D, EUV-F2X (XP9947W), and 1K provided by Shipley
Non-CA resists: PMMA from MicroChem, HSQ from Dow Corning

Modifications to the F2X system that contributed to the increased throughput (~6×) and enhanced results mentioned above included a new 10× optic, a load lock sub-system, and a new vacuum chamber (Chapters 3 and 4). Simulations were required to develop specifications for fabrication of this new optic and its ultimate alignment. At-wavelength

interferometry was also done to determine actual optical performance. It is worth noting that Intel has used this modified tool for resist screening.

This work contributed to advancing the commercialization of EUV technology. More, however, needs to be done. For example, more progress is needed in resist chemistry as well as resist evaluation tools and methodologies. Intel's relevant resist specifications include resolution in the 10- to 20-nm range, LWR < 1.5 nm rms (3 sigma), and sensitivity between 2 and 5 mJ/cm^2. New tools such as the MET are now in place and will continue the challenge of advancing the EUV roadmap.

8   Appendix A - 10×-Intel

8.1   Zernike Coefficients

	n	m	j	EUV 421 px 0.0876 NA nm RMS coeff		EUV 337 px 0.07 NA nm RMS coeff		Visible 151 px 0.07 NA nm RMS coeff	
				0.0876 NA	RMS	0.07 NA	RMS	0.07 NA	RMS
astig	2	2	4 5	-0.0888	0.2623 astig	-0.1938	0.2022 astig	0.0846	0.0903 astig
	2	-2		-0.2469		-0.0577		0.0315	
coma	3	1	6	0.0377	0.2012 coma	-0.0039	0.0360 coma	0.0046	0.0985 coma
	3	-1	7	0.1976		0.0358		0.0984	
sph ab	4	0	8	-0.1585	0.1585 sph ab	-0.0455	0.0455 sph ab	-0.0210	0.0210 sph ab
trifoil	3	3	9	-0.1663	0.5873 trifoil	-0.1108	0.3216 trifoil	-0.0703	0.2341 trifoil
	3	-3	10	-0.5632		-0.3019		-0.2233	
astig	4	2	11	0.1444		0.0610		0.0380	
	4	-2	12	-0.1234		-0.1691		-0.1556	
coma	5	1	13	0.0232		0.0739		0.0781	
	5	-1	14	0.0580		0.0657		0.0195	
sph ab	6	0	15	-0.0036		-0.0044		0.0181	
quad	4	4	16	0.0076		-0.0659		-0.0636	
	4	-4	17	0.1035		0.0267		0.0270	
trifoil	5	3	18	0.0293		0.0035		-0.0297	
	5	-3	19	0.0020		-0.0214		-0.0184	
astig	6	2	20	-0.0112		-0.0355		-0.0045	
	6	-2	21	0.1121		0.0665		0.0501	
coma	7	1	22	-0.0615		-0.0425		0.0106	
	7	-1	23	-0.0387		0.0003		-0.0348	
sph ab	8	0	24	0.0207		-0.0249		-0.0307	
quit	5	5	25	0.0244		-0.0028		-0.0205	
	5	-5	26	-0.0314		0.0004		0.0127	
quad	6	4	27	0.0583		0.0154		-0.0268	
	6	-4	28	0.0084		0.0274		0.0212	
trifoil	7	3	29	0.0063		-0.0026		0.0162	
	7	-3	30	0.0197		0.0351		0.0278	
astig	8	2	31	0.0153		0.0417		0.0189	
	8	-2	32	-0.0457		0.0048		0.0146	
coma	9	1	33	0.0294		-0.0087		-0.0324	
	9	-1	34	-0.0003		0.0123		0.0252	
sph ab	10	0	35	0.0257		0.0183		-0.0104	
sph ab	12	0	36	-0.0154		-0.0034		-0.0076	
			RMS37	0.7459	0.0553	0.4561	0.0338	0.3379	0.0250
			P-V	4.7312	0.3505	2.7258	0.2019	2.6470	0.1961

For the three wavefront measurements discussed in Section 3.2.3, the Zernike coefficients are given in the table above. The coefficient ordering used here is shown in the left columns: n is the radial order, and m is the azimuthal order. For the low-ordered aberrations, coeffient pairs are combined into a single RMS magnitude. Near the bottom of the table, the 37-term RMS and peak-to-valley wavefront aberration magnitudes are given, first in nm, followed by waves at 13.5 nm.

Over 0.07 NA, the EUV-visible-light difference wavefront magnitude is 0.336 nm within the first 37 Zernike terms. When astigmatism is removed from consideration, the RMS difference wavefront magnitude becomes 0.165 nm.